UNIVERSITÀ DEGLI STUDI DI PADOVA

Department of Physics and Astronomy

master's degree in astronomy

Master's Degree Thesis

Analysis of Oxia Planum region (Mars): the landing site of the ESA ExoMars 2020 rover

Supervisor:
Prof. Monica Lazzarin
Co-supervisor:
Dr. Gabriele Cremonese
Co-supervisor:
Dr. Maurizio Pajola

Candidate:
Maria Mastropietro
Matr.:1181894

Academic Year 2018-2019

Ai miei genitori, che mi hanno sempre
supportata in questi anni di studio.

Ai miei parenti, che mi sono sempre stati vicini,
anche se alcuni non più fisicamente.

Alle amiche ed amici, sempre disponibili
ad aiutarmi nei momenti in cui avevo bisogno
e che mi hanno sempre motivata.

Alle mie ex coinquiline, che mi hanno sopportata molto,
alle quali, quando ho iniziato i conteggi,
chiedevo: "secondo voi questo è un cratere?".

A chi mi chiama CIAM, per il suo
prezioso conforto e la sua vicinanza.

Abstract

The Oxia Planum region has been chosen as the landing site for the future ESA ExoMars 2020 rover for engineering and scientific aspects.
The main goal of this thesis is the identification and measurement of craters and boulders located in the Oxia Planum region to understand both the surface exposure ages as well as the processes that occurred over the studied area. We use THEMIS images to date the surface units, a middle and a late Noachian unit, present on Oxia Planum, by using the method of counting craters. We obtain a modelled age of 3.85 +0.02/-0.02 Ga for the middle Noachian unit and of 3.82 +0.02/-0.03 Ga for the late Noachian one, quantitatively confirming that the Oxia Planum region dates back to the Noachian age. We also derive the age of the four deposits that are present inside the landing ellipse, by using high resolution CTX images. We obtain a modelled age of 1.39 +0.56/-0.56 Ga for the Amazonian unit and the modelled ages of about 660-600 Ma and 1.79 +0.30/-0.30 Ga for the three exhumed Noachian units. These results are pivotal to suggest an evolutionary model of the Oxia Planum region: two of the exhumed Noachian units have similar exhumation ages, while the remaining exhumed Noachian unit was exhumed earlier than the other two given its higher relief; on the contrary, the Amazonian unit was largely eroded and it is still being degraded letting the Noachian terrains situated underneath to be exposed. The study of the areal density of the craters is important also for rover landing and traversing reasons. We find that the Noachian unit is safer with respect to the Amazonian one. For the boulders manual identification and count we use HiRISE images and we calculate their size-frequency distribution and their spatial density in different areas of the landing ellipse to determine the processes that occurred on the Oxia Planum. We find that the formation of boulders in this area is due to impact processes and we derive that the Amazonian unit is from 2.4 to 48.2 richer of boulders than the exhumed Noachian units. By comparing these results with other boulder distributions previously accomplished on different locations of Oxia Planum we derived a lower spatial density of boulders. Nevertheless, the similar SFD obtained suggests that the erosive processes that occurred in our studied area are similar. We also compare our results with the ones derived from other landing sites on Mars, finding, for example, that the Pathfinder landing site is 4.2 times more dangerous than our exhumed Noachian 2 unit. The boulder analysis is of fundamental importance from an engineering perspective, returning the safest areas where the ExoMars 2020 rover might land and traverse.

Contents

Introduction

This thesis focuses on the counting of craters and boulders in the Oxia Planum region, the landing site of the ESA ExoMars 2020 rover. This was made for scientific and engineering perspectives to show that Oxia Planum is an interesting and an important region for exobiological studies and it is also an engineering-safe area for the landing and roving phases.
In the first chapter an introduction about the general properties of Mars is presented with, in particular, its geologic history. In the second chapter the dataset and methodology used for the presented analysis are showed in detail. We explain that the craters counting is important to estimate the age of the considered zones as well as for safety reasons: if the rover were to land in a crater with too steep walls, it would remain locked inside. Regarding the boulders counting, we explain it is of pivotal importance because from their size frequency distribution it is possible to distinguish the groups of boulders that had an impact origin from those that formed due to wind erosion and possible collapse. As for the craters, the boulders counting is also important due to safety reasons, since boulders can be dangerous during the rover landing and traversing. In the third chapter the ExoMars 2020 mission and the requirements needed to select a landing site are presented together with a general overview of the Oxia Planum region. In the fourth and last chapter we present the obtained results and we thoroughly discuss them, suggesting an evolutionary model of the Oxia Planum region. Eventually, we made a comparison both between our boulder results with those of previous works, as well as with other Mars landing sites.

Chapter 1

Mars

1.1 Physical characteristics

Mars is the fourth planet of our Solar System, orbiting around the Sun at a distance of about 1.5 AU (Table 1.1). Its mass is $\frac{1}{10}$ of Earth's mass, its radius is $\frac{1}{2}$ of Earth's radius and its gravity is $\frac{1}{4}$ of Earth's gravity. Mars' orbit is among the most elliptical of the planetary orbits, its eccetricity is indeed about 0.09. A day on Mars is similar to a terrestrial day and its year is about 2 terrestrial years. Its axial tilt is 25.2°, particularly similar to the Earth's one, this is why Mars has season (Barlow, 2008). The temperature on the planet changes a lot, on average it is about -63 °C (210 K) with a diurnal range between -89 and -30 °C (184 K and 243 K). For a comparison, on Earth the average temperature is 15 °C (288 K) (Kading and Straub, 2015). Mars has two small and irregular moons, Phobos and Deimos.

	Mars	Earth
Distance from Sun	2.279 x 10^8 km (1.524 AU)	1.496 x 10^8 km (1 AU)
Mass	6.417 x 10^{23} kg	5.972 x 10^{24} kg
Radius	3390 km	6371 km
Density	3.934 g/cm^3	5.513 g/cm^3
Surface gravity	3.71 m/s^2	9.807 m/s^2
Eccetricity	0.0934	0.0167
Rotation period	24.623 hours	23.934 hours
Revolution period	686.98 Earth days	365.26 days
Axial tilt	25.2°	23.439°
Surface temperature	120–293 K	185–331 K

Table 1.1: Informations on Mars and Earth

1.2 Magnetic field

Mars is a terrestrial planet that is less dense than Earth (Table 1.1), with a differentiated internal structure. The dense metallic core region is mainly constituted by iron and nickel with about 16-17% sulfur (Rivoldini et al., 2011). The core is surrounded by a silicate mantle, which originated the volcanic and tectonic features on the planet in its past. The crust is made by silicon, oxygen and other abundant elements like iron, magnesium, aluminium, calcium and potassium (Rivoldini et al., 2011). Mars is also called the "Red Planet" because of the iron oxide present on its surface, that gives a reddish colour to the planet.
By means of measurements made by the US Mars Global Surveyor, fossil magnetization in the Martian rocks has been seen in the southern hemisphere, an index of the presence of a strong magnetic field on the planet in the past (over 4 Ga), able to protect Mars from the solar radiation and to maintain climatic conditions advantageous for liquid water to exist (Michalski et al., 2017). This magnetic field was produced by a dynamo effect and then by convection movements of metals in the core, that was partially or fully liquid. Nowadays Mars has no longer a global magnetic field. The reason for this change may be due to the fact that Mars cooled early in its history. Probably the planet cooled down and the dynamo effect decreased, the convective motion stopped, because the liquid core completely solidified. However, recent data about Mars suggest that this is not the case, and the liquid core may still be present (Sakai et al., 2018).

1.3 Atmosphere

With a surface pressure of 6 mbar, Mars has a thin atmosphere, primarily composed of carbon dioxide, small quantities of molecular nitrogen and few traces of water vapor. It is too thin now so there is no liquid water on the Martian surface, but in the past the atmosphere was thicker, as showed by the presence of few little impact craters. With a denser atmosphere on Mars, the temperature was good enough to have liquid water on the surface (Heather et al., 2017). The solar radiation Mars receives is half the radiation received by Earth, hence it has a lower effective temperature and a weak greenhouse effect due to the low abundance of greenhouse gases. However, in the past, active volcanoes were filling the atmosphere of gases. Later on, their activity started to diminish, the greenhouse effect decreased, so water vapor and carbon dioxide were incorporated in the ground, disappearing from the atmosphere. Hence, the atmosphere became thinner, molecules were divided

by the solar UV radiation and escaped in the space. Another cause of gas escaping is probably the disappearing of the magnetic field, that was not able to protect the atmosphere from the solar wind particles anymore (Jakosky et al., 2015).
For all the above reasons the atmosphere was lost, the liquid water present on the surface started to evaporate together with a decreasing pressure. It is therefore possible that the water was incorporated by the polar ice caps or by the underground (Galletta and Sergi, 2005).

1.4 Geologic history

The geologic history of Mars is divided into three main periods (Figure 1.1): Noachian (>3.7 Ga), Hesperian (∼3.7-3.0 Ga) and Amazonian (<3.0 Ga) period (Figure 1.1) (Michael, 2013). There is also a Pre-Noachian period characterized by the formation of Mars (Carr and Head, 2010).

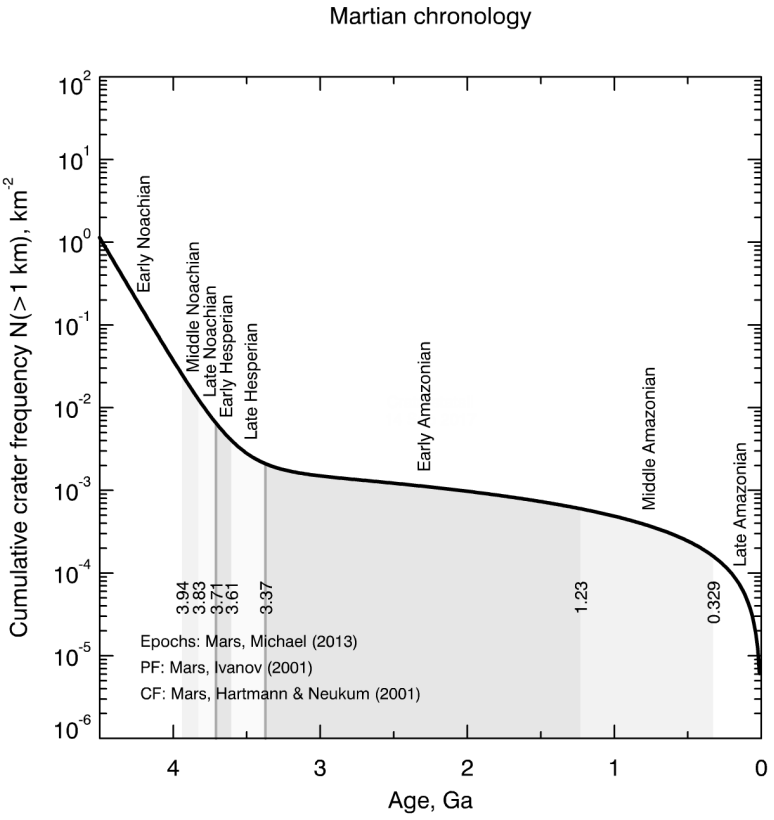

Figure 1.1: Chronology of Mars epochs (Michael, 2013).

1.4.1 Noachian period

During the Noachian period, the end of the late heavy bombardment occurred. This period was characterized by high rates of craters impact, erosion, valley formation and the volcanism was concentrated around the Tharsis region. The heat generated by the impacts and the outgassing from volcanoes created a warmer climate. There was the formation of acqueous minerals like phyllosilicates and water and other greenhouse gases were expelled into the atmosphere (Carr and Head, 2010; Segura et al., 2002).

1.4.2 Hesperian period

The Hesperian period is characterized by less crater impacts and erosion when compared to the Noachian time, but strong volcanic activity, indeed resurfacing phenomena can be seen and also the formation of outflow channels, created by lava and water released from the underground. When the volcanic activity declined, the SO_2 was removed from the atmosphere, such that a high formation of sulfates occurred. The weather changed becoming colder (Carr and Head, 2010).

1.4.3 Amazonian period

The Amazonian era is characterized by low rates of meteorite and asteroid impacts and by cold and dry climatic conditions similar to the current ones. This period is marked by the oxidation process that makes the Martian surface of its reddish colour. Nowadays water is not liquid on the surface, but it is present in considerable quantities in the form of ice (permafrost) in the underground and above all in correspondence of the two polar caps of the planet. The presence of ice in this period is abundant (Carr and Head, 2010; Smith et al., 2016). Gullies, similar to the terrestrial ones, were probably obtained by the melting of this ice, to indicate liquid water action (Malin et al., 2006). Volcanic activity decreased while aeolian phenomena were numerous and this is evident by the large amount of dunes distributed globally on the Martian surface (Carr and Head, 2010).

1.5 Geological features

Mars is characterized by multiple features testifying that in the past there was liquid water on its surface. Such examples are outflow channels, made by water, glaciers or lava (Carr and Head, 2010). Along crater and canyon walls, there are features similar to terrestrial gullies. Other geological features

are deltas, valleys, sedimental deposits and alluvial fans, where also aeolian erosion can be seen (Lewis and Aharonson, 2006).
In the Tharsis region (Figure 1.2) of Mars there are the highest volcanoes in the Solar System, the highest one is the Olympus Mons volcano with a height of about 26000 m (Galletta and Sergi, 2005). For a comparison, on Earth the highest volcano is Nevado Ojos del Salado in the Andes on the Argentina–Chile border with its 6893 m (Mpodozis et al., 1996).
Mars has also strong dust storms with maximum measured speed of 30-40 m/s. They are due to the heating of the dry ground by the Sun, as consequence a whirlwind on vertical column is formed (Ryan and Lucich, 1983 ; Ringrose et al., 2003; Ellehoj et al., 2010). For a comparison, on Earth terrestial dust devils speeds are of 5–10 m/s, but also peak winds of up to 25 m/s are not unusual (Ryan and Carroll, 1970; Balme et al.,2003).

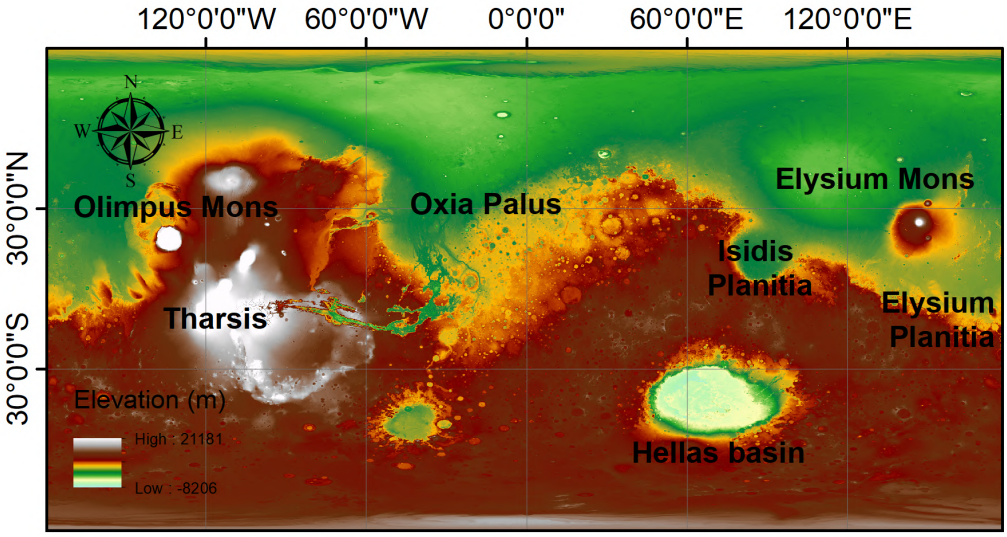

Figure 1.2: Tharsis region, Oxia Palus, Hellas basin, Isidis Planitia and Elysium Planitia on Mars. The elevation values refer to the Mars Global Surveyor-Mars Orbiter Laser Altimeter (MOLA).

1.6 Mineralogy

There several different minerals that are found on Mars, especially phyllosilicates and sulfates.
Evaporitic sulfate minerals, like gypsum and jarosite, were found on Mars and there was also the detection of Ca-sulfate bassanite on outflow channels

floor, present under phyllosilicate units (Aubrey et al., 2006; Wray et al., 2010). Sulfate minerals indicate precipitation of salts from acidic surface and near surface waters in the Hesperian period (Ehlmann et al., 2009).
The OMEGA instrument (Observatoire pour la Mineralogie, L'Eau, les Glaces et l'Activitié) found phyllosilicates, that are hydrous minerals, on Mars (Bibring et al., 2006). They are present on a large region on the planet, especially in old terrains and in the form of Fe/Mg and Al clays. Their formation started during the Noachian period and continued because of the presence of water (see subsection 1.4.1). The Compact Reconnaissance Imaging Spectrometer for Mars (CRISM) (Murchie et al., 2007) showed a large diversity of phyllosilicate mineralogy too: kaolinites, chlorites, illites or muscovites, hydrated silicates, Fe/Mg-OH phyllosilicates and smectites like nontronites and saponites. Some areas have olivine-rich materials above phyllosilicate units, to indicate cessation of aqueous alteration.
Studies made on these terrains are fundamental from an astrobiological point of view, since clay deposits are possible sites able to preserve organic material, then it is highly probable that the Noachian period was inhabited (Mustard et al., 2008; Ehlmann et al., 2008).

Chapter 2

Dataset and methodology

In this thesis the ArcGIS software was extensively used, which is a software to work and analyse both maps, multi-instrument and multi-resolution datasets, together with the associated geographic information (GIS).
The analysis of the Oxia Planum region, target of this thesis, was made by both importing in the ArcGIS software elevation maps (MOLA, see section 2.1), multi-resolution images (THEMIS, CTX and HiRISE, see section 2.2) and geological maps already prepared for Mars (see section 2.3).

2.1 Digital Terrain Model

Elevation values of Mars are given by the Mars Orbiter Laser Altimeter (MOLA) (with a spatial scale of 463 m/pixel at lower latitudes to 115 m/pixel near the poles) (Zuber et al., 1992; Smith et al., 2001) (Figure 2.1). MOLA is an instrument aboard Mars Global Surveyor that has measured the topography of the Martian surface giving a global map of the planet. MOLA operated by transmitting an infrared laser towards Mars. The distance was determined by measuring the time of a laser pulse from the instrument to the planet surface and back to the instrument. In this way a digital terrain model (DTM) of the planet was obtained, in the latitudes from –87° to +87°. The main goals of MOLA are to provide and refine the global map of Mars surface in terms of pixel scale and vertical accurancy, to produce high resolution regional topographic grids, to improve measurements of optical pulse width and reflectivity (Zuber et al., 1992). Moreover, MOLA is fundamental to resolve time variations in the elevation due to seasonal change of CO_2 and to monitor exchanges in the atmosphere due to CO_2 and dust transport. Using MOLA it is possible to find future landing site thanks to the high resolution local grids of topography, slope and surface roughness (Smith et

al., 2001).
In the map shown in Figure 1.2 a high contrast in elevation between the Martian northern and southern hemispheres can be seen. The highest elevations are found in the Tharsis region, the lowest ones are in the Hellas basin (Smith et al., 2001).

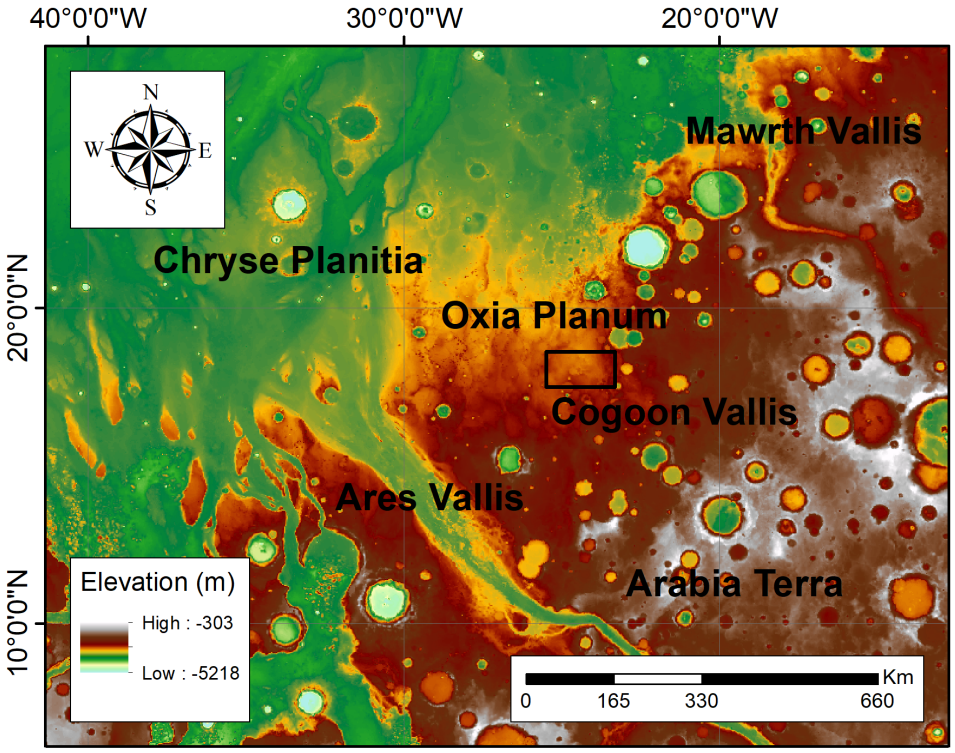

Figure 2.1: MOLA context map showing the location of the Oxia Planum region. In the black rectangle the location of the landing ellipse for the ExoMars 2020 mission is showed (see Figure 3.2 in detail).

2.2 Imaging

2.2.1 Thermal Emission Imaging System (THEMIS)

The Thermal Emission Imaging System (THEMIS) is the scientific camera onboard the 2001 Mars Odyssey orbiter (Christensen et al., 2004). Its spatial scale is 100 m/pixel (Figure 2.2), and it provides images of the entire surface of Mars through multi-spectral thermal-infrared images in nine

wavelengths, centered from 6.8 to 14.9 μm, and through visible/near-infrared images in five bands, centered from 0.42 to 0.86 μm. THEMIS mapped the entire planet during day and night to determine the thermal properties of the surface and to investigate the surface mineralogy and physical properties of the planet. Indeed, geologic materials like carbonates, silicates, sulfates, phosphates and hydroxides, have strong fundamental vibrational absorption bands in the thermal-infrared spectral region, hence providing diagnostic information on mineral composition.
The main goals of the THEMIS camera is to study the mineralogy of the deposits related to hydrothermal or sub-aqueous environments, to identify landing sites, to search for thermal anomalies related to active sub-surface hydrothermal systems, to study the characteristics of geologic processes and landing sites using morphologic and thermophysical properties and to investigate polar cap activities during all seasons (Christensen et al., 2004).

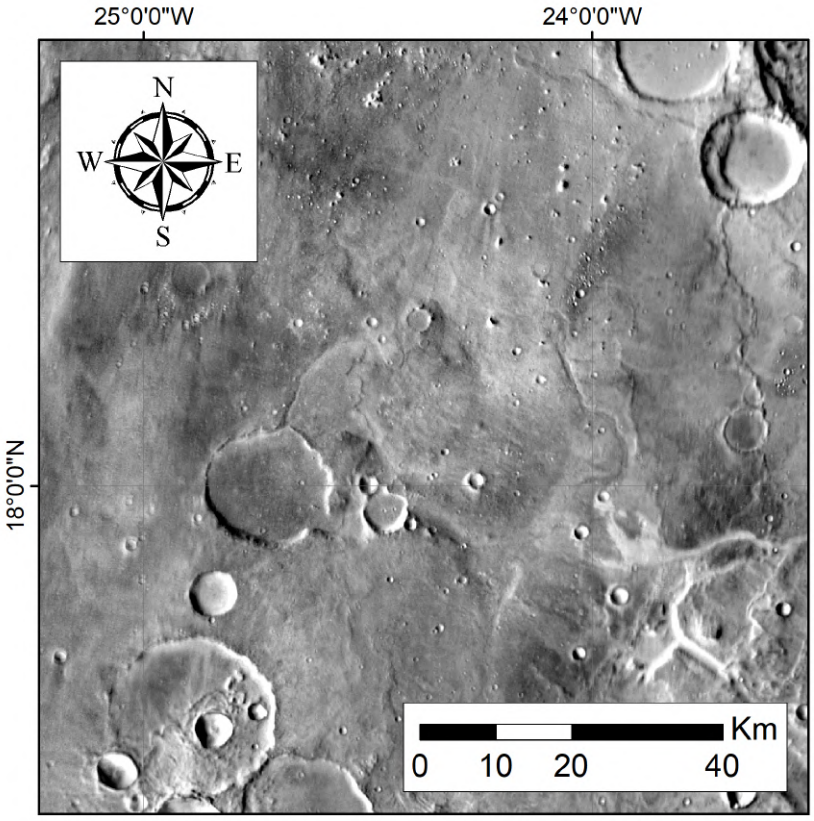

Figure 2.2: The Oxia Planum region showed on the THEMIS map.

2.2.2 The Context Camera (CTX)

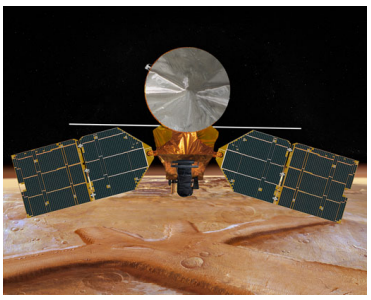

Figure 2.3: Mars Reconnaissance Orbiter (MRO), from nasa.gov.

The Context Camera (CTX) returns images of the surface of Mars with a pixel scale of 6.0 m/pixel (Malin et al., 2007) (Figure 2.4). This camera was built to provide context for images acquired by other instruments on board the Mars Reconnaissance Orbiter (MRO) (Figure 2.3), in particular the High Resolution Imaging Science Experiment (HiRISE) and the Compact Reconnaissance Imaging Spectrometer for Mars (CRISM) (Bell III et al., 2013).
The main goals of CTX are to observe candidate landing sites and to conduct a scientific investigation of geologic, geomorphological and meteorological processes on Mars. Since the MRO spacecraft can be rolled off nadir, CTX is able to acquire stereoscopic image pairs of specific targets on Mars, hence Digital Terrain Models (DTM) of the surface can be created. CTX takes images spanning 30 km of terrain (Malin et al., 2007).

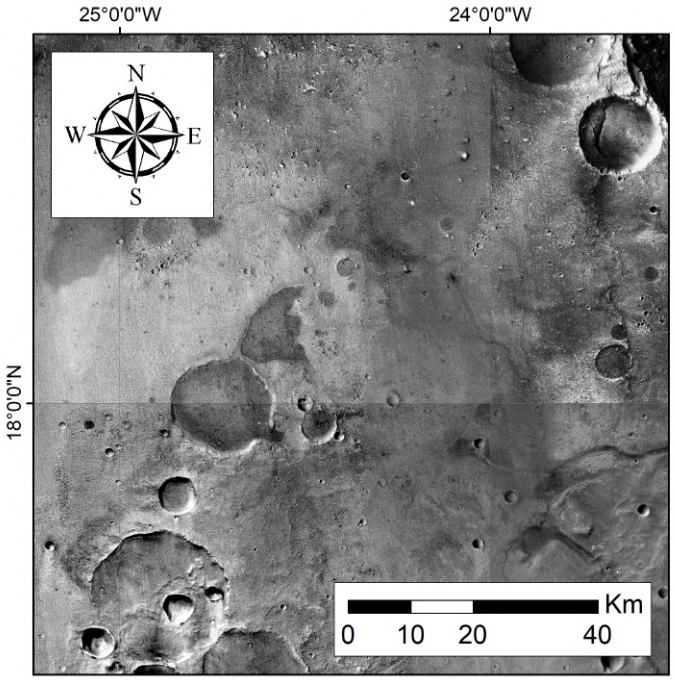

Figure 2.4: The Oxia Planum region showed on four CTX.

2.2.3 High Resolution Imaging Science Experiment (HiRISE)

HiRISE is the high-resolution scientific camera onboard the MRO spacecraft (Figure 2.3). This instrumet provides images of the surface of Mars with a spatial scale of 0.3 m/pixel (McEwen et al., 2007) (Figure 2.5). HiRISE images are taken both in the visible and NIR wavelenghts. The high resolution of this camera is essential because surface features of Mars are possible to be seen in great detail and it provides a good characterization of the Martian environment, especially in the searching for landing sites (Delamere et al., 2003). Acquiring stereo pairs is fundamental for topographic measurements, essential in the characterization of landing sites and to study surface processes (McEwen et al., 2007).
The main goals of the HiRISE camera are to search for sites showing evidence of aqueous and hydrothermal activity, to characterise in detail the stratigraphy, geomorphology and composition of Mars surface and subsurface and to understand better the nature and evolution of different Martian terrain types. Moreover, HiRISE is fundamental to identify sites for future landed exploration that have a high potential for future scientific discoveries and that are sufficiently safe for future landers/rovers (Zurek and Smrekar, 2007).

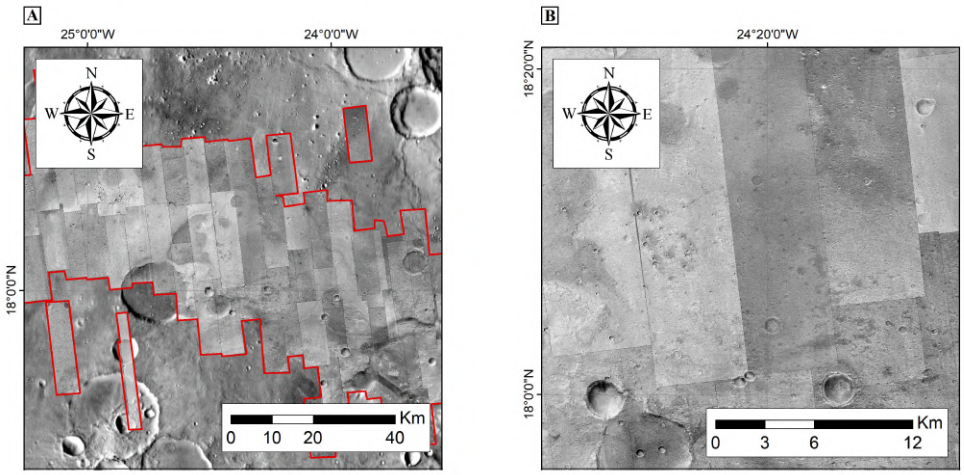

Figure 2.5: In the panel A the Oxia Planum region is showed on HiRISE images (highlighted with the red polygons) with THEMIS map in background. In the panel B a zoom of the centre of the Oxia Planum region is showed on HiRISE images.

2.3 The Mars global geological map

The Tanaka et al. (2014) global geological map (Figure 2.6) shows the distribution of geologic units and landforms on Mars' surface, divided in a chronological way. It is based on data supplied by NASA's Mars Global Surveyor (MGS), Mars Odyssey (ODY), Mars Reconnaissance Orbiter spacecraft and by the European Space Agency's Mars Express orbiter. These data have provided a digital geologic database of Mars, useful for investigations of its geology.

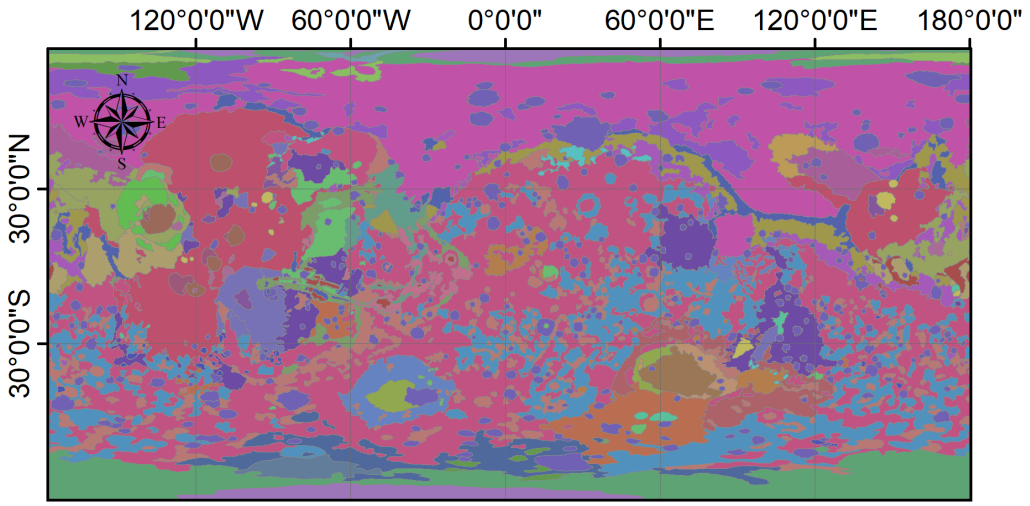

Figure 2.6: The global geological map by Tanaka et al. (2014) where different colored areas correspond to different geological units and surface exposure ages.

This map establishes the first global chronologic units division of Mars' terrains. Using the crater counting technique these units were divided in progressively lower crater density and thus younger relative age units: the Noachian, the Hesperian and the Amazonian periods.
In the Noachian highland unit three morphologic categories were identified: Early Noachian (with highest density of impact craters); Middle Noachian (with intermediate density of impact craters) and Late Noachian (with relatively low density of impact craters).
The Hesperian epoch is divided into Early Hesperian period, defined by volcanic unit, and Late Hesperian lowland unit.
The Amazonian Epoch is divided into Early Amazonian unit, Middle Amazonian lowland unit and Late Amazonian unit that is the polar unit, which forms ice-rich layered plateaus at both poles (Tanaka et al., 2014).

2.4 Planetary chronology

The surfaces of planets and small bodies are covered by a great number of impact craters with a wide range of different appearences, from old, heavily battered ones, to newer, fresh craters with sharp rims and bright rays (Melosh, 1989). The analysis of the crater rate formation is pivotal to understand the geologic history as well as the evolution of the considered surfaces. The value of ages determined from crater counts is called crater retention age. This parameter dates the length of time that a topographic feature can be retained in the case of erosion (Hartmann, 1966; Hartmann, 1977; Hartmann and Neukum, 2001). The determination of a terrain's age is based on the cratering record, it requires a crater population that is not in equilibrium and where superposed craters are counted. In addition, all secondary and volcanic craters are removed from the counts (Strom and Sprague, 2003). On the contrary, a crater population reaches equilibrium when crater density becomes constant and only a lower limit on the age can be obtained (Melosh, 1989). At the equilibrium point, the craters size frequency distribution (SFD) no longer changes because impacts are obliterated by various processes such as crater overlap, ejecta emplacement, lava flows and eolian erosion (Hartmann, 1984; Woronow, 1977; Woronow, 1978).
A statistical analysis of the craters located in different units is able to give the relative surface age (Hartmann, 1977; Melosh, 1989; Neukum et al., 1975a; Neukum and Ivanov, 1994). This is possible because the frequency of impact craters is related to geologic time: the higher is the frequency, the older is the age, meaning that the surface was exposed for long time (Hartmann et al., 1981; Neukum et al., 1975a; Wagner et al., 2010). Together with the relative surface age, absolute ages can be obtained too if the time dipendent impactor flux on the target body is known. Nevertheless, current models are still far from being accurate for the early stages of Solar System formation.

2.4.1 Neukum Production Function (NPF)

Using the crater statistics, a method to obtain the absolute age was developed for the Moon (Neukum, 1983; Neukum and Ivanov, 1994; Neukum et al., 1975a; Neukum et al., 2001a). The model presented in Neukum (1983) is an empirical chronology that is based on the correlation between the radiometric ages of the rock samples analysed from the Apollo landing sites and the crater frequencies derived from the investigation of the images of the Moon surface (Neukum, 1983; Neukum and Ivanov, 1994; Neukum et al., 1975a; Neukum et al., 2001a).
In this model the determination of the SFD of an impact crater population

on the Moon over large sizes of craters is the Neukum Production Function (NPF) (Neukum and Ivanov, 1994; Neukum et al., 1975a; Neukum et al., 1975b). The first step to obtain such SFD is to select regions of different ages that have a homogeneous geologic history (Neukum and König, 1976; Neukum and Ivanov, 1994; Neukum et al., 1975a). Afterwords, a counting of craters is needed, where the detected craters have to be primary, while secondary craters and volcanic features must to be avoided. Secondary craters (see subsection 2.4.3) can be identified thanks to their elongated shapes or by being in clusters (Neukum and König, 1976; Oberbeck and Morrison, 1973), but in some rare cases their recognition may not be complete. In addition, secondary craters do not contribute uniformly to the primary crater population as they only occur in a limited size range. Due to the presence of secondaries craters a $\pm 30\%$ uncertainty in crater frequency can be assumed (Neukum, 1977b).
The fit that is obtained from the NPF is in accordance with the distribution of the considered crater population (Neukum, 1977a). Deviations from the NPF are due to endogenic processes, like lava flows, or exogenic processes, like superposition by other impact craters, erosion and ejecta blanketing emplacement (Hartmann et al., 2008; Ivanov et al., 2002; Neukum et al., 1975a). Due to processes of deposition and erosion, small craters are lost more than large ones hence resulting in an increasing of the slope of the curve in the cumulative plot (Neukum and Ivanov, 1994).
The empirical relation of Neukum chronological model for the Moon is showed in the following equation:
$N(1)=5.44 \times 10^{-14} (e^{6.93T} - 1) + 8.38 \times 10^{-4} T$
This equation relates the cumulative number crater frequency per km^2 at diameter of 1 km with the crater retention age (T) in Ga (Neukum et al., 2001b). The cumulative SFD represents the number of craters greater than or equal to a given diameter per unit area, as a function of the diameter. This distribution is independent of bin size. The resulting log-log plot displays the obtained distribution along with the confidence interval $\pm\sigma$.
Using this equation it is possible to infer absolute ages for any region with an available crater frequency (Neukum, 1983; Neukum and Ivanov, 1994; Neukum et al., 2001a). Possible uncertainties can derive from (Hiesinger et al., 2000; Wagner et al., 2002; Wagner et al., 2010):

- the crater SFD measurement procedure, due to the influence of factors such as flooding, blanketing, secondary cratering, superposition, infilling, abrasion, mass wasting and volcanic craters (Neukum et al., 1975a);

- the quality, the spatial resolution and the illumination conditions of the

images where the craters are counted, because they can have influence on the detection;

- radiometric dating of rock samples;
- derivation of the cratering chronology model.

Later on, the crater chronological model developed for the Moon, was also used for age determination of other terrestrial planets. To transfer the lunar impact crater SFD to other planets, differences have to be considered like different projectile flux, impact velocity distribution, gravity, atmosphere, crustal strength density and structure (Hartmann, 1977; Neukum and Ivanov, 1994; Ivanov, 2008; Ivanov et al., 2001; Ivanov et al., 2002). The procedure follows some steps (Hartmann, 1977; Neukum and Ivanov, 1994; Ivanov et al., 2001, 2002; Neukum et al., 2001a; Neukum et al., 2001b), that are based on the use of scaling laws, assuming new impact velocity values and considering all the parameters involved in the process of crater formation.

2.4.2 Hartmann Production Function (HPF)

Another function to produce SFD was developed by Hartmann (Hartmann, 1995; Ivanov et al., 2002; Neukum et al., 2001a). Analysing the diameters of the craters in the lunar catalog, in Hartmann (1964, 1965) the log–incremental SFD with a $\sqrt{2}$ bin size was used. The Hartmann Production Function (HPF) (Hartmann et al., 1981) shows different branches: a steep secondary one (diameter $<$ 1.41 km), a primary one (1.41 km $<$ diameter $<$ 64 km) and a turndown one (diameter $>$ 64 km).
Later on, using high resolution images of the Moon, given by the Ranger program (1960s), it was found that the primary and secondary branches are due to the ones produced during rock fragmentation at respectively lower and higher energies. The primary power-law fit was similar to the size distribution distinguished in asteroids, where collision and fragmentation are abundant (Hartmann, 1964; Hartmann, 1969). The secondary power-law fit was explained as a combination of primary impactors and secondary craters due to fallback of the ejecta (Shoemaker, 1965). In Neukum and Ivanov (1994) the NPF was also observed in space, such as on asteroid 951 Gaspra, therefore it was concluded that part of the secondary branch was due to debris from space. Thanks to this discovery the two production functions were compared and an agreement between the two ones was found (Hartmann, 1999).
Once the shape of the lunar SFD has been obtained, crater-based ages can

be estimated using isochrons, where an isochron is defined as the total number of craters formed on an age-specific surface layer, as a function of their sizes. Such isochrons represent the observed crater diameter distribution on a surface if no successive process has modified it (Hartmann, 1999). It was adopted to derive the crater retention age on Mars (Hartmann, 2005). Some assumptions were made to adapt the Lunar model to Mars, such as the hypothesis that the SFD and time dependence of the impact flux is the same for the two bodies. In addition, some corrections were made to account for the different crater and atmosphere properties.
Hartmann et al. (2007) focused on a possible variability in the projectile rate. The lunar chronology shows an intense decrease of the cratering rate before 3.5 Ga, that corresponds to the late heavy bombardment, when a large number of comets and asteroids hit the inner Solar System, and it shows a constant cratering rate over the last 3 Ga. The impact history can be well done just in the time range from 4.0 Ga to 3.2 Ga, where lunar samples are available (Neukum et al., 2001a). This suggestion was also supported by geological considerations on landslide activity and resurfacing processes on the Martian surface (Quantin et al. 2007).

2.4.3 Secondary craters

To derive the crater chronology, problems are due to the occurrence of secondary craters. In the production function used, the crater population is considered to be made by randomly formed craters, but some craters, the secondary ones, are not produced by impacts. They are due to the fallback of ejecta from primary craters and this is the reason why they appear strongly clustered both in space and time (Melosh, 1989; Wilhelms, 1987). The gravitational acceleration is enough to make the ejecta blocks land at a high velocity resulting into the formation of craters. There are bodies with thick atmospheres that decelerate the ejecta (like Venus, Earth and Titan), objects with insufficient surface gravity to preserve the ejecta (like asteroids) or objects with high resurfacing rates that destroy small craters (like Io). Therefore, secondary craters are plentiful on objects like the Moon, Mercury and Mars (McEwen and Bierhaus, 2006).
The predominance or not of secondaries over primary craters has always been discussed since the early studies of crater distributions (Strom and Sprague, 2003). With the greater spatial resolution of the images acquired by recent missions this subject has been increasingly debated. Secondary craters can be distinguished from primaries for their elliptical shape and shallow profile (Neukum and König, 1976; Oberbeck and Morrison, 1973). In addition, secondaries usually occur in peculiar deposits pointing radially away from

the originating crater, clusters, and chains (herringbone pattern) (Oberbeck and Morrison, 1974). However, the distal secondary field produced by high-velocity ejecta can generate isolated secondaries, with a more regular shape and a dimension up to 5% of their parent crater size. In this case, secondary craters resemble smaller primaries, making it harder to reach a definitive distinction between the two populations (Neukum, 1977b).

2.4.4 The Craterstats 2 software

The analysis of crater population statistics is pivotal to establish planetary chronologies, to determine the nature of planetary surface processes and to infer the characteristics of asteroids and comets. Thanks to studies of crater size frequency, density and morphology distribution, chronologies were derived for the Moon, Mars and Mercury. Therefore, geological map and age of the surfaces were obtained and also an identification of the different geologic processes happening on the surface, like aeolian erosion, volcanism and tectonic distruption, were distinguished, since they affect the crater SFD (Crater analysis techniques working group, 1979).
A software that is used to derive the age of a planetary surface is Craterstats. This is a program for plotting crater counts and determining surface ages. The software (Michael and Neukum, 2010) plots isochrons in:

- cumulative plot, that shows the density distribution per km^2;
- differential plot, that is important to detect resurfacing events;
- relative plot (R-plot), that is used to compare size frequency characteristics of crater or impactor populations;
- Hartmann plot, that plots the HPF;

After choosing the chronology it prepares isochron that can be fitted with both cumulative and differential data.
For this thesis we counted all craters through the software ArcGis and then the crater SFD have been analyzed with Craterstats 2 (Michael and Neukum, 2010; Michael et al., 2012; Neukum, 1983). The crater ages we used is based on the crater size-frequency distribution and the chronology model of Hartmann and Neukum (2001) and the production function of Ivanov (2001) was used. In the analysis the epochs boundaries of the Martian geologic history used are from Michael (2013) and the isochrons used in the cumulative fit are from Hartmann and Neukum (2001).
We fitted a cumulative production function to a the crater size frequency distribution we obtained from the counting. This technique is used in deriving

ages for surfaces which have undergone partial resurfacing events, such as erosional or depositional events, that have affected a limited diameter range of the crater population (Michael and Neukum, 2010).

2.5 Crater counting

In order to estimate the modelled age of different regions, we manually counted the craters localised in the Oxia Planum region, based on THEMIS and CTX images to analyse the region both in a global and local fashion. We define a crater as a bowl shape impact structure with a surrounding rim. Given its hollow nature, its shadow is always located inside of the structure. A crater is a circular feature, so we fit it with a circle and extract then the diameter. The location of each craters, its diameter and area are recorded on the ArcGIS software. In Figure 2.7 and Figure 2.8 the methodology to identify craters is presented.

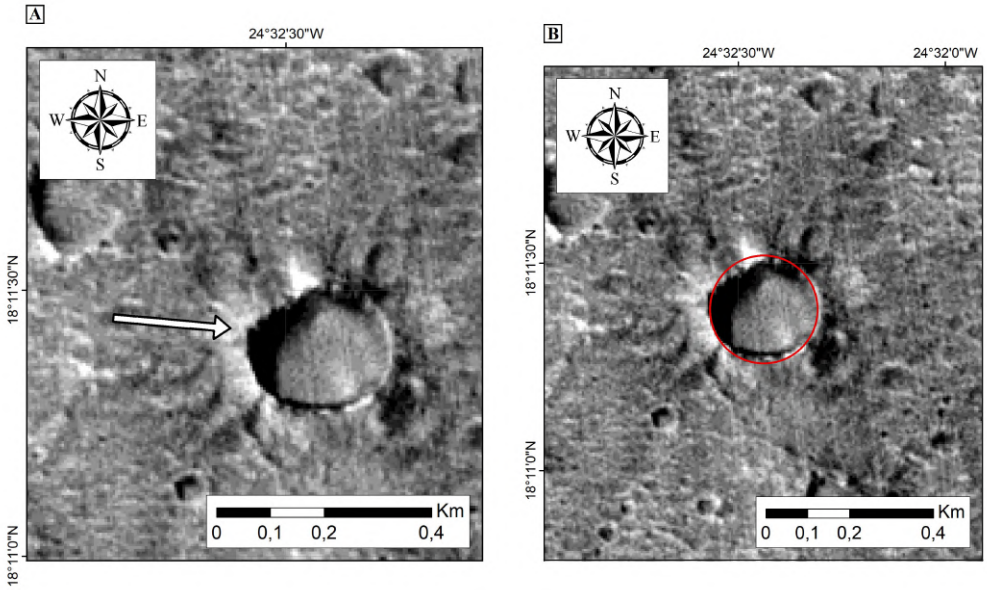

Figure 2.7: Methodology used to identidy craters. In the panel A an example of a crater located in the Oxia Planum study area is showed. The white arrow indicates the direction of the sunlight. In the panel B the red circle that fits the identified crater is presented. This is a CTX image.

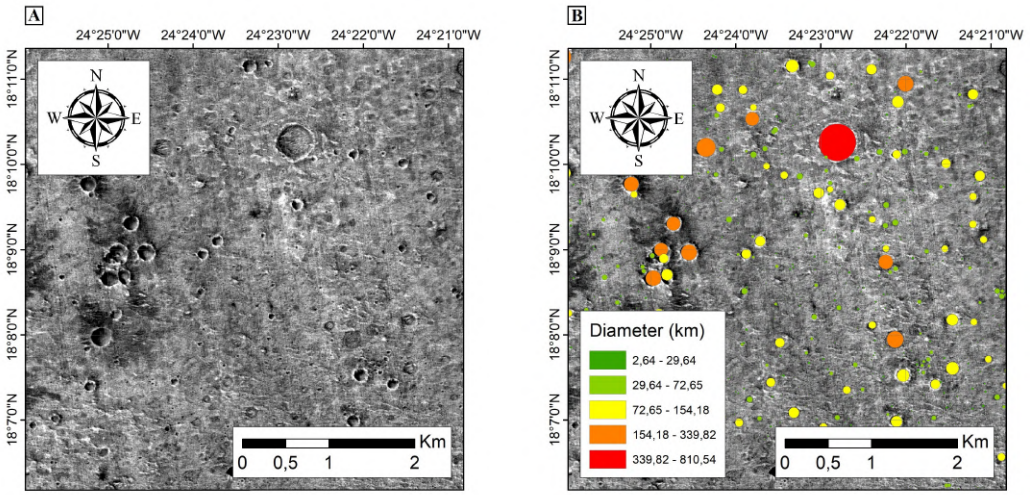

Figure 2.8: In the panel A the centre of the landing ellipse is showed. In the panel B the craters identified and the dimension range considered can be seen. This is a CTX image.

Errors and uncertainties in the detection of craters from the shape of their shadow are due to the solar incident angle and to how deep the craters is. Other errors are due to the unsure ability to distinguish non-craters from craters, since the counting was manually made. Other uncertainties relate to the resolution of the images (Golombek et al., 2008).

We studied a middle Noachian highland unit and a late Noachian highland unit, as specified from the global geologic map by Tanaka et al. (2014), using the THEMIS map in backgroung with a spatial scale of 100 m/pixel. Afterwards, we counted craters in the landing ellipse, using CTX images with a spatial scale of 5.0 m/pixel. The landing ellipse was later divided into an Amazonian volcanic unit and into three different exhumed Noachian units. To avoid calculation errors in the dating, the areas have been selected to avoid large aeolian deposits and major crater ejecta (Pajola et al., 2016b).

Later on, the software "Craterstats 2" (Michael and Neukum, 2010; Michael et al., 2012; Neukum, 1983) was used to carry out statistical analyses of the craters and in the estimate of the ages on the study areas.

2.6 Boulder counting

In order to evaluate the average boulder abundance and their associated size-frequency distribution (SFD), we manually counted the boulders located in the Oxia Planum region, based on HiRISE images with a spatial scale of 0.25 m/pixel and 0.5 m/pixel.
We define a boulder as a positive relief detectable thanks to its elongated shadow and it seems to be detached from the ground where it stands (Pajola et al., 2015, 2016b, 2017). Given its protruding nature, its shadow is always located outside of the structure. In the counting, boulders are approximated as circles using as reference their own shadow. They can have elongated shapes, but we considered their maximum size, as done in other works (Golombek et al., 2003; Michikami et al., 2008; Kueppers et al., 2012). Scarp ledges can be avoided because they have elongated shapes that are contiguous and different to those of the isolated boulders. Since a boulder is a circular feature, we fit it with a circle and extract then the diameter. The location of each boulders, its diameter and area are recorded on the ArcGIS software. In Figure 2.9 and Figure 2.10 the methodology to identify boulders is presented.

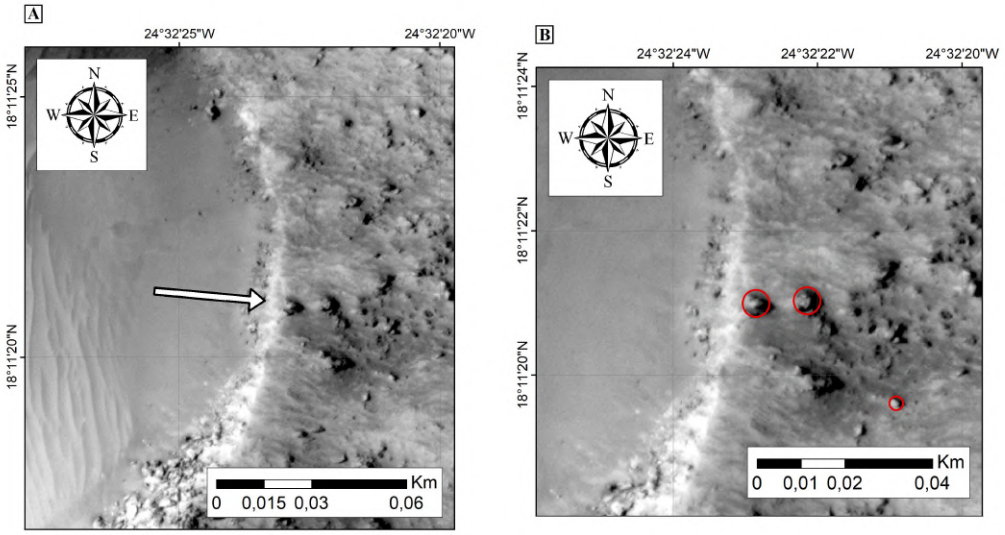

Figure 2.9: Methodology used to identidy boulders. In the panel A an example of boulders located in the Oxia Planum study area is showed. The white arrow indicates the direction of the sunlight. In the panel B the red circles that fit the identified boulders are presented. This is a HiRISE image.

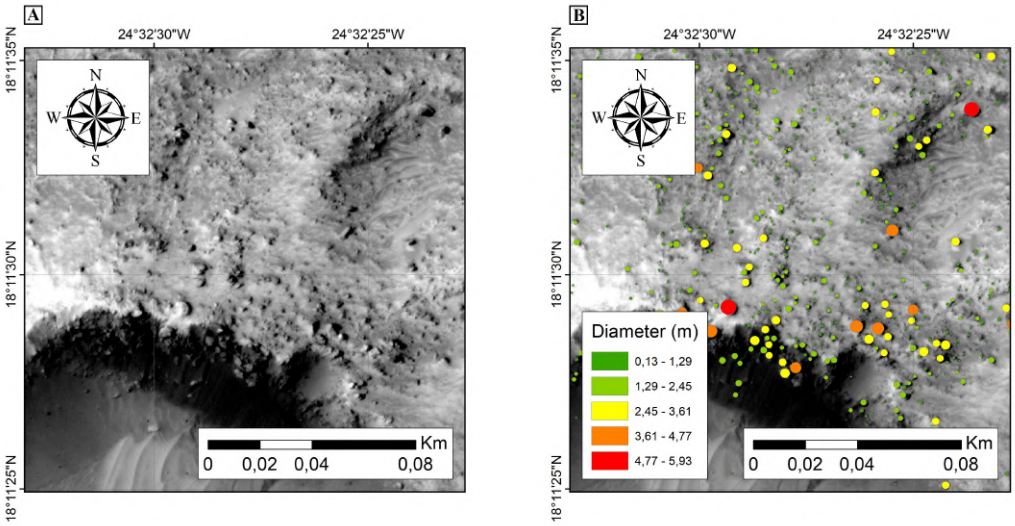

Figure 2.10: In the panel A a part of the amazonian volcanic unit in the landing ellipse is showed. In the panel B the boulders identified and the dimension range considered can be seen. This is a HiRISE image.

Errors and uncertainties in the detection of boulders from the shape of their shadow are due to the solar incident angle and to the height of the boulders. For example, the greater is the Sun angle, the smaller is the shadow formed. Other errors are due to the unsure ability to distinguish non-boulders features, like small hills, mounds and portion of escarpments, from boulders ones, since the counting was manually made. Other uncertainties relate to the resolution of the images (Golombek et al., 2008).

We studied four circular areas of radius R=500 m in the landing site and one circular area of radius R=1 km in the centre of the landing site. These regions were selected because they include two geological units, Amazonian and exhumed Noachian ones (Pajola et al., 2017).

Chapter 3

The ExoMars 2020 mission and the Oxia Planum landing site

3.1 ExoMars 2020 mission and the seach for past Martian life

The joint ESA-ROSCOSMOS ExoMars mission is planned to explore Mars, and it is divided into two parts.
The first one was launched in March 2016, it consists of the ExoMars Trace Gas Orbiter (TGO or ExoMars Orbiter) and it started orbiting the planet in October 2016. The spacecraft was carrying a technological demonstrator called EDM (Entry, Descent and landing demonstration Module) the lander Schiaparelli, that unfortunately crashed on the surface due to malfunction of the surface payload DREAMS package (Bettanini et al., 2018). The TGO is searching for traces of methane and other atmospheric gases that could be signatures of active biological (see subsection 3.1.1) or geological processes. It is also fundamental because of the presence of the Colour and Stereo Scientific Imaging System (CaSSIS), the main high resolution imaging system on the spacecraft. Through this camera, it is possible to obtain stereo images, thanks to the mechanism of rotation or inclination of the camera, and informations of the surface in four colors, within the visible to the near infrared range. Using stereo images, high-resolution digital terrain models (DTMs) can be generated and also 3D images of the Martian surface, which would allow high-resolution morphometric studies. The CaSSIS camera is designed to acquire high-resolution images ($\sim$4.6 m) of Mars: a fundamental mean to have detailed geological and geomorphological studies of landing sites. The scientific goals achievable with the CaSSIS camera are: i) to characterize sites with probable gas emitting sources; ii) to investigate the dynamic processes

that occur on the surface of Mars and iii) to identify and to analyse potential future landing sites (Thomas et al., 2017).

The second part of the mission will be launched in 2020, when the ESA Rosalind Franklin rover will be sent to the Martian surface (Ribes-Pleguezuelo et al., 2019). The aims of the mission are: i) to analyse the Martian terrain to find traces of life, present or past, digging into the ground for a maximum depth of two meters; ii) to get a more detailed characterization of the Martian environment; iii) to characterize the distribution of water and iv) to identify possible risks for future human missions on the surface of the Red Planet (Vago et al., 2017). The landing site of this rover, the Oxia Planum region, was chosen because it is safe from an engineering point of view and because it is interesting scientifically, especially for exobiological studies.

3.1.1 Biosignatures

In its past history Mars had a dense atmosphere that allowed water to be liquid on its surface. The chemical composition of the volcanic gases could have created a place favorable to the formation of organic molecules, but with the decreasing of the greenhouse effect there was not the presence of liquid water on the surface anymore. However, water is still present in the polar ice caps, in the atmosphere and it is possible it is also present in the underground (Galletta and Sergi, 2005; Orosei et al., 2018). For this reason, the resulting atmosphere could not shield anymore the possible organic material formed on the surface, which was probably destroyed by the UV rays (Galletta et al., 2010). Therefore, if life formed in the past on Mars, it could be still present on the planet in the underground or, if it is extinguished, traces of them could be found (Galletta et al., 2010).
On Earth, life forms release more ^{12}C than ^{13}C, such that in nature their ratio R=^{13}C/^{12}C is lower if there is presence of life. The standard value for this ratio (R_{VPDB}) was identified in the isotopic ratio measured in the Belemnitella americana fossil. An index to identify life forms is: δC^{13}[‰]=[R/R_{VPDB}-1]*1000, that decreases in time if there is biological material. The δC^{13} sometimes is alterated by external factors, like the presence of methane, that could be of biological origin or not, in this second case, the δC^{13} is as low as the first case, giving a false positive (Galletta and Sergi, 2005). If that was also the case on Mars, then we would see the same trend. That is why one of the targets of the ExoMars mission is to search for methane (CH_4) and the processes that form it. Other atmospherical gases, that could indicate presence of life and that are searched, are also oxygen (O_2), ozone (O_3), water (H_2O), carbon dioxide (CO_2), which could indicate an active biosphere (Briot et al., 2013).

3.2 Landing sites

To select landing sites on Mars, the accomplishment of both scientific and engineering constrains are needed. The engineering ones are related to the landing and roving safety, the scientific ones are related to the searching for areas that in the past were suitable for life.

3.2.1 Engineering requirements

Engineering constrains have to be satisfied during the landing and roving phases and some of them are due to the fact that the hardware and electronics of the rover must be exposed to the harsh environment of Mars for a long period (Golombek et al., 2003; Pajola et al., 2016b; Pajola et al., 2019). They concern:

- Latitude and longitude: If the rover has solar panels, landing sites are chosen in the equatorial region, where there is the maximum insolation. Instead if it has a radioisotope thermoelectric generator, the landing region can be extended to higher latitudes;

- Elevation: It is needed to have a sufficient braking mechanism during the EDL phases. The elevation values refer to the Mars Global Surveyor-Mars Orbiter Laser Altimeter (MOLA) (Smith et al., 2001);

- Landing ellipses dimensions and orientation: They are chosen based on the spacecraft entry angle into the atmosphere, on the atmospherical density, on the aerodynamic resistance and on the mass of the spacecraft. Because of the uncertainties in the estimates of these factors, it is impossible to know exactly the point where the spacecraft will land. In order to have a prediction of the landing area, numerous numerical simulations are needed;

- Slopes at different length scales: They are generated with the GIS software, used for the generation of digital terrain models (DTMs), that are 3D representations of the surface. They are necessary to guarantee slope and incidence compatible with the radar on the rover, a correct fuel consumption in the descent phase, an altitude error during the landing and stability in this phase;

- Rock abundances: It is necessary to calculate the probability of crashing of the rover in the landing and roving phases. This abundance is extracted using the Viking Infrared Thermal Mapper (IRTM) data (Christensen, 1986) or, if accessible, the Mars Global Surveyor-Thermal

Emission Spectrometer (TES) data (Nowicki and Christensen, 2007). To calculate this probability, a counting of rocks is needed, manually or automatically, using HiRISE images with high resolution and then it is also needed to study their surface density and diameter distribution;

- Dust coverage: It is needed to identify possible regions with material deposits on the surface, that would prevent the rover from moving. In this case the Dust Cover Index (DCI) map (Ruff and Christensen, 2002) obtained from the TES data is used;

- Thermal inertia: It is given by the thermal limits of the rover and it is used to identify a dust-free landing site. Its measure unit is the Thermal Inertia Unit (TIU) i.e. $\frac{J}{m^2 s^{\frac{1}{2}} K}$. For this purpose the MGS-TES global night-side and day-side seasonal thermal inertia maps are used (Putzig et al., 2005; Putzig and Mellon, 2007);

- Albedo: It is given by the thermal limits of the rover and by the temperature supposed by Mars surface. It is obtained using the MGS-TES map (Christensen et al., 2001);

- Radar reflectivity: It is fundamental to the functionality of the radar on the rover and for the calculation of particle diffusion during data transfer to the orbiter. The required values are derived from the Mars Advanced Radar for Subsurface and Ionosphere Sounding (MEX-MARSIS) global reflectivity map (Mouginot et al., 2010).

Atmospheric factors have to be evaluated in the landing site choice, because they could be critical in the EDL phases, and they are:

- Sensitivity to the air density variations, caused by aerodynamic forces in the descent phases, and sensitivity to the vertical winds, to which lander and rover, that use rockets to brake, are subject to in the descent phases (Vasavada et al., 2012);

- Sensitivity to the mean horizontal winds, to which the rover is sensitive in the deceleration caused by the parachute during the descent phase. Uncertainties on the horizontal wind speed increase the size of the landing ellipse (Rafkin and Michaels, 2003);

- Sensitivity to the wind shear, that can produce oscillations of the EDL system (Kass et al., 2003).

3.2.2 Scientific requirements

According to the scientific criteria to choose a landing site, as specified in Mustard et al. (2013), the mission's aims are to:

- explore an astrobiologically relevant ancient environment on Mars to decipher its geological processes and history, including the assessment of past habitability;
- assess the biosignature preservation potential within the selected geological environment and search for potential biosignatures;
- demonstrate significant technical progress towards the future return of scientifically selected, well-documented samples to Earth;
- provide an opportunity for contributed instruments from Human Exploration or Space Technology Programs.

From a scientific point of view the landing sites are chosen because they are interesting for exobiological studies and to obtain a detailed characterization of the Martian surface, useful also to identify possible risks for future human missions. To satisfy the scientific requirements, maps of Mars suface have to be created using GIS software, that can show the geological units of the soil and the mineral components (Pajola et al., 2016a). A site can be interesting because:

- it has lands able to preserve life forms, developed in past epoches;
- it has hydrothermal sediments and rocks made by minerals that indicate aqueous phases, like phyllosilicates, carbonates and sulphates;
- there are morphological criteria related to fluvial activities, like delta deposits and valleys;
- the past presence of water and glacial activities can be identified;
- it is made by regions of Noachian/Pre-Hesperian age (>3.5 Ga), where sedimental deposits, craters and not altered igneous rocks are visible;
- there is a volcanic unit of Hesperian or Amazonian age, characterized morphologically and mineralogically;
- it is a potential area where future human exploration missions could take place.

3.3 The Oxia Planum region

The Oxia Planum region is situated in the quagrangle of Oxia Palus. It is located between the south west of Arabia Terra and the norther part of Chryse Planitia, between Mawrth Vallis and Ares Vallis and at the outlet of Cogoon Vallis (Quantin et al., 2015; Quantin et al., 2016, Pajola et al., 2017) (Figure 2.1).
It has been chosen as the landing site of the future ExoMars ESA 2020 rover, because it is a safe region from engineering perspective, since it satisfies main parameters for the landing and roving phases. It is indeed situated on a large basin, the ground is flat and smooth and therefore it provides a large landing ellipse (Quantin et al., 2016; Carter et al., 2016).
It has been chosen because it is also scientifically interesting and it is important for exobiological studies. It is characterized by large clay sedimentary deposits made of magnesium and iron phyllosilicates, discovered through the the OMEGA data (in the near infrared range with a pixel scale of 2.5 km/pixel) and the CRISM multispectral data (in the visible and IR range with a pixel scale of 200 m/pixel). All these clay deposits were originated in the Noachian epoch. Afterwards, they have been covered by an Amazonian volcanic unit. Exhumation happens after the erosion of this last event (Quantin et al., 2015; Quantin et al., 2016).
Part of the freshest phyllosilicate rich surfaces is younger than 100 Ma, basing on crater counting studies. This young surface exposure age is a potential sign of preservation of biosignatures from cosmic rays during the past 4 Ga (Quantin et al., 2015). In this region various fluvial morphologies are visible and they provide information about the water history of the region. These structures are valleys or inverted channels and a delta fan at the outlet of the Cogoon Vallis (Figure 3.1). This fan has a flat surface and the material seems constituted by fine grains, discovered through the THEMIS thermal inertia, hence suggesting it could be a delta fan. This delta implies a second period of alteration in Oxia (Quantin et al., 2016). Oxia Planum is also characterized by the presence of hydrated silicates deposited in the Noachian era (age$>$3.7 Ga), the epoch where liquid water was still present on Mars surface. In the region there are also morphologies related to phenomena of volcanism and erosive processes that occurred in the Amazonian age (age$<$3.0 Ga) (Quantin et al., 2016; Pajola et al., 2017).

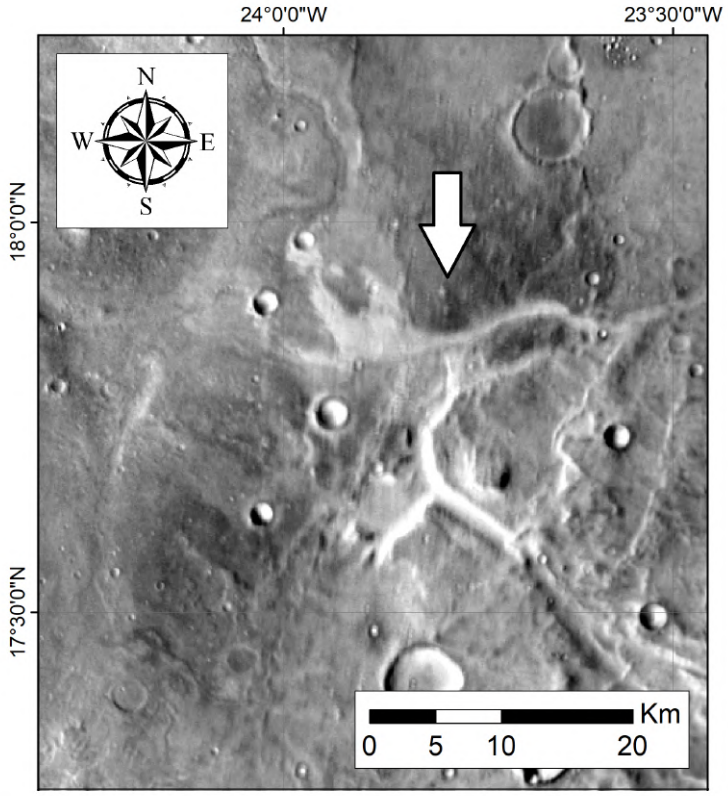

Figure 3.1: The deltaic system at the outlet of the Cogoon Vallis in the Oxia Planum region. THEMIS map is in background.

3.3.1 The Oxia Planum ExoMars landing ellipse

The landing ellipse in Oxia Planum is centred at 18.14° latitude north and -24.35° eastern longitude at a mean MOLA elevation of -3049.17±46.90 m. The maximum elevation in the ellipse is -2857 m and the minimum one is -3127 m. In Table 3.1 we show the orientation of the landing ellipse, the latitude and longitude of its centre and the dimensions of the semimajor axis and the semiminor axis.
The landing ellipse is characterized by three ellipses that are of 1σ, 2σ and 3σ (Figure 3.2), where there is respectively the 68%, 95% and 99.7% of probability that the rover might landing in those places.

Orientation (azimuth)	103.90°
Latitude (N) of the centre	18.14°
Longitude (E) of the centre	-24.35°
Semimajor axis	44.15 km
Semiminor axis	2.40 km

Table 3.1: Orientation (from the north direction, counted in the clockwise direction) of the landing ellipse, latitude and longitude of its centre and the dimensions of the semimajor axis and the semiminor axis.

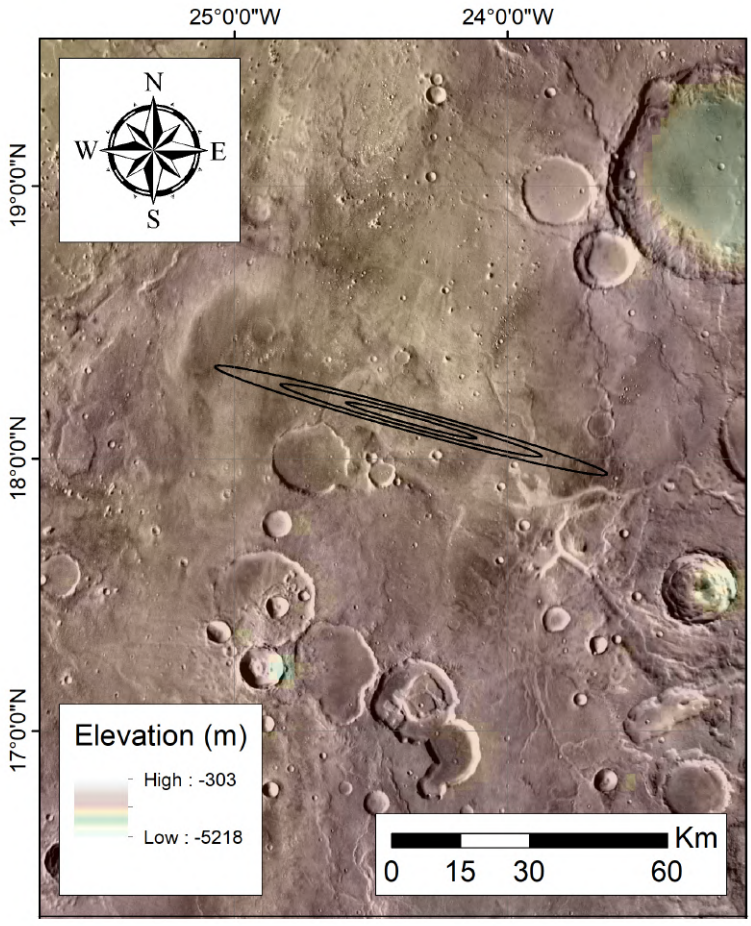

Figure 3.2: MOLA context map showing the landing ellipse for the ExoMars 2020 mission in the Oxia Planum region. THEMIS map is also in the background.

We divided the larger ellipse into different regions by analysing THEMIS images and considering the different daylight thermal inertia values present on the area (Nowicki and Christensen, 2007; Putzig et al., 2005; Putzig and Mellon, 2007) (see subsection 3.2.1) (see Table 3.2). In Figure 3.3 we can distinguish these areas that are an Amazonian volcanic unit (Av) and three different exhumed Noachian units (Nc1, Nc2, Nc3), all characterised by different thermal inertia values. Nc1 and Nc2 were separated even if they have a similar thermal inertia because they are located on opposite sides with respect to the Amazonian unit. Moreover, in the same figure we can identify also Amazonian patches located in Nc2, as indicated in Pajola et al. (2017). A 98.76% of the landing ellipse is situated in a late Noachian unit while a 1.24% lies on a middle Noachian unit, according with the global geologic map units by Tanaka et al. (2014) (Figure 3.4).
In Table 3.3 we indicate the areas of the different regions.

Unit	Av	Nc1	Nc2	Nc3
Minimum value (TIU)	370	325	329	249
Maximum value (TIU)	512	469	512	421
Mean (TIU)	439	390	385	290
Standard deviation (TIU)	44	35	46	34

Table 3.2: Thermal inertia values, the mean and the standard deviation for all units.

Region	Area
Smaller ellipse area (E1)	35111 m^2
Middle ellipse area (E2)	140451 m^2
Larger ellipse area (E3)	316015 m^2
Amazonian volcanic (Av)	36193 m^2
Exhumed Noachian unit 1 (Nc1)	81004 m^2
Exhumed Noachian unit 2 (Nc2)	48433 m^2
Exhumed Noachian unit 3 (Nc3)	154119 m^2
Late Noachian highland unit	39986.10 km^2
Middle Noachian highland unit	166062.00 km^2

Table 3.3: Areas of the ellipses and of the different regions identified in the larger ellipse and of the two Noachian global highland units.

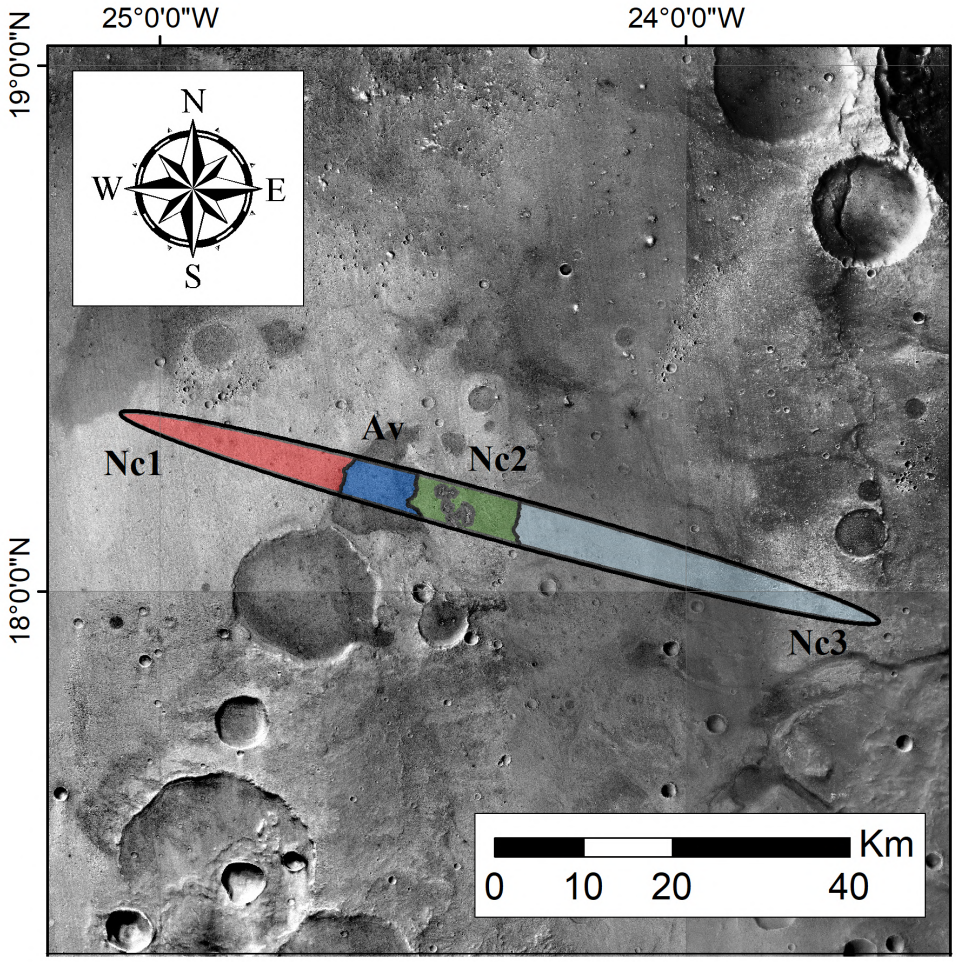

Figure 3.3: Amazonian and exhumed Noachian units in the landing ellipse. The grey patches identified in the Nc2 are remnants of the Amazonian volcanic unit that was once covering this region. This is a CTX image.

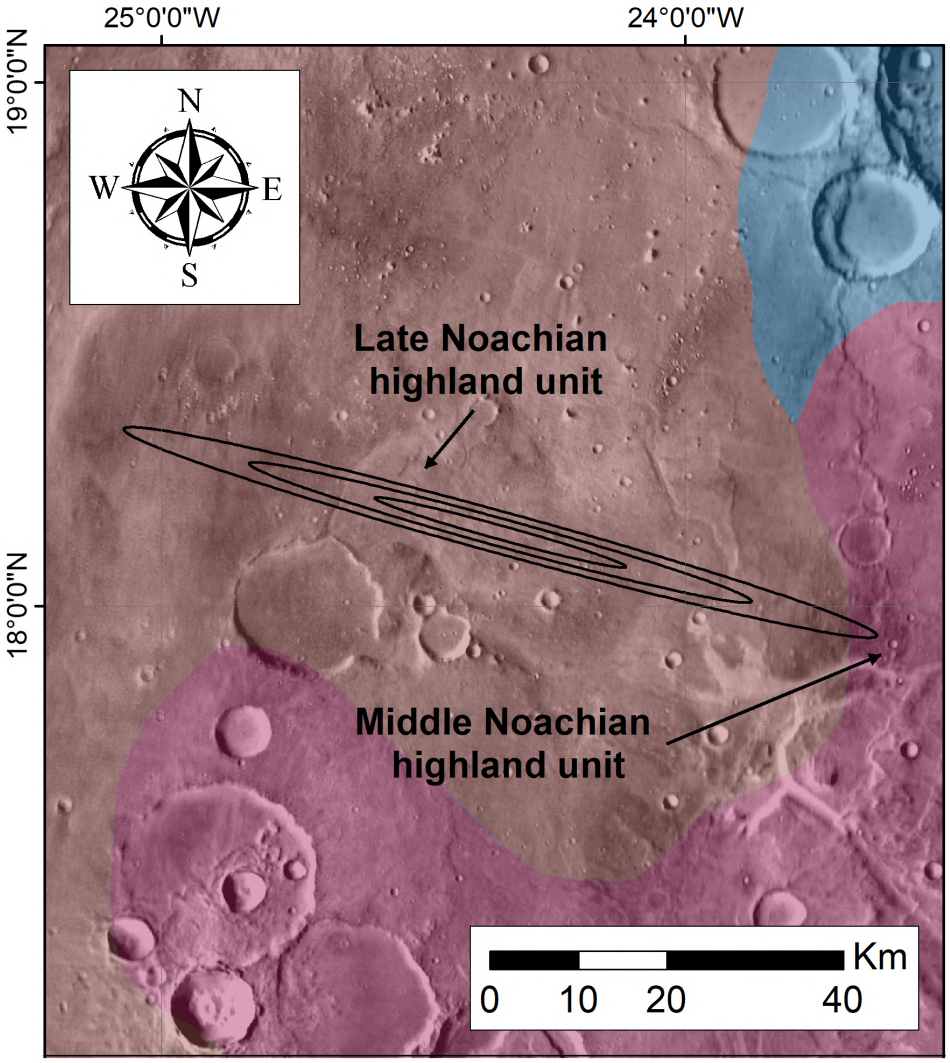

Figure 3.4: The Oxia Planum region with the global geological limits identified by Tanaka et al. (2014). Different colored areas correspond to different geological units and surface exposure ages. THEMIS map is in background.

Through the extraction of the MOLA DTM values (Smith et al., 2001) (see Table 3.4), we computed the elevations for the four units identified. This was done to understand if those units characterised by similar or different thermal inertia are situated on similar or different elevations (Figure 3.5) (Figure 3.6).

Unit	Av	Nc1	Nc2	Nc3
Minimum value (m)	-3110	-3101	-3127	-3076
Maximum value (m)	-3049	-3020	-3054	-2821
Mean (m)	-3083	-3068	-3093	-3007
Standard deviation (m)	20	21	22	54

Table 3.4: The minimum and the maximum value, the mean and the standard deviation obtained from the profile in elevation of the different units inside the landing site.

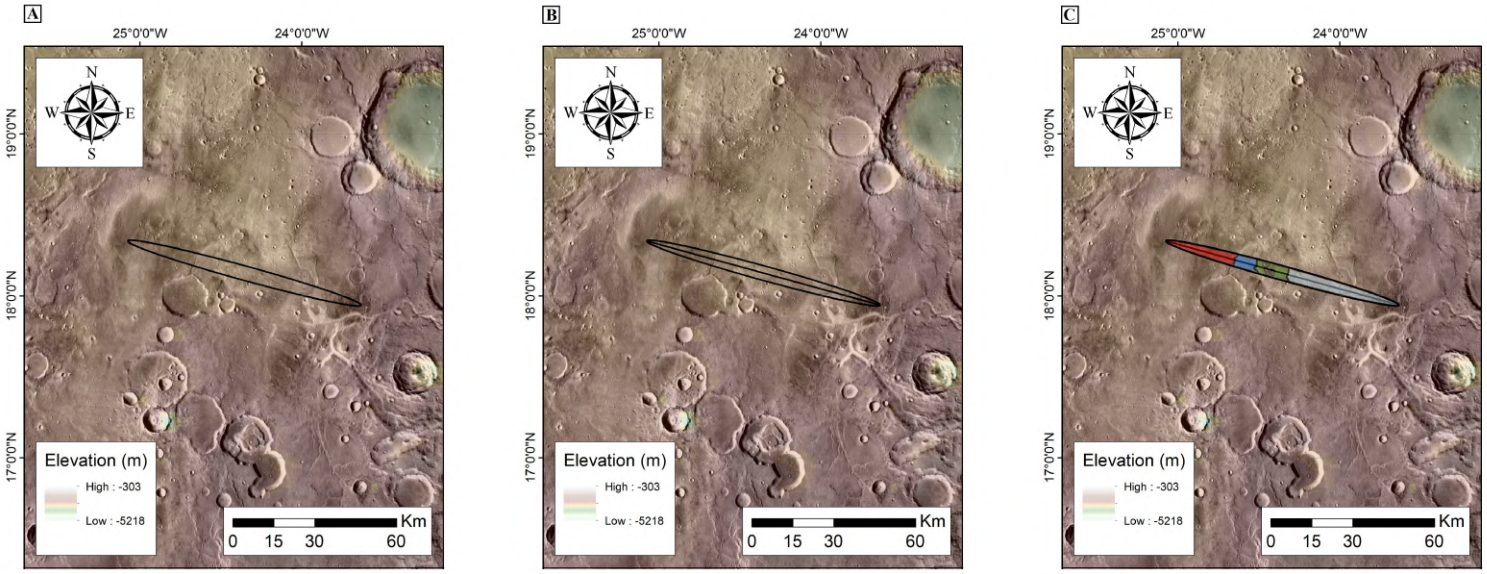

Figure 3.5: In the panel A the landing ellipse is showed. In the panel B the line on which we made the profile is added. In the panel C the different unit (Amazonian one and the three exhumed Noachian ones) are also showed.

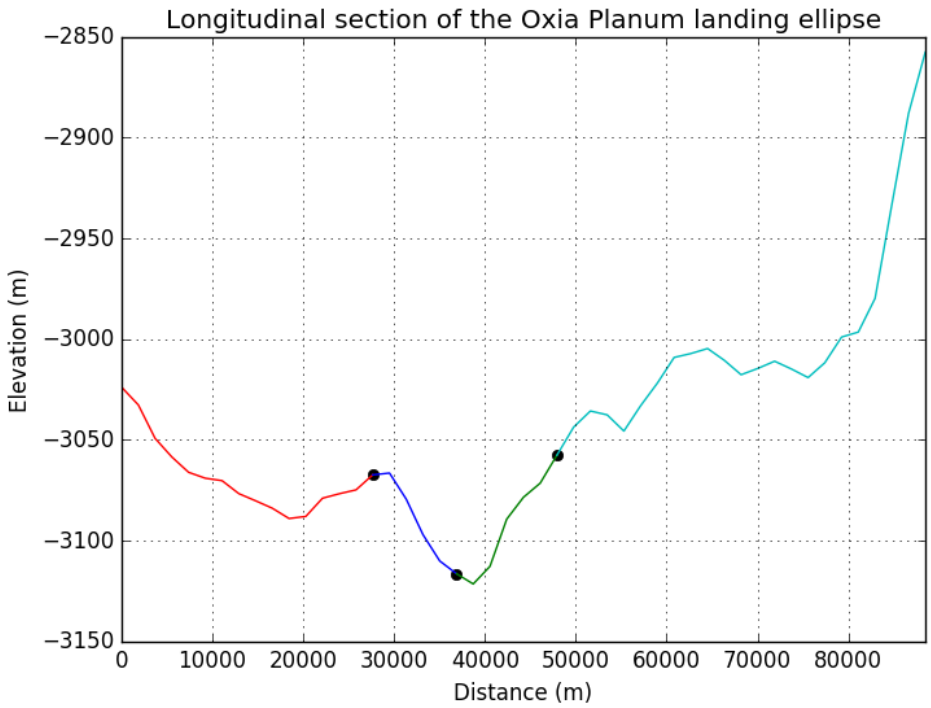

Figure 3.6: Longitudinal section of the Oxia Planum landing ellipse. The different colours used to made the line correspond to the different units represented in Figure 3.5 in the panel C.

Chapter 4

Results and Discussion

4.1 Crater analysis and surface modelled ages

By means of the methodology indicated in the section 2.5, we identified and measured all craters both in THEMIS (see subsection 4.1.1) as well as in CTX images (see subsection 4.1.2). Through the crater counting technique, we then derived the modelled surface ages using the software "Craterstats 2" (see subsection 2.4.4). In the presented analysis the epochs boundaries of the Martian geologic history used are from Michael (2013) and the isochrons used in the cumulative fit are from Hartmann and Neukum (2001).

4.1.1 Global analysis of Oxia Planum landing area

According to the global geologic map units by Tanaka et al. (2014) we studied the two geological units where the Oxia Planum landing site is located: a middle Noachian highland unit and a late Noachian one. In the first case the area is 39986.10 km^2 and we counted on this region a total number of 556 craters. The minimum diameter in this count is 0.33 km and the maximum one is 9.36 km. Using "Craterstats 2" the modelled age we derived is 3.82 +0.02/-0.03 Ga obtained in the fitting curve range of 2 km - 60 km. On the contrary, the second unit is characterised by an area of 166062.00 km^2 and we counted a total number of 1993 craters. The minimum diameter in this count is 0.30 km and the maximum one is 9.82 km. Using "Craterstats 2" the modelled age we derived is 3.85 +0.02/-0.02 Ga obtained in the fitting curve range of 1.4 km - 60 km. The identified craters are presented in Figure 4.1, while the resulting modelled ages are in Figure 4.3 for the middle Noachian highland unit while it is in Figure 4.4 for the late Noachian one.

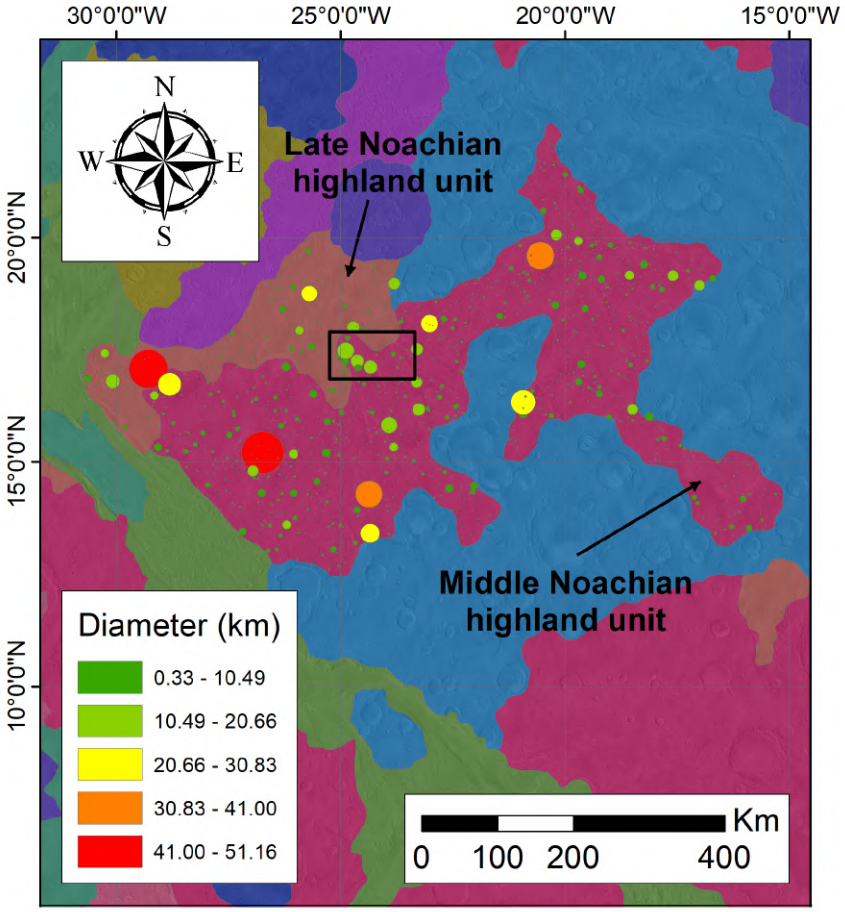

Figure 4.1: The late and middle Noachian highland units in Oxia Planum and the crater counted are showed. In the black rectangle the location of the landing ellipse for the ExoMars 2020 mission is indicated too (see Figure 4.2 in detail). The THEMIS image is superimposed in trasparency.

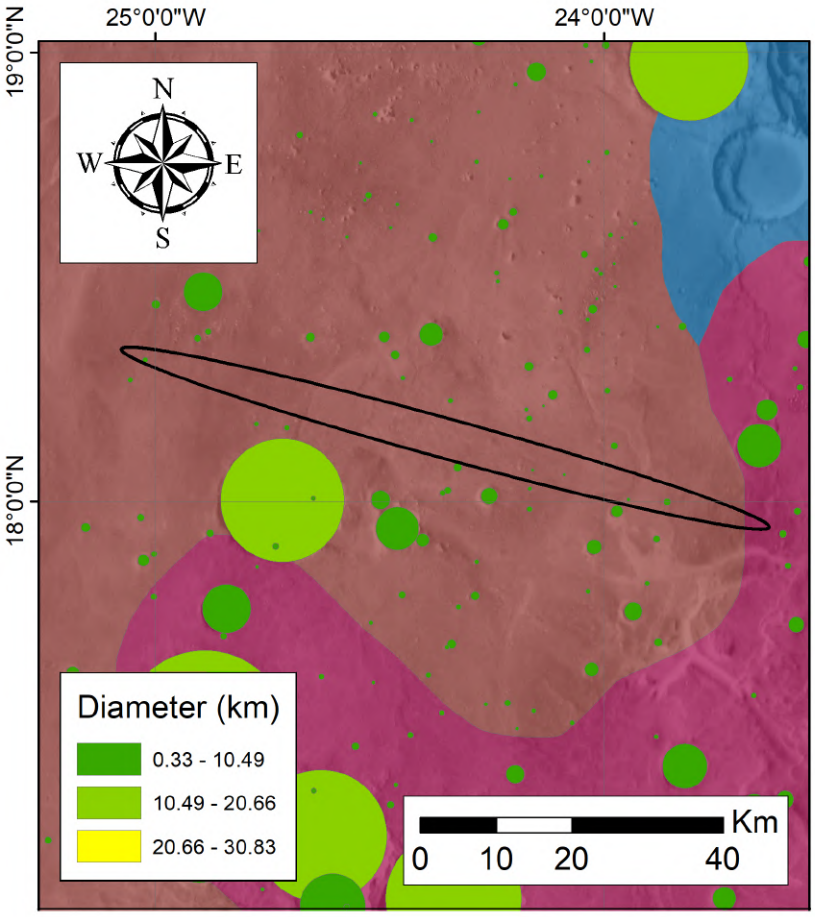

Figure 4.2: The landing ellipse located in the middle and late Noachian highland units is showed. The THEMIS imagery dataset is superimposed in trasparency.

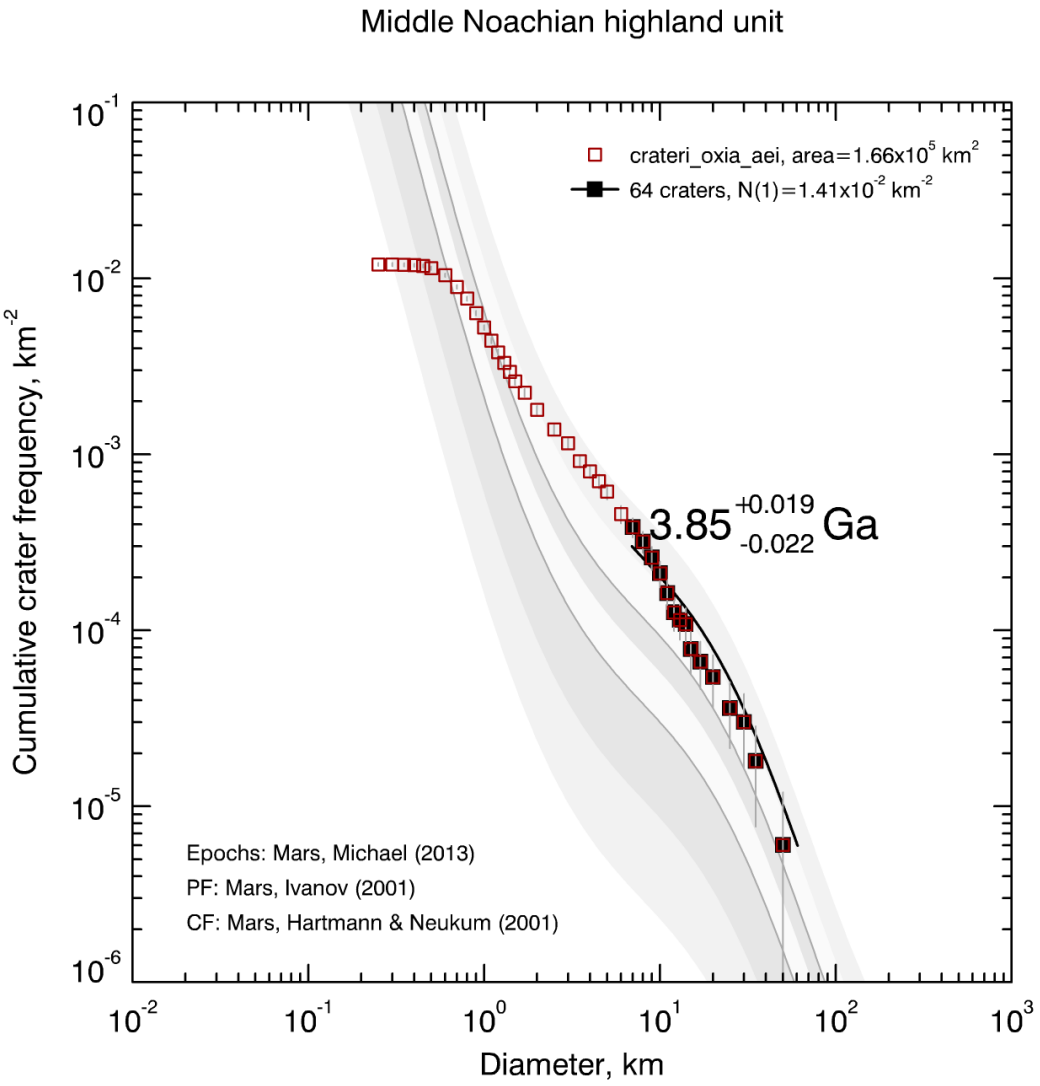

Figure 4.3: Modelled age of the middle Noachian highland unit over which the 1.24% of the ExoMars landing ellipse is located.

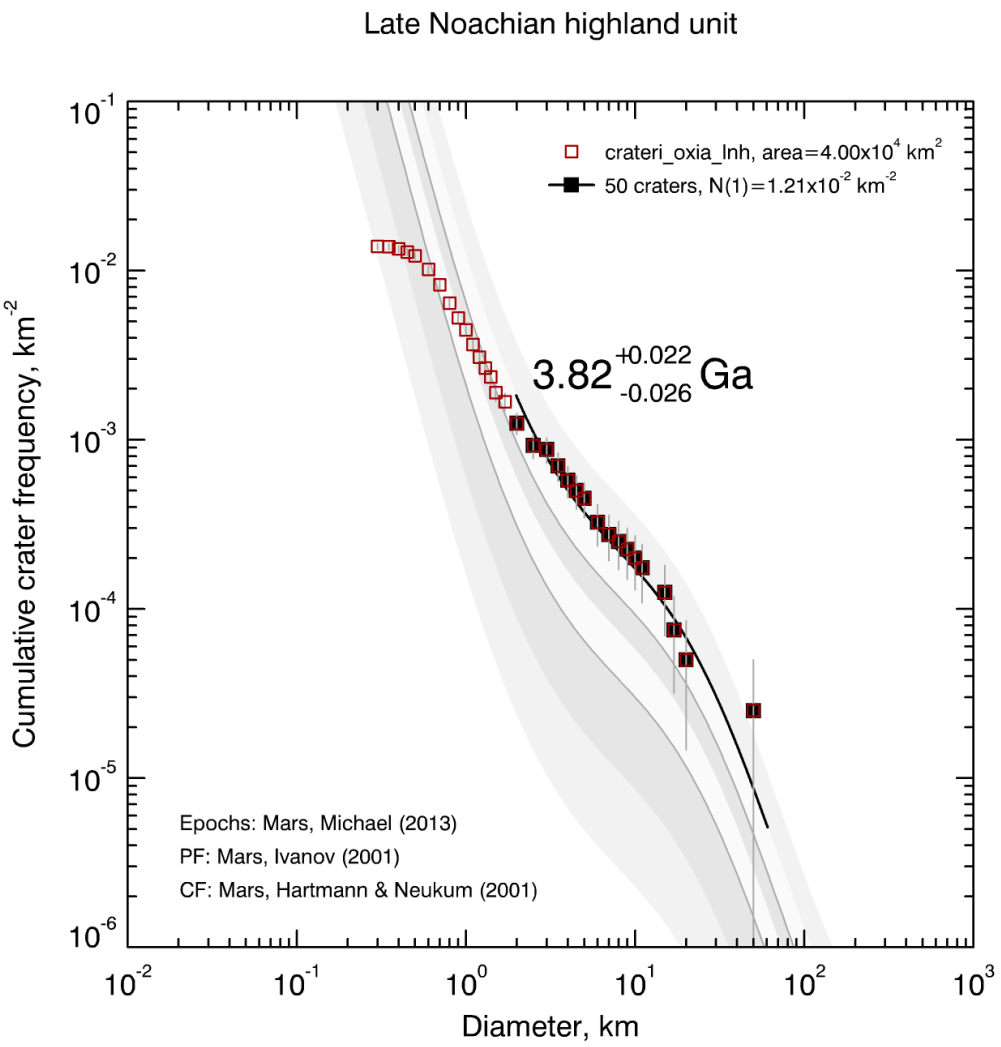

Figure 4.4: Modelled age of the late Noachian highland unit over which the 98.76% of the ExoMars landing ellipse is located.

In this work the crater count that was globally made in the Oxia Planum region was entirely accomplished on THEMIS images with a spatial resolution of 100 m. The modelled ages we obtained from the fitting curves are 3.82 +0.02/-0.03 Ga for the middle Noachian highland unit and 3.85 +0.02/-0.02 Ga for the late Noachian one. Such results are in the age range indicated in Figure 1.1, hence confirming the unit division accomplished by Tanaka et al. (2014). This result is of particular importance because we confirm that Oxia is located on Noachian terrains, hence accomplishing the requirements expected by the ExoMars mission. The Oxia planum is made by sedimental

deposits of clays indicating aqueous formation bedrocks and alteration, together with morphologies that highlight the ancient occurrence of long-term standing bodies of water. These are important astrobiological aspects, because they suggest the environment could be favourable for life occurrence and preservation. In addition, the terrain and mineralogies are well preserved hence making of particular interest the search for potential ancient biosignatures. This is the reason why the Oxia Planum region is an extraordinary site for the search of potential life on Mars.

4.1.2 Local analysis of Oxia Planum landing area

After the global identification of craters inside the two geological units identified on Oxia we focused our attention on the ExoMars 2020 final landing ellipse, making use of CTX 5.0 m resolution images. The total area of the 3σ ellipse is 316015 m^2 and inside this full region we counted 10358 crater. The minimum diameter in this count is 2.64 m and the maximum one is 810.54 m. The identified craters are presented in Figure 4.5.

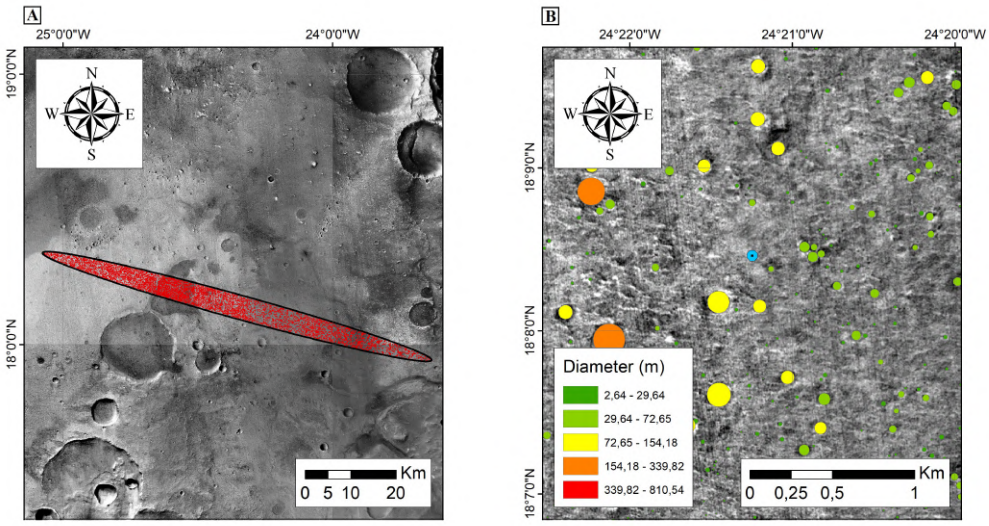

Figure 4.5: In the panel A the landing ellipse and the crater counted (in red) are showed. In the panel B the centre of the landing ellipse (in light blue), the craters counted and their dimensions are indicated. This is a CTX image.

Within the landing ellipse we identified four different regions. Three are exhumed Noachian clay rich units, while one is an Amazonian volcanic unit (Quantin et al., 2015; Quantin et al., 2016; Pajola et al., 2017).
The area of the Amazonian volcanic unit (Av) is 36193 m^2 and we counted a total number of 2123 craters. The minimum diameter in this count is 3.17 m and the maximum one is 508.83 m. Using "Craterstats 2" the modelled age we derived is 1.39 +0.56/-0.56 Ga obtained in the fitting curve range of 200 m - 600 m. The identified craters are presented in Figure 4.6, while the resulting modelled ages are in Figure 4.7.

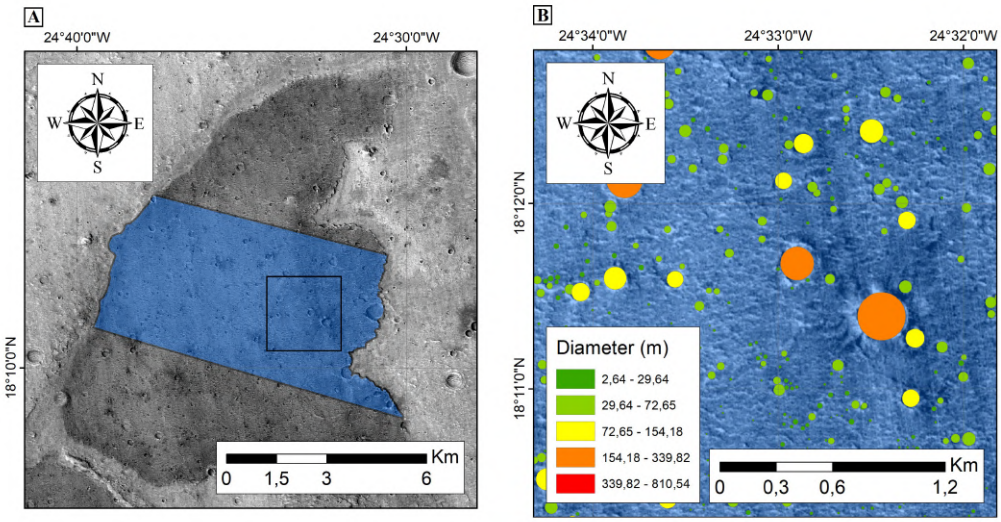

Figure 4.6: In the panel A the Amazonian volcanic unit (Av) located inside the landing ellipse is showed in the blue region. In the panel B a zoom of the black rectangle identified in the panel A is showed. This is a CTX image.

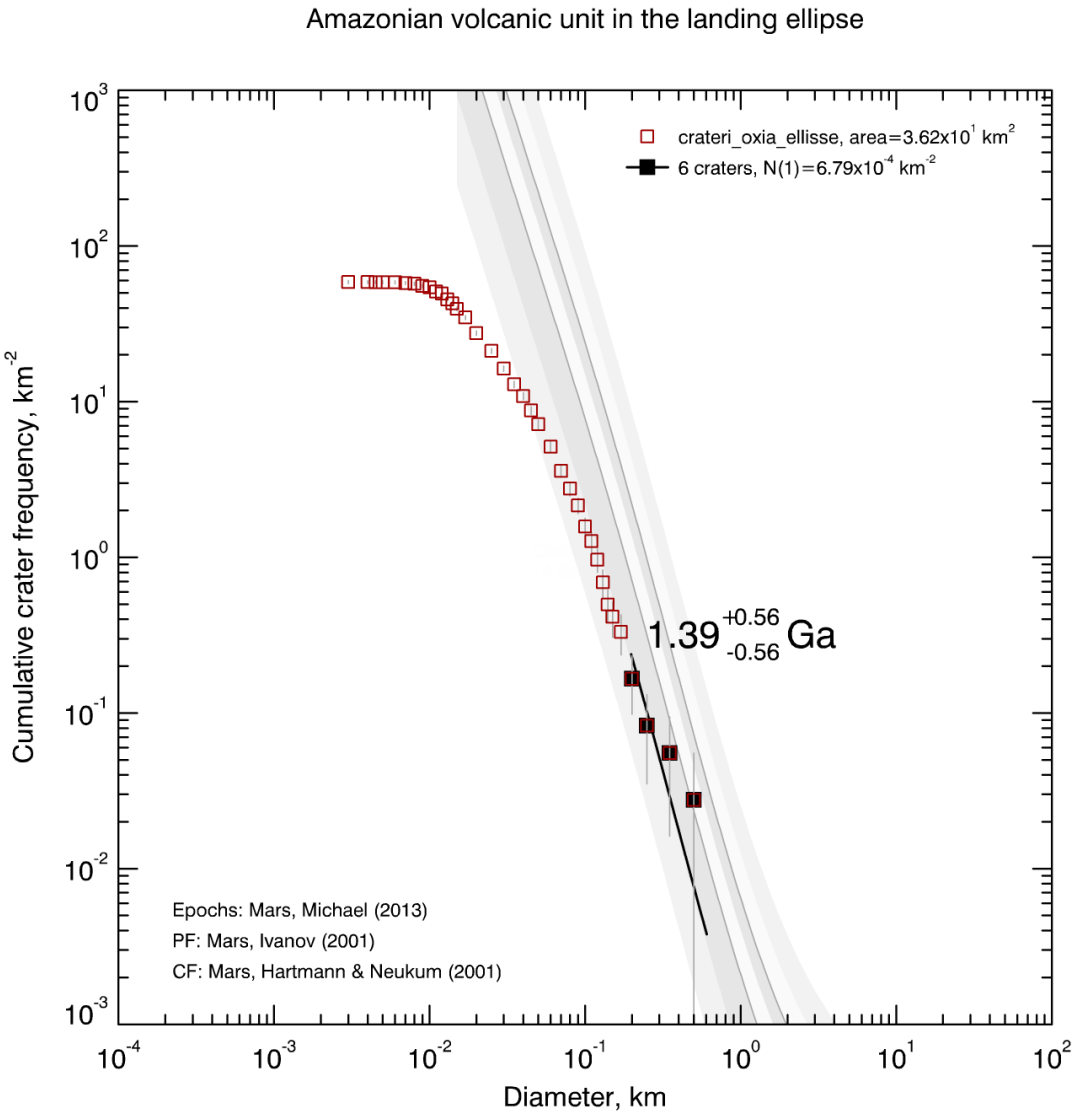

Figure 4.7: Modelled age of the Amazonian volcanic unit (Av) in the landing ellipse.

The area of the exhumed Noachian 1 unit (Nc1) is 81004 m^2 and we counted a total number of 3596 craters. The minimum diameter in this count is 3.17 m and the maximum one is 810.54 m. Using "Craterstats 2" the modelled age we derived is 607 +72/-72 Ma obtained in the fitting curve range of 100 m - 350 m. The identified craters are presented in Figure 4.8, while the resulting modelled ages are in Figure 4.9.

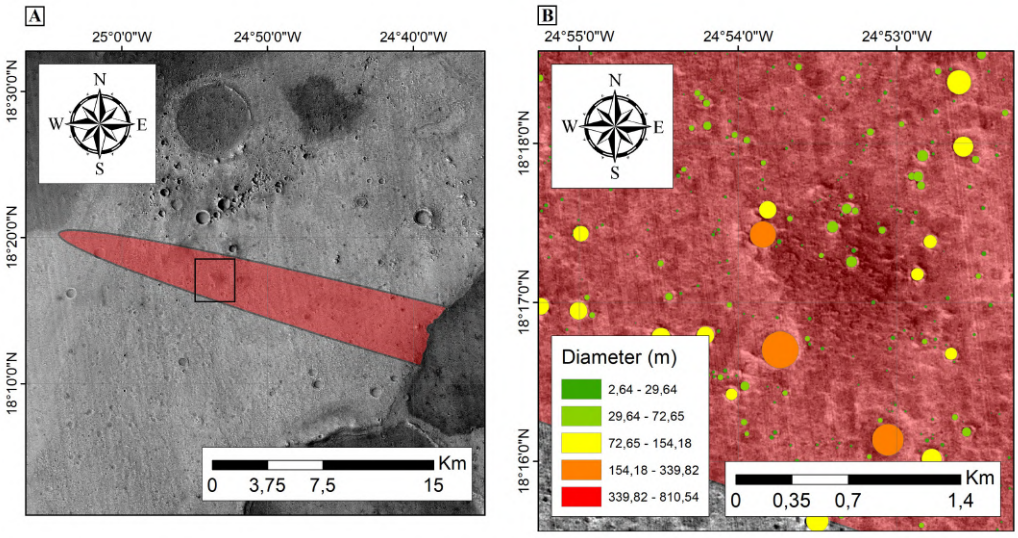

Figure 4.8: In the panel A the exhumed Noachian 1 unit (Nc1) located inside the landing ellipse is showed in the red region. In the panel B a zoom of the black rectangle identified in the panel A is showed. This is a CTX image.

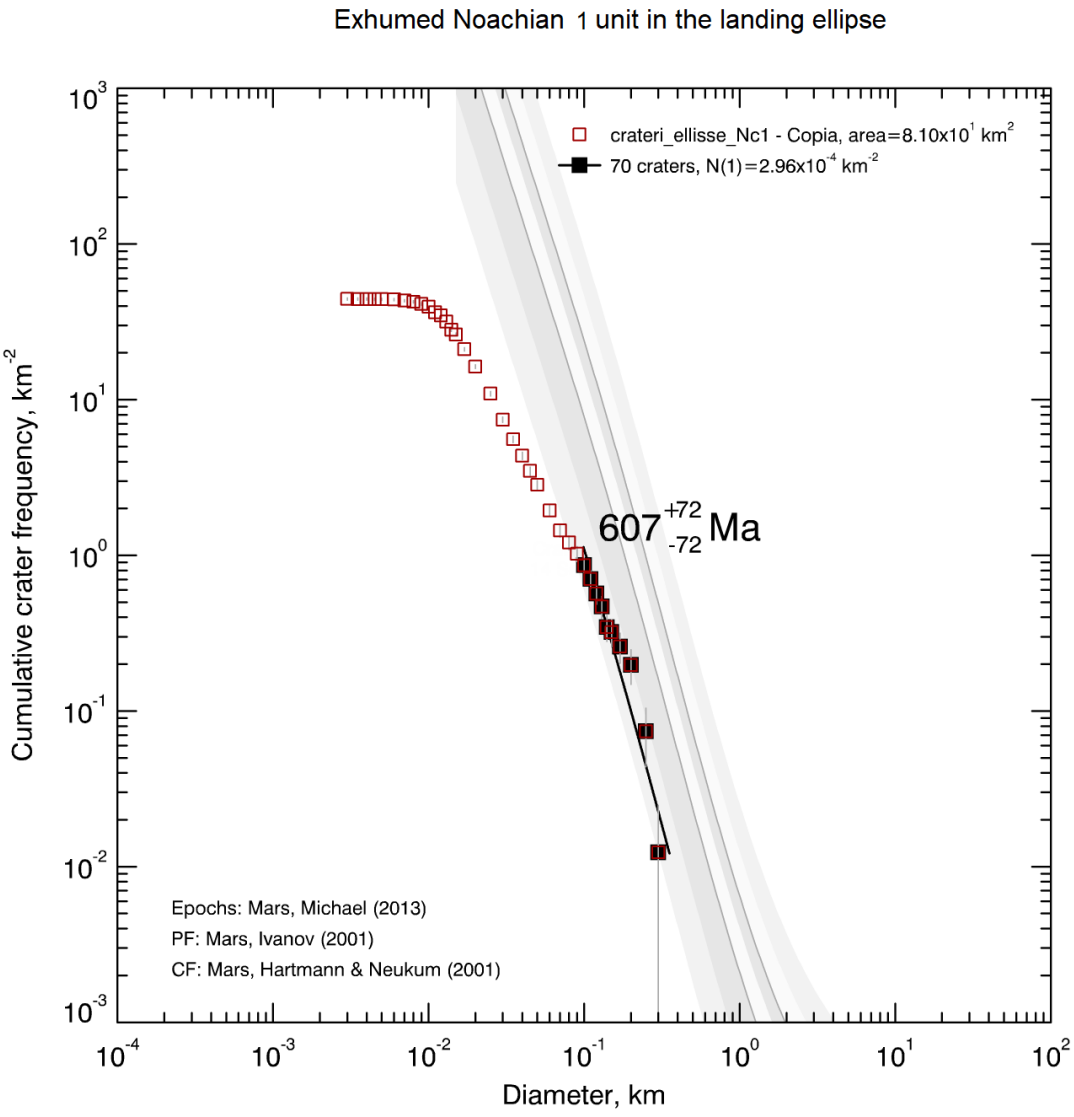

Figure 4.9: Modelled age of the exhumed Noachian 1 unit (Nc1) in the landing ellipse.

The area of the exhumed Noachian 2 unit (Nc2) is 48433 m^2 and we counted a total number of 1809 craters. When identifying and counting all craters over this area we avoided some Amazonian patches, that are located in this area, as indicated in Pajola et al. (2017). The minimum diameter in this count is 4.22 m and the maximum one is 485.21 m. Using "Craterstats 2" the modelled age we derived is 659 +120/-120 Ma obtained in the fitting curve range of 130 m - 500 m. The identified craters are presented in Figure 4.10, while the resulting modelled ages are in Figure 4.11.

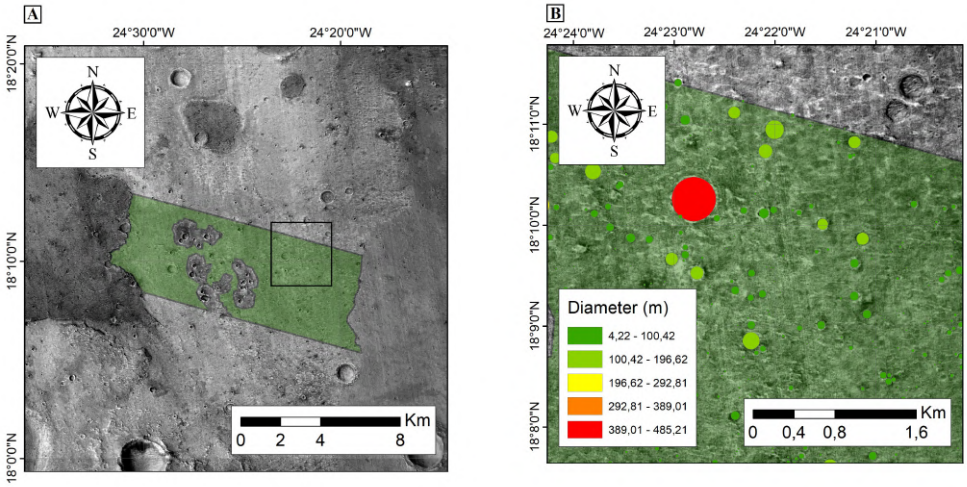

Figure 4.10: In the panel A the exhumed Noachian 2 unit (Nc2) located inside the landing ellipse is showed in the green region. We decided to not consider the Amazonian patches indicated in Pajola et al. (2017) and the corresponding craters in the area to have a single, homogeneous exhumed Noachian unit. In the panel B a zoom of the black rectangle identified in the panel A is showed. This is a CTX image.

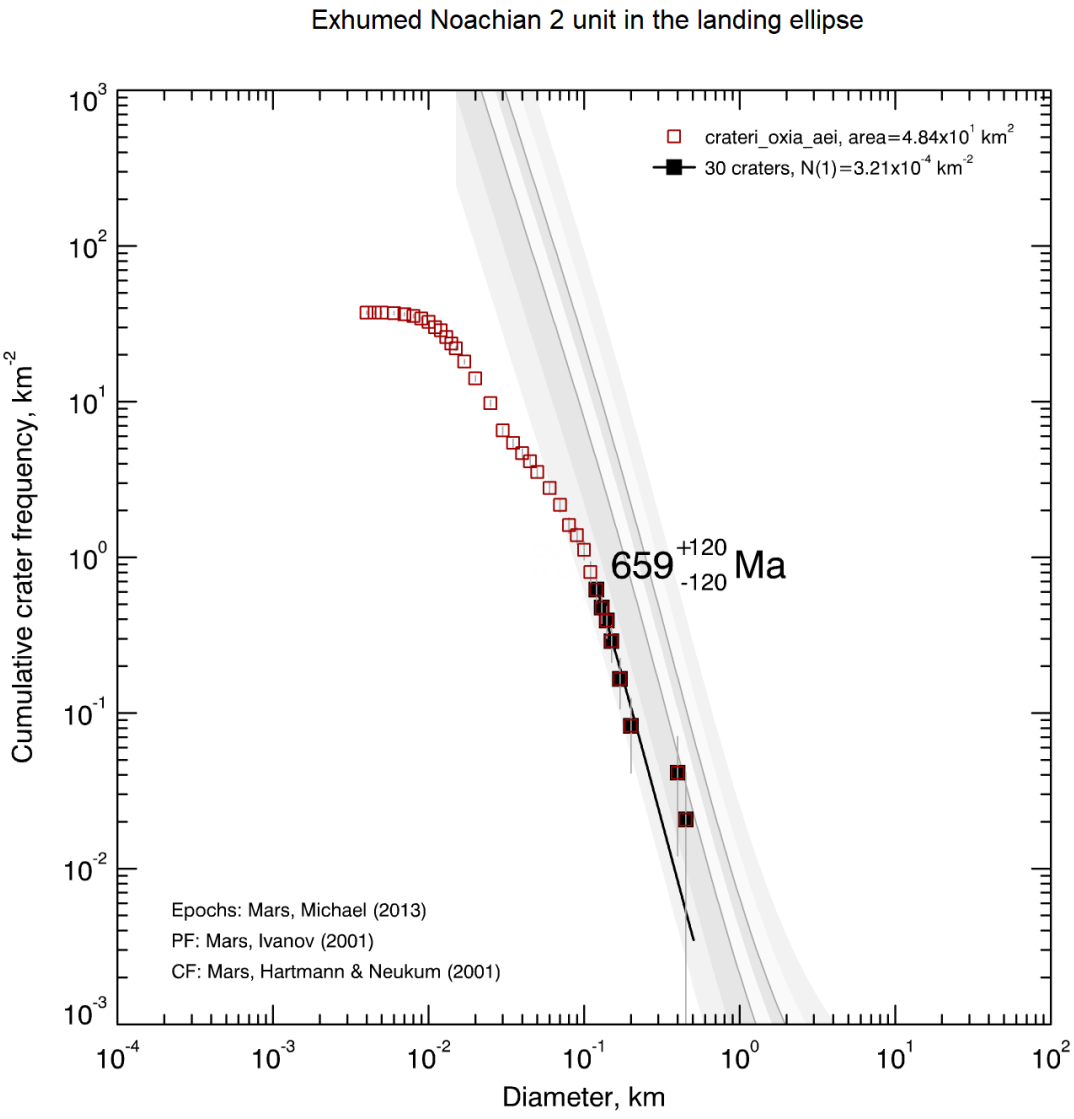

Figure 4.11: Modelled age of the exhumed Noachian 2 unit (Nc2) in the landing ellipse.

The area of the exhumed Noachian 3 unit (Nc3) is 154119 m^2 and we counted a total number of 2628 craters. The minimum diameter in this count is 5.28 m and the maximum one is 746.39 m. Using "Craterstats 2" the modelled age we derived is 1.79 +0.30/-0.30 Ga obtained in the fitting curve range of 200 m - 800 m. The identified craters are presented in Figure 4.12, while the resulting modelled ages are in Figure 4.13.

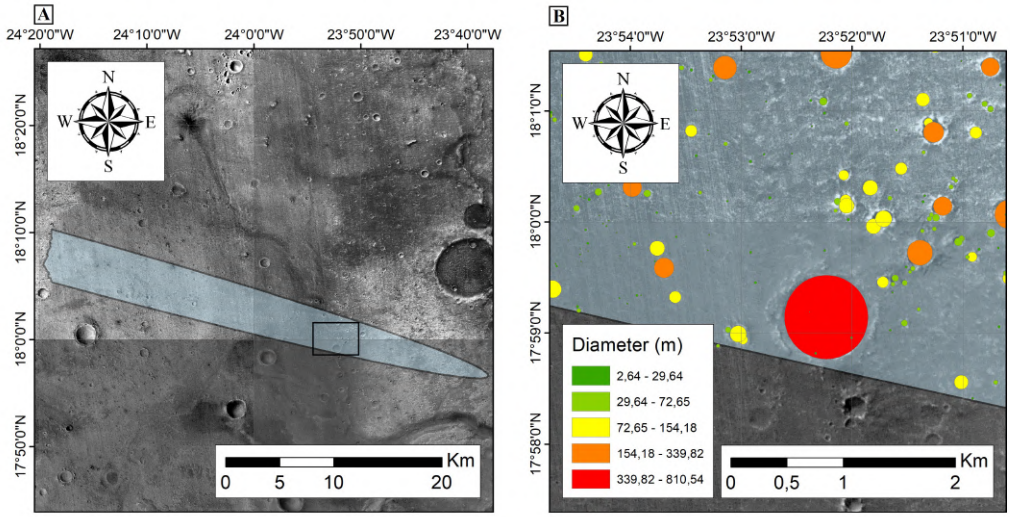

Figure 4.12: In the panel A the exhumed Noachian 3 unit (Nc3) located inside the landing ellipse is showed in the cyan region. In the panel B a zoom of the black rectangle identified in the panel A is showed. This is a CTX image.

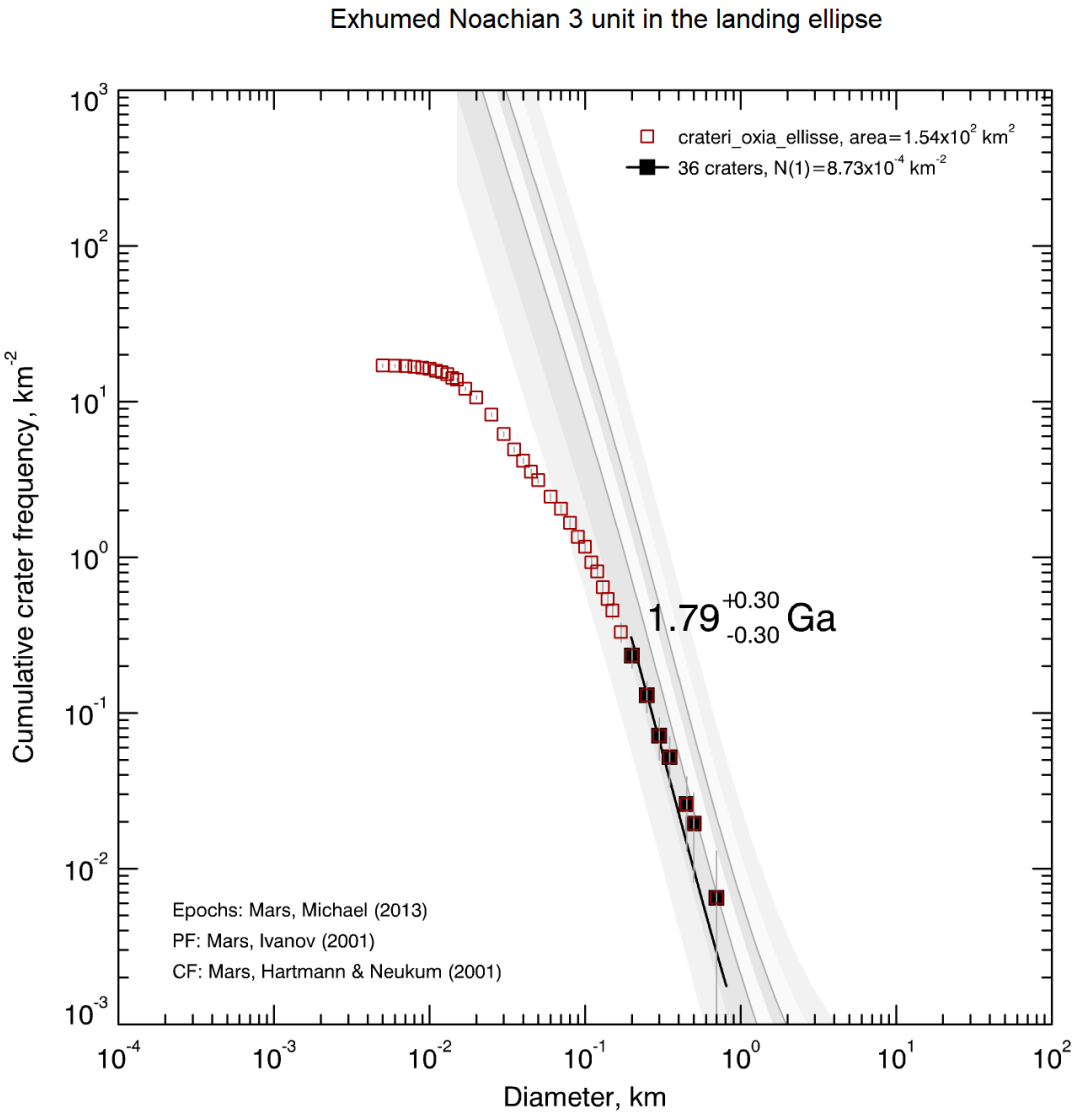

Figure 4.13: Modelled age of the exhumed Noachian 3 unit (Nc3) in the landing ellipse.

Locally analysing the landing ellipse with a crater count, the modelled ages we obtained from the fit are 1.39 +0.56/-0.56 Ga for the Amazonian volcanic unit, 607 +72/-72 Ma for the exhumed Noachian 1 unit, 659 +120/-120 Ma for the exhumed Noachian 2 unit and 1.79 +0.30/-0.30 Ga for the exhumed Noachian 3 unit. These ages are Amazonian as indicated from Figure 1.1, but they are exhumed ages. As specified in the subsection 4.1.1 these results are important because they confirm the Oxia Planum region is the right landing site for the ExoMars 2020 mission.

4.1.3 Cogoon deltaic deposits

In addition to the different terrains located on Oxia, we made the first crater count in the Cogoon deltaic deposits on CTX images presented in Figure 4.14 and in Figure 4.15.
The area of the deltaic deposits we identified is 502838 m^2 and we counted a total number of 6842 craters. The minimum diameter in this count is 1.89 m and the maximum one is 2203.25 m. Using "Craterstats 2" the modelled age we derived is 3.78 +0.05/-0.08 Ga obtained in the fitting curve range of 10^{-4}-10^{2} km. The identified craters are presented in Figure 4.16, while the resulting modelled ages are in Figure 4.17.

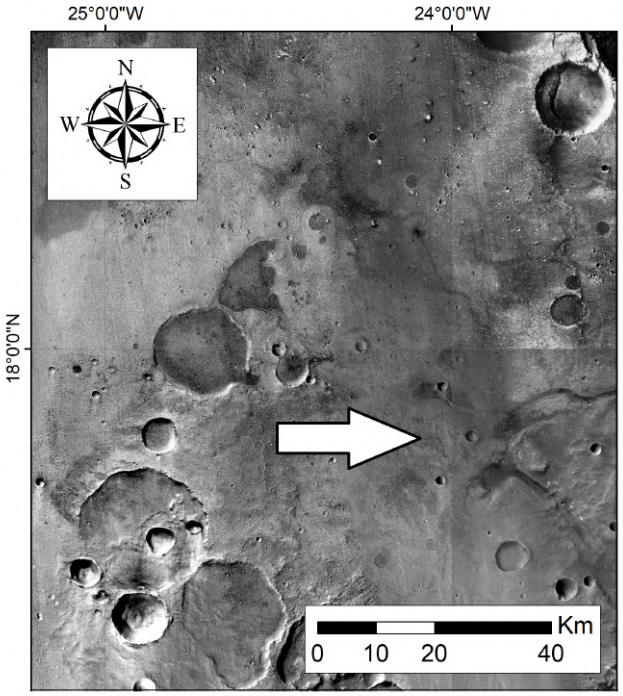

Figure 4.14: The region of Oxia Planum and the outlet of the Cogoon Vallis (white arrow) are showed. This is a CTX image.

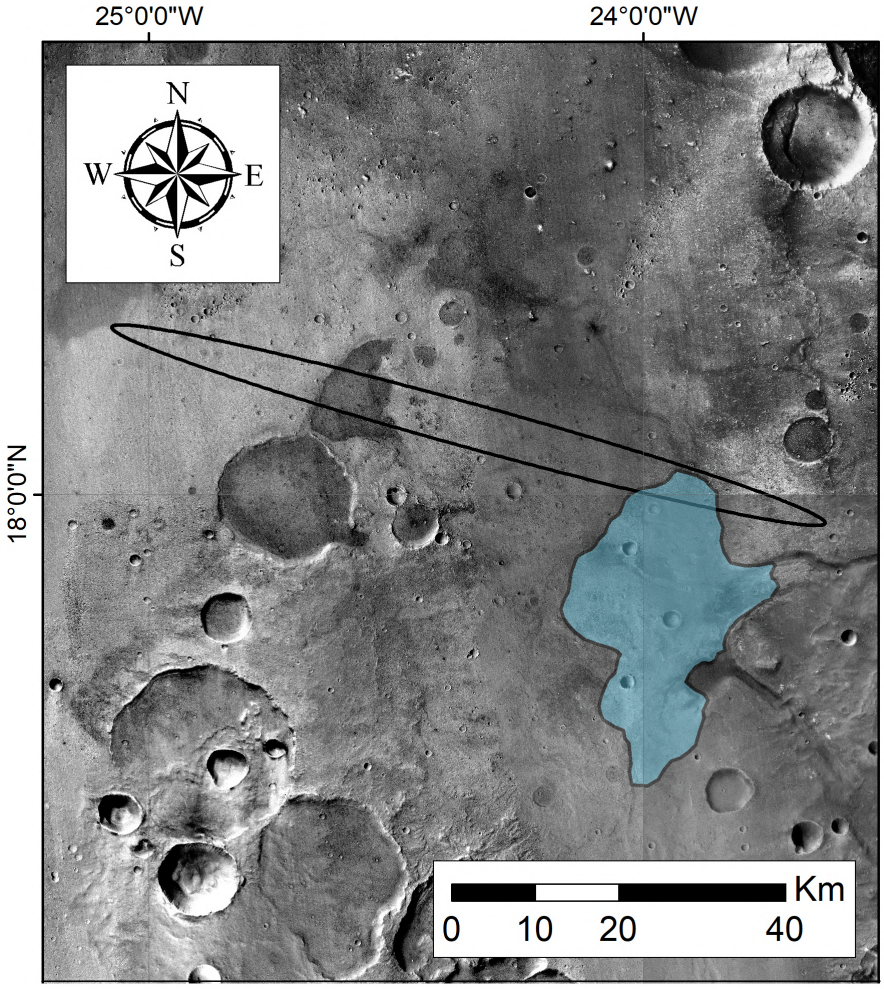

Figure 4.15: The landing ellipse and the Cogoon deltaic deposits area are indicated. This is a CTX image.

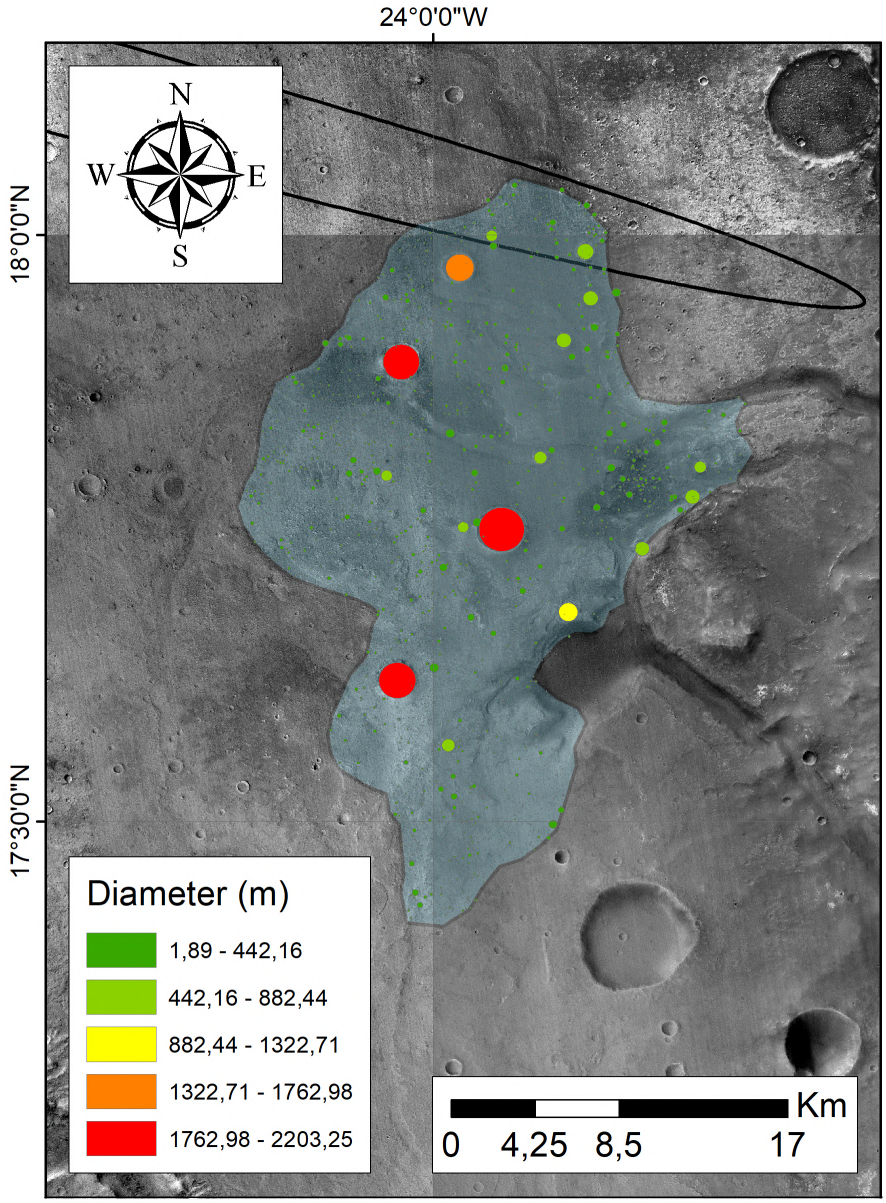

Figure 4.16: The Cogoon deltaic deposits area and the craters counted are showed.

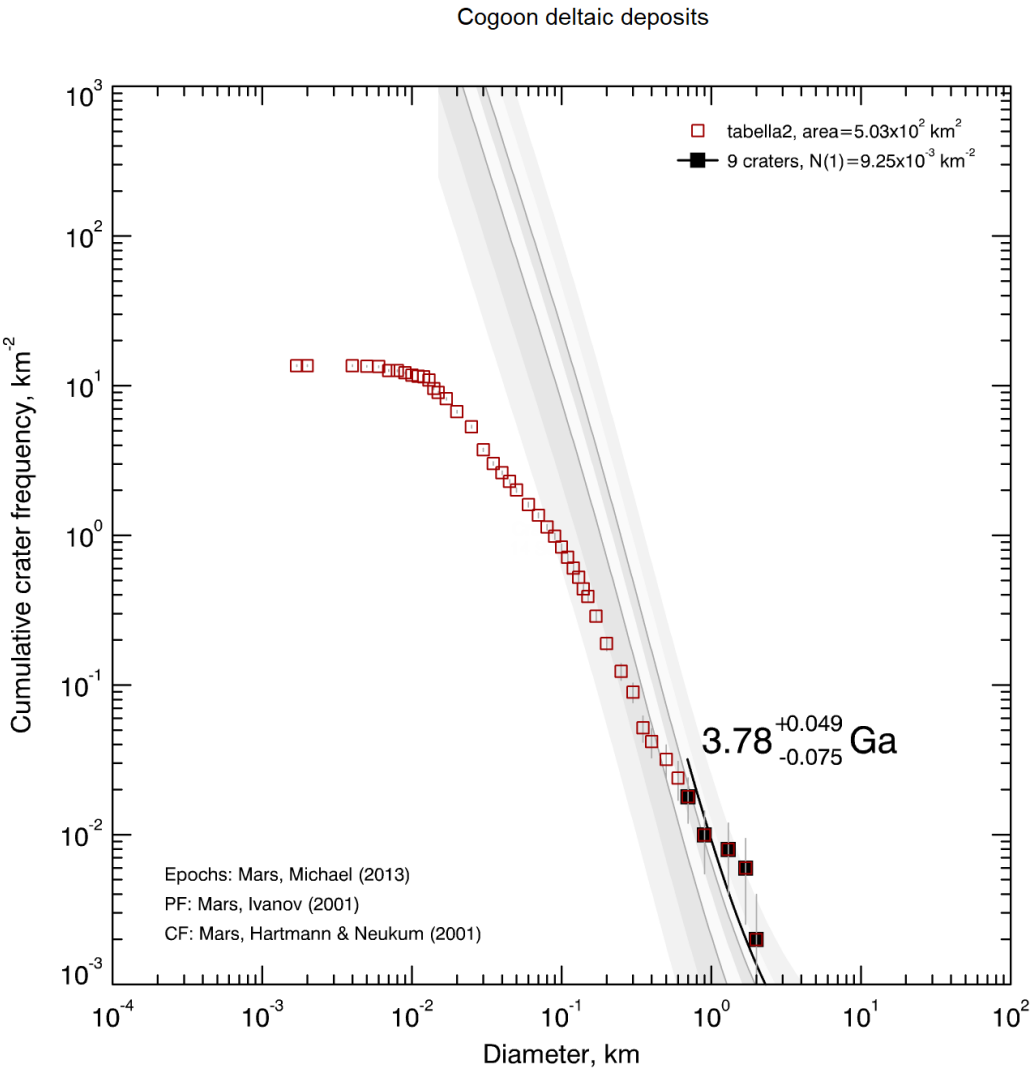

Figure 4.17: Modelled age of the Cogoon deltaic deposits.

The modelled ages we obtained from the fit is 3.78 +0.05/-0.08 Ga. This is compatible with the interpretation made in Quantin et al. (2016), where it was suggested that the delta-fan is older than 3.5 Ga. This age should indicate the last stage in which water vanished from this region.

4.1.3.1 Evolution of the Oxia Planum area

By means of the modelled age we obtained from the different units located on Oxia planum we can suggest how the area evolved through the ages.
In Figure 4.18 a sketch representing the evolution of the Oxia Planum region is showed.

- Panel A: The ancient Martian basalts deposited on the area. The resulting superimposed craters and the counts we obtained confirm that the surface exposure of such deposits is middle/late Noachian (3.85 +0.02/-0.02 to 3.82 +0.02/-0.03 Ga), i.e. an age where valleys formation, incision and a possible water cycle was expected to be active on the full surface of Mars (Carr and Head, 2010). Over this entire area, the presence of an ancient water table (paleolakes or an ancient ocean) altered all basalts into large clay deposits;

- Panel B: During this time the Cogoon valleys system incised the region and formed the delta and the deltaic deposits that are located eastwards of the ExoMars landing ellipse;

- Panel C: The modelled surface age we obtained on the Coogon deltaic deposits returns a value of 3.78 +0.05/-0.08 Ga (Figure 4.17), possibly indicating the late water pulses (Quantin et al., 2016) that occurred on the area;

- Panel D: During the Hesperian-Amazonian age volcanic deposits covered the full landing area, and its ancient clays, partially covering the Cogoon deltaic deposits too;

- Panel E: The eroded remnants of such deposits are located on the Av unit and the corresponding surface age we derived is 1.39 +0.56/-0.56 (Figure 4.7). Depending on the surface elevation the ancient Noachian deposits started to be exhumed (likely due to wind erosion) with NC3 unit being exposed around 1.79 +0.30/-0.30 Ga (Figure 4.13). On the contrary, NC1 and NC2 are located on a lower altitude with respect to NC3 and exhumed later, around 660-600 Ma (Figure 4.9 and Figure 4.11).

The exhumed Noachian 1 and 2 units have similar elevation and thermal inertia and we obtained that they have similar exhumation ages. On the contrary, the exhumed Noachian 3 unit is higher in elevation than the other two exhumed units and it was exhumed earlier than Nc1 and Nc2. The Amazonian unit instead was eroded and we derived a modelled age of 1.39 +0.56/-0.56 for its remnants.

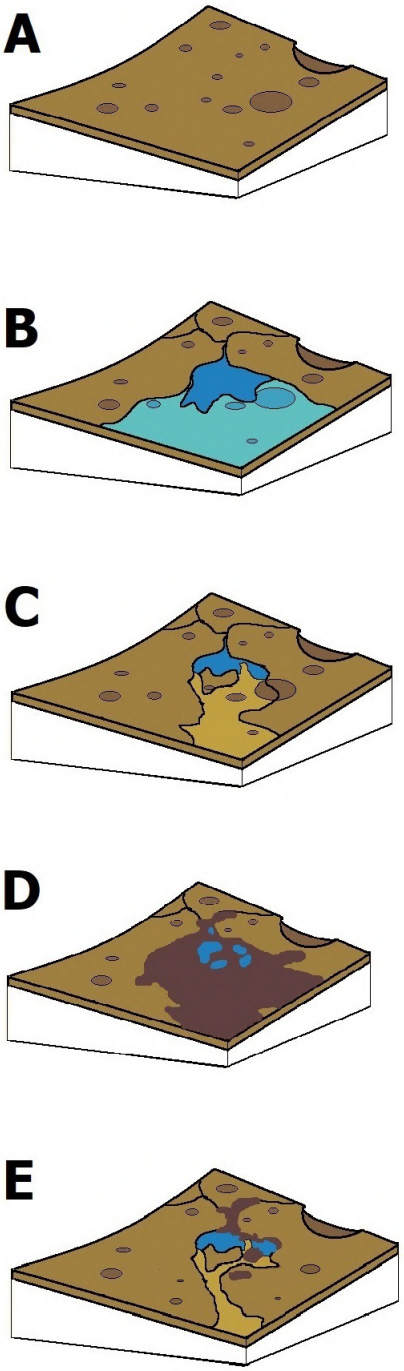

Figure 4.18: The evolution of the Oxia Planum region.

In the Table 4.1 the areas, the craters counted and the modelled age obtained in the different regions are showed.

Unit	Area	Num	Modelled age
Late Noachian	39986.10 km^2	556	3.82 +0.02/-0.03 Ga
Middle Noachian	166062.00 km^2	1993	3.85 +0.02/-0.02 Ga
Amazonian volcanic (Av)	36193 m^2	2123	1.39 +0.56/-0.56 Ga
Exhumed Noachian 1 (Nc1)	81004 m^2	3596	607 +72/-72 Ma
Exhumed Noachian (Nc2)	48433 m^2	1809	659 +120/-120 Ma
Exhumed Noachian (Nc3)	154119 m^2	2628	1.79 +0.30/-0.30 Ga
Cogoon deltaic deposits	502838 m^2	6842	3.78 +0.05/-0.08 Ga

Table 4.1: Units where the craters counting was done, their areas, the number of craters counted and the modelled age obtained from the fit. The Av, Nc1, Nc2, Nc3 units are inside the landing ellipse.

4.1.4 Engineering analysis

The study of the crater areal densities of the craters on Oxia is pivotal not only from a scientific perspective, but also for rover landing and traversing reasons. Indeed, if the rover were to land in a crater with too steep walls, it would remain locked inside with no feasible possibilities to find an exit route, hence resulting in a failure for the mission.
We derived the crater SFD in the ellipses of 1σ, 2σ and 3σ, in the Amazonian unit (Av) and in the three exhumed Noachian units (Nc1, Nc2, Nc3) (see the following Figures). Due to safety reasons, we considered the NC2 unit together with the craters located in the Amazonian patches.
Within the smaller smaller ellipse, where there is the 68% of probability that the rover will land here, we found that the density of craters with diameters $\geq$5 m is 24.55 km^2. On the contrary, within the middle ellipse, where there is the 95% of probability that the rover will land here, we found that the density of craters with diameters $\geq$5 m is 31.62 km^2. Within the larger ellipse, where there is the 99.7% of probability that the rover will land here, we found that the density of craters with diameters $\geq$5 m is 32.36 km^2. Over the four identified units located in the landing ellipse we found that at craters' diameters $\geq$5 m the Amazonian volcanic unit has a density of craters of 58.88 km^2, the exhumed Noachian 1 unit has a density of craters of 43.65 km^2, the exhumed Noachian 2 unit has a density of craters of 35.48 km^2 and the exhumed Noachian 3 unit has a density of craters of 16.98 km^2.

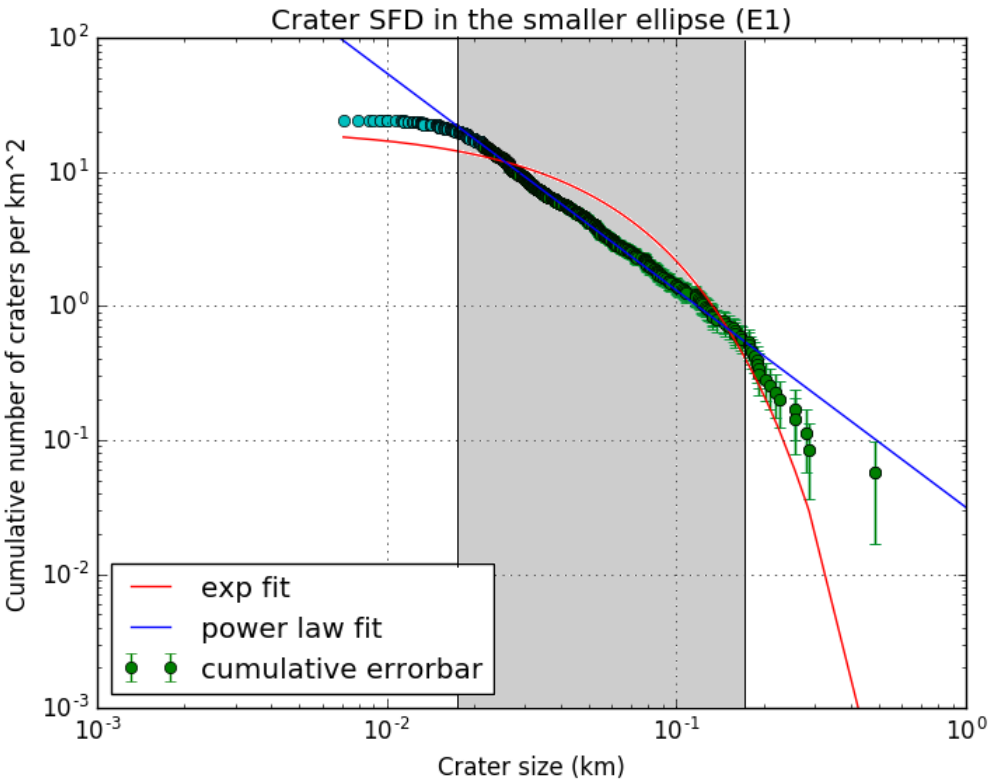

Figure 4.19: SFD of the identified craters. The data were fitted with a power-law fit (grey interval) and with an exponential fit starting at 5 m.

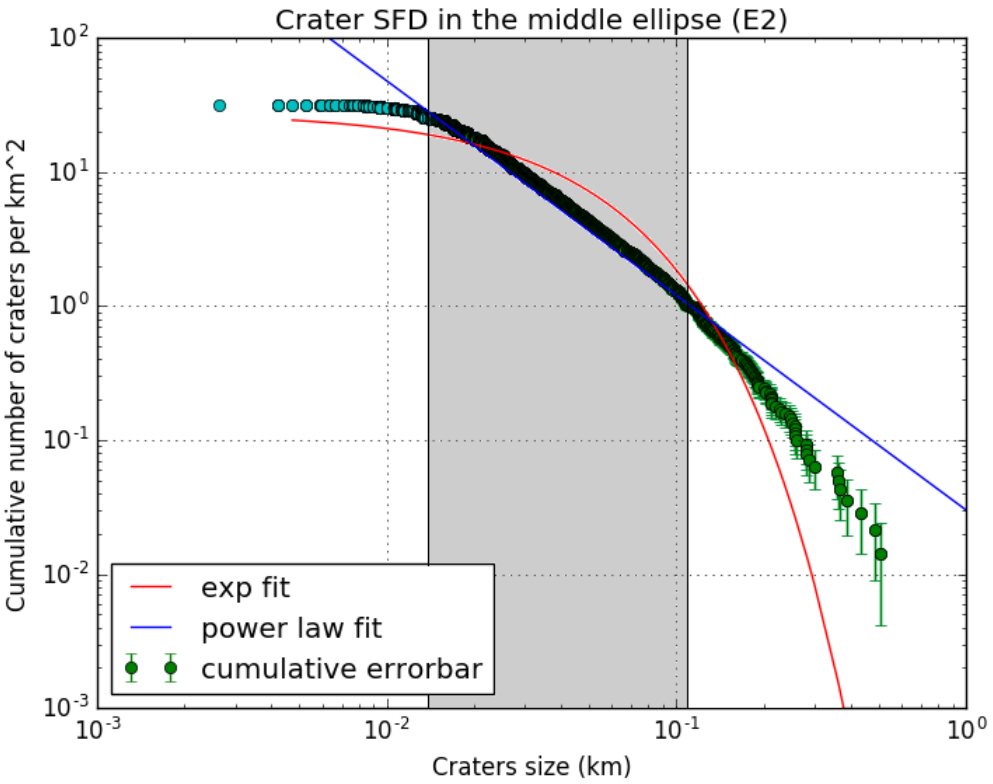

Figure 4.20: SFD of the identified craters. The data were fitted with a power-law fit (grey interval) and with an exponential fit starting at 5 m.

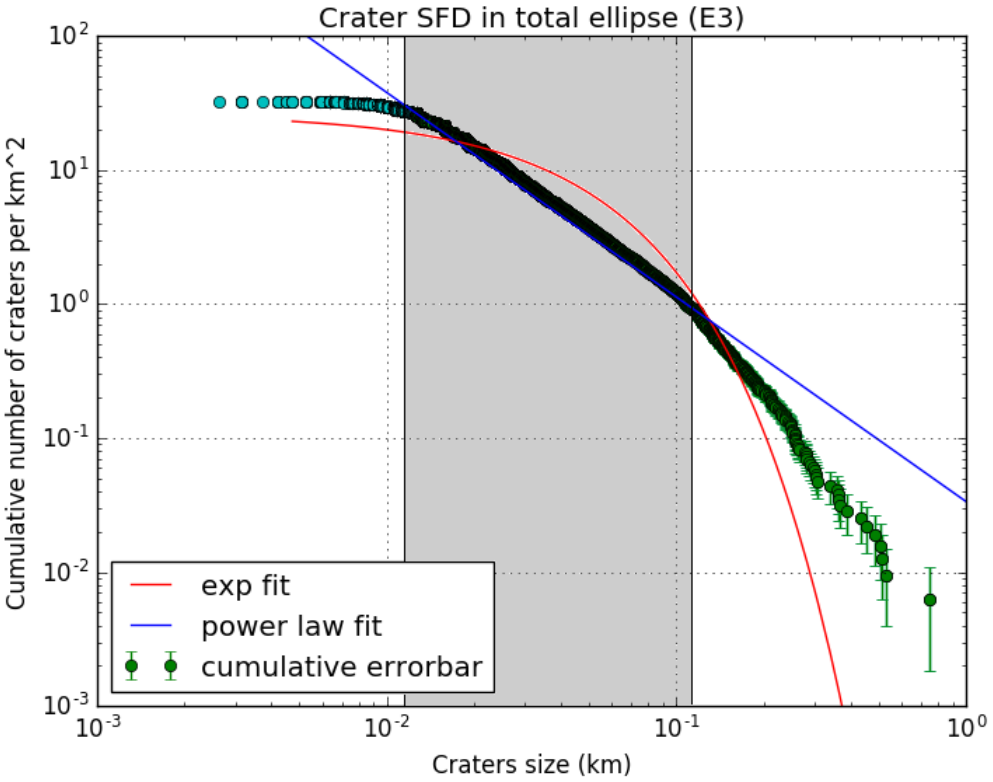

Figure 4.21: SFD of the identified craters. The data were fitted with a power-law fit (grey interval) and with an exponential fit starting at 5 m.

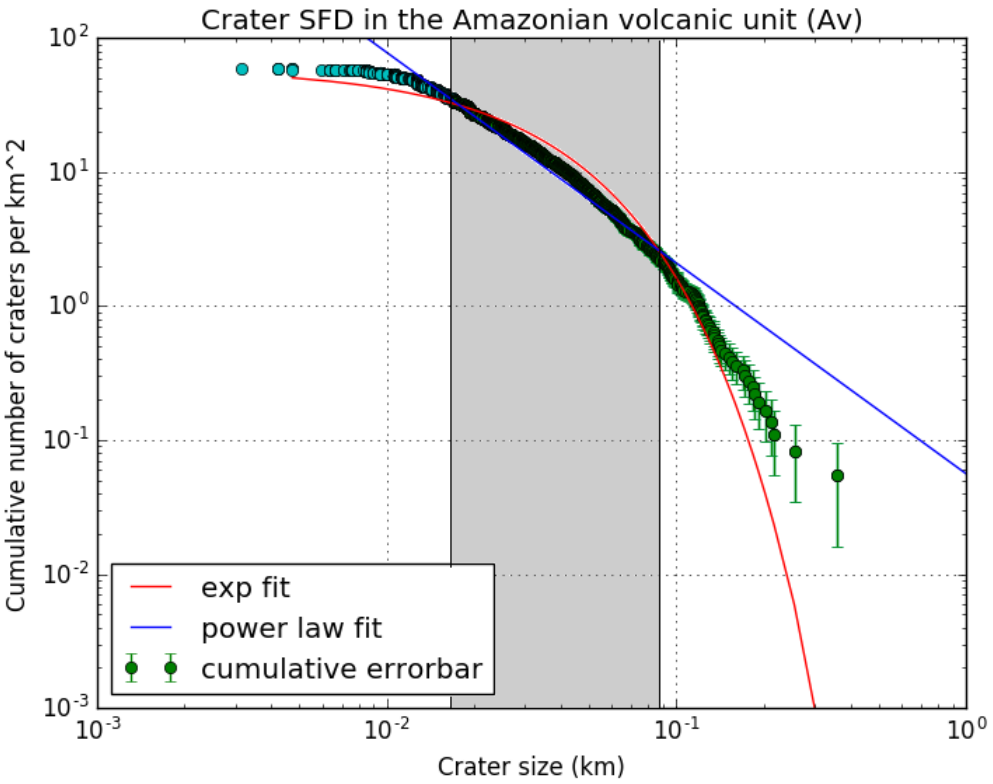

Figure 4.22: SFD of the identified craters. The data were fitted with a power-law fit (grey interval) and with an exponential fit starting at 5 m.

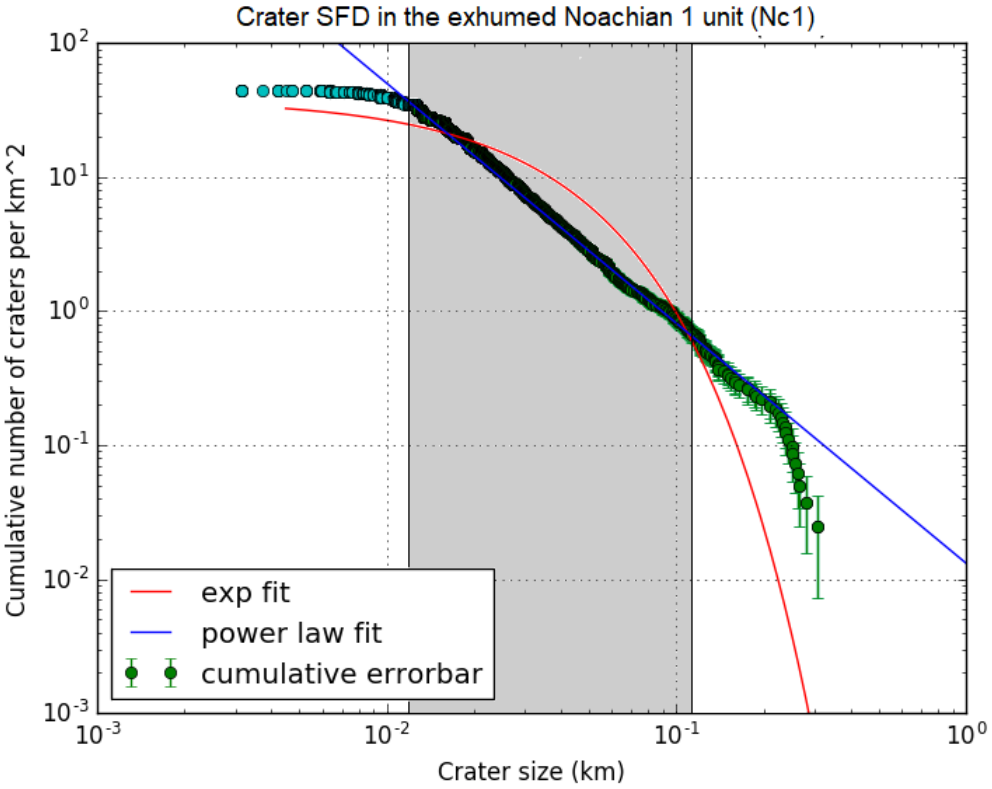

Figure 4.23: SFD of the identified craters. The data were fitted with a power-law fit (grey interval) and with an exponential fit starting at 5 m.

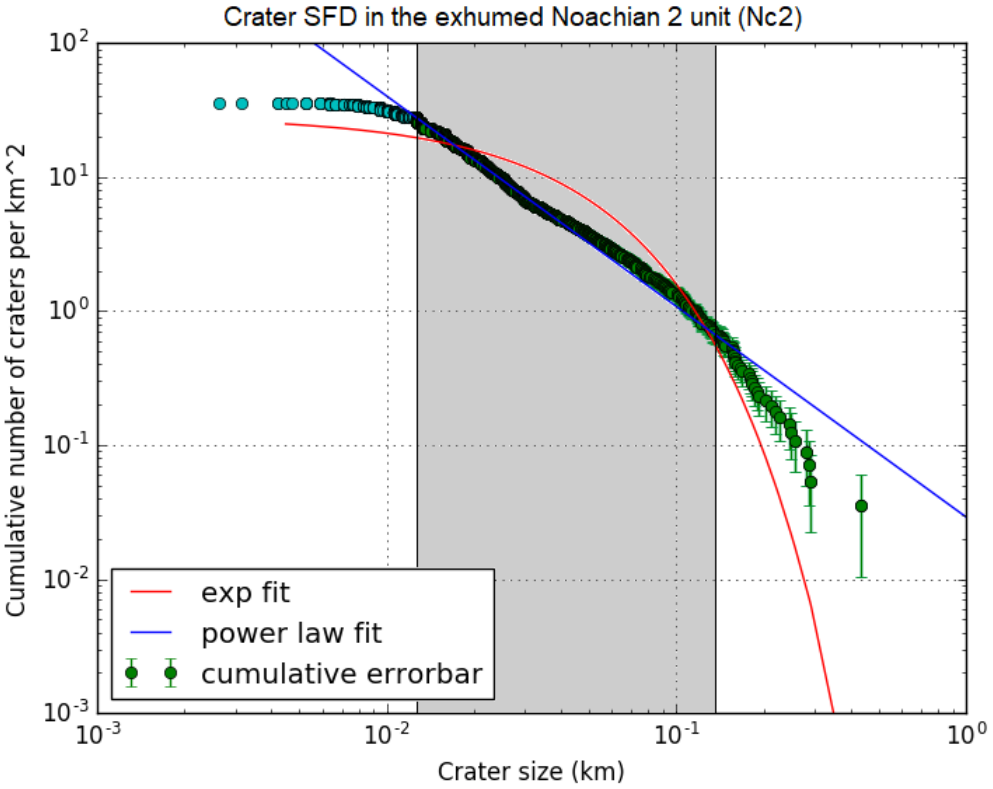

Figure 4.24: SFD of the identified craters. The data were fitted with a power-law fit (grey interval) and with an exponential fit starting at 5 m.

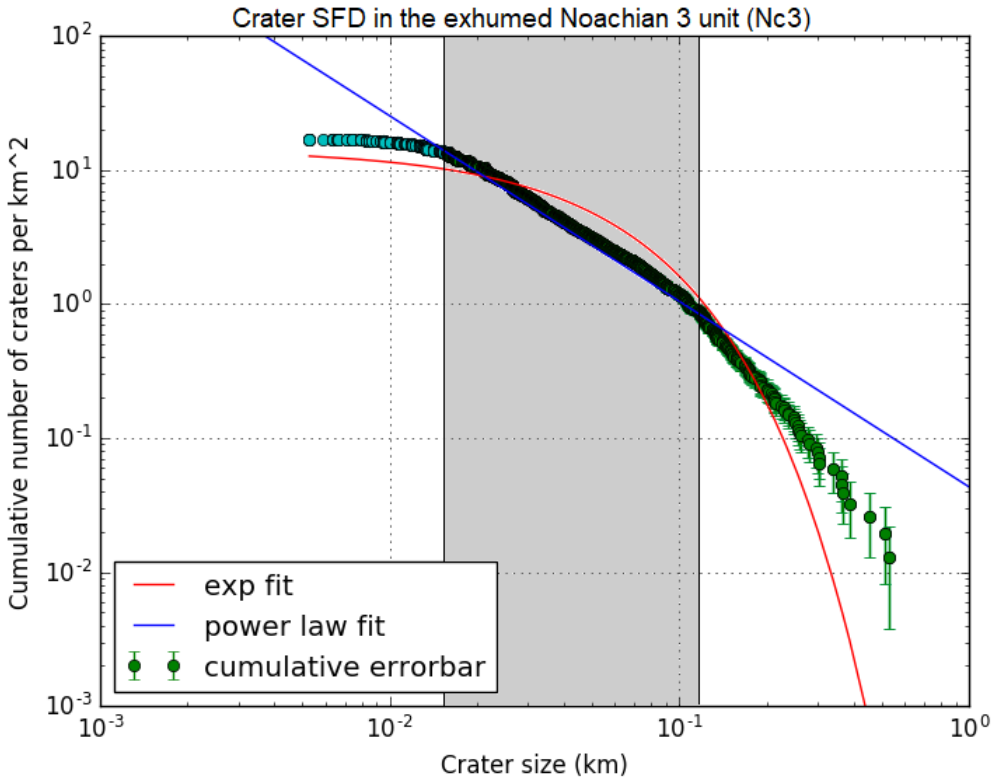

Figure 4.25: SFD of the identified craters. The data were fitted with a power-law fit (grey interval) and with an exponential fit starting at 5 m.

In this work we calculated the cumulative craters SFD per km^2 in the landing sites, considering different regions. The exponential fitting curves used to interpolate the number of craters take in account diameter that are larger than 5 m, because of the resolution of the images. For the power-law cases, we fitted the data down to knee of the distribution following the same approach of Michikami et al. (2008).
In Table 4.2 the slopes derived from the power-law fit and the coefficient derived from the exponential model for the different considered regions are showed. The results suggest that within the selected range the power-law index is more representative of the crater distribution we derived. On the contrary, the exponential curve is not in a good agreement with the data because it overstimates the sizes in the considered range (grey range in all plots) (Table 4.3).
The power-law indices of the exhumed Noachian units are steeper than the Amazonian unit in any case, but not in the last case. As the same way, the

coefficients derived from the exponential fit of the exhumed Noachian units are smaller than the Amazonian one, but not in the last case.
This result is pivotal from engineering aspects, because we can confirm that the Amazonian unit is more dangerous both in the case for landing and roving. Indeed, the density of craters at diameter 5 m is between 1 and 3 times larger than the exhumed Noachian cases (Table 4.3).

	Power-law slope	Exponential coefficient	Density at 5 m (km^2)
E1	-1.62 +0.03/-0.04	-22.92 +1.19/-1.57	24.35
E2	-1.60 +0.03/-0.04	-27.01 +0.8/-1.04	31.94
E3	-1.53 +0.02/-0.02	-27.24 +0.57/-0.74	32.71
Av	-1.57 +0.04/0.04	-36.08 +1.29/-1.82	58.55
Nc1	-1.79 +0.04/-0.05	-36.77 +1.18/-1.61	44.24
Nc2	-1.57 +0.05/-0.06	-28.80 +1.12/-1.62	35.83
Nc3	-1.38 +0.03/-0.04	-21.77 +0.75/-1.04	17.05

Table 4.2: The slope derived from the power-law fit and the coefficient derived from the exponential model for the different considered regions.

Av/Nc1	Av/Nc2	Av/Nc3
1.32	1.63	3.43

Table 4.3: The ratios between the Amazonian density at 5 m and the other exhumed Noachian units.

4.2 Boulder analysis

4.2.1 Scientific analysis

The identification and boulder counts are important to assess the processes that occurred and modified the Oxia Planum surface. The calculation of their size-frequency distribution, their spatial density and the corresponding fitting curves were done as in other works (Golombek et al., 2003, 2008). From these studies it is possible to distinguish the formation and degradation processes of the boulders, such as impacts, collapse or wind erosion.
To obtain a homogeneous dataset, we decided to consider as statistical meaningful boulders with a diameter larger than 1.75 m. Indeed, below this value

the SFD starts to roll over, meaning that the sampling are not statistically complete and significant, as suggested with the same dataset by Pajola et al. (2017). We considered an inferior limit to the dimension of the boulders, because below this value the power-law model overstimates the size, indeed the regression lines are above the data (Golombek et al., 2008; Hebrard et al., 2012). The cumulative distribution becomes flat at size smaller than about 1.5 m due to the resolution of the images (Heet et al., 2009; Hebrard et al., 2012).

We counted boulders located inside five circles in the 1σ ellipse (Figure 4.26). We located the circles in regions with a great number of boulders, in order to have a superior limit for the boulder densities.

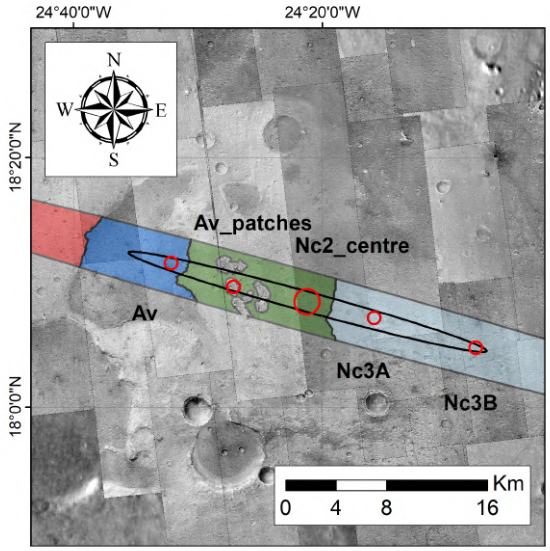

Figure 4.26: The five circles where the counting of boulders was done. These are HiRISE images.

The first circular study area (500 m radius) is localized in the Amazonian volcanic unit (Av). This area is 785000 m^2 and we counted a total number of 22611 boulders (Figure 4.27). The minimum diameter in this count is 0.13 m and the maximum one is 5.95 m.
Through an unbinned cumulative size frequency distribution we obtained the best power-law fit with an index of -4.03 +0.16/-0.21 (Figure 4.29). The density we derived for boulders $\geq$1.75 m is 1.06 x 10^{-3} per m^2.

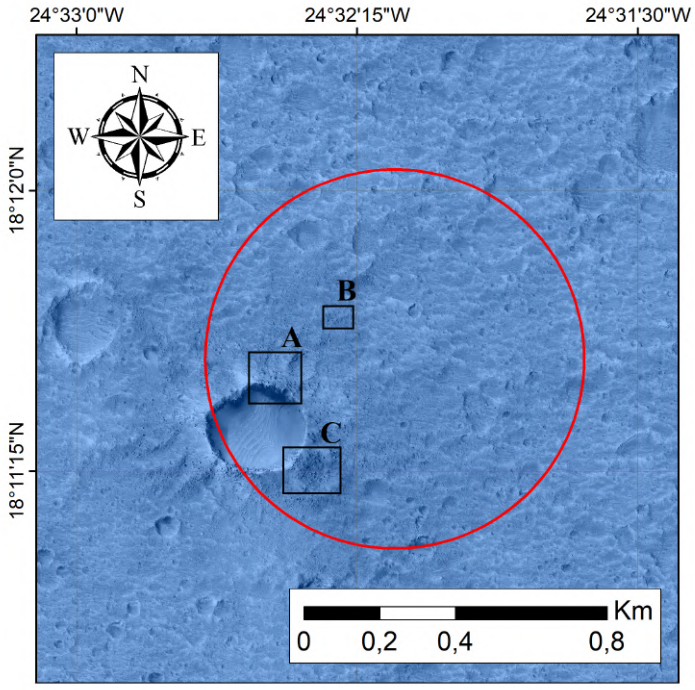

Figure 4.27: Circle (Av) where we counted the boulders localised in the Amazonian unit. In Figure 4.28 the three regions in the black rectangles are showed.

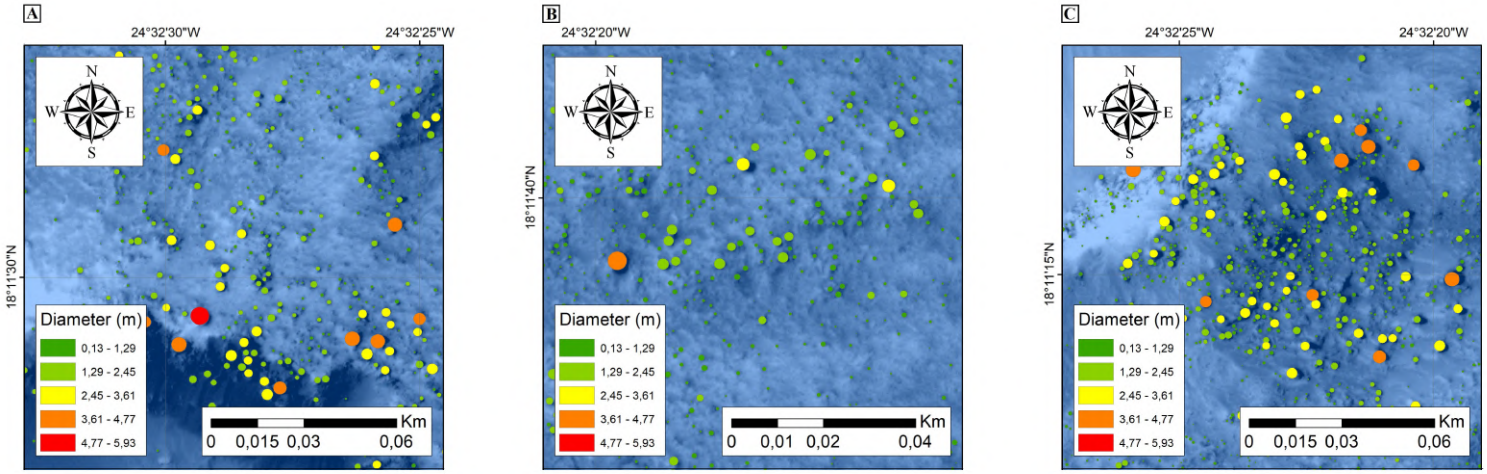

Figure 4.28: The three regions identified in Figure 4.27.

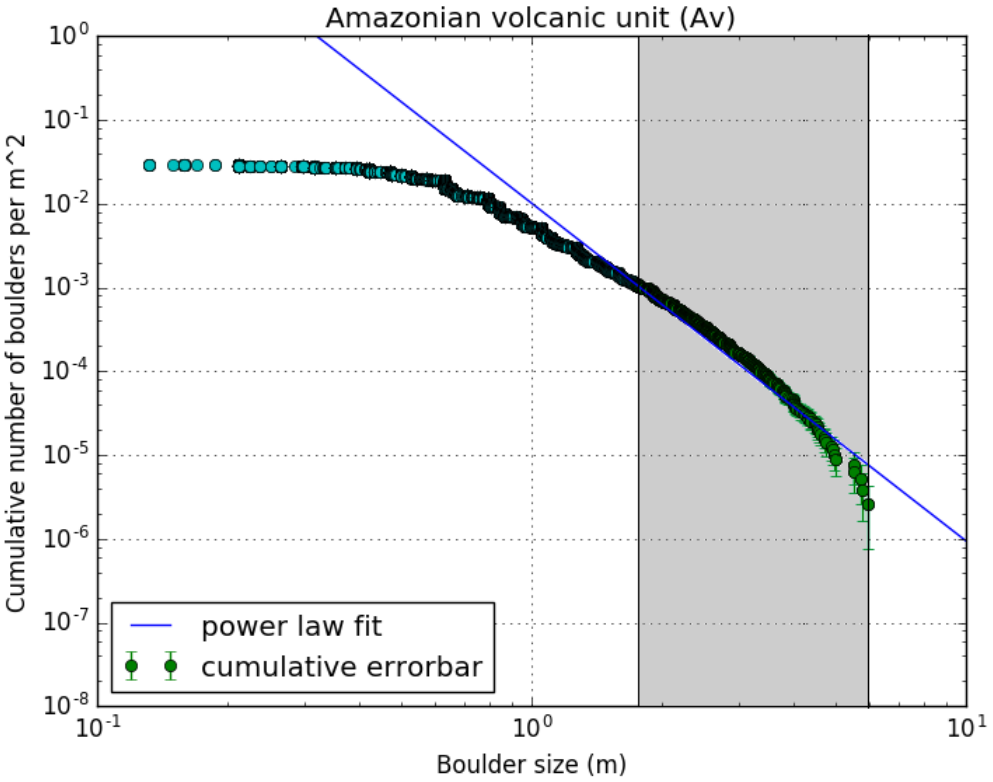

Figure 4.29: SFD of the identified boulders in the Av unit. The data were fitted with a power-law fit performed in the grey interval starting at 1.75 m.

The second circular study area (500 m radius) is localized in the Amazonian patches (Av_patches) situated in the middle of the NC2 unit. This area is 785000 m^2 and we counted a total number of 4665 boulders (Figure 4.30). The minimum diameter in this count is 0.15 m and the maximum one is 4.75 m. In this case this circle is located in one of the Amazonian patches.
Through an unbinned cumulative size frequency distribution we obtained the best power-law fit with an index of -4.74 +0.51/-1.30 (Figure 4.32). The density we derived for boulders $\geq$1.75 m is 1.63 x 10^{-4} per m^2.

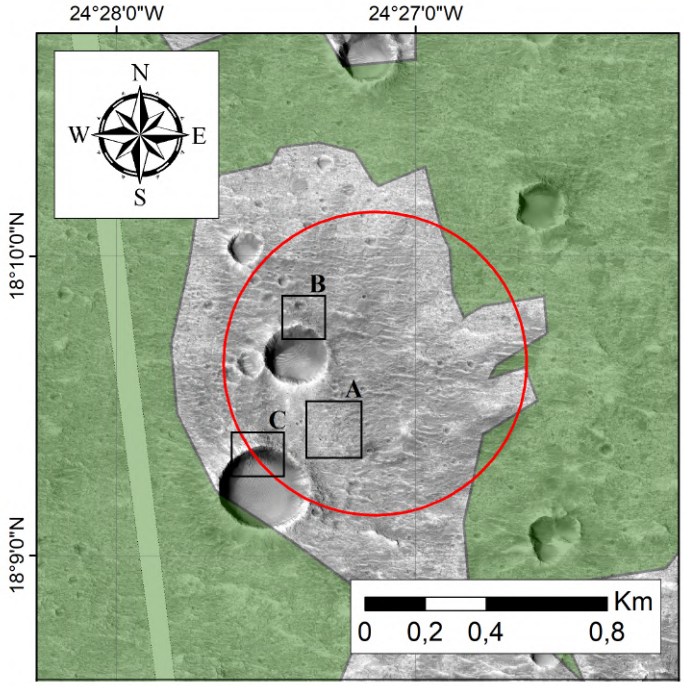

Figure 4.30: Circle (Av_patches) where we counted the boulders localised in the exhumed Noachian 2 unit. In Figure 4.31 the three regions in the black rectangles are showed.

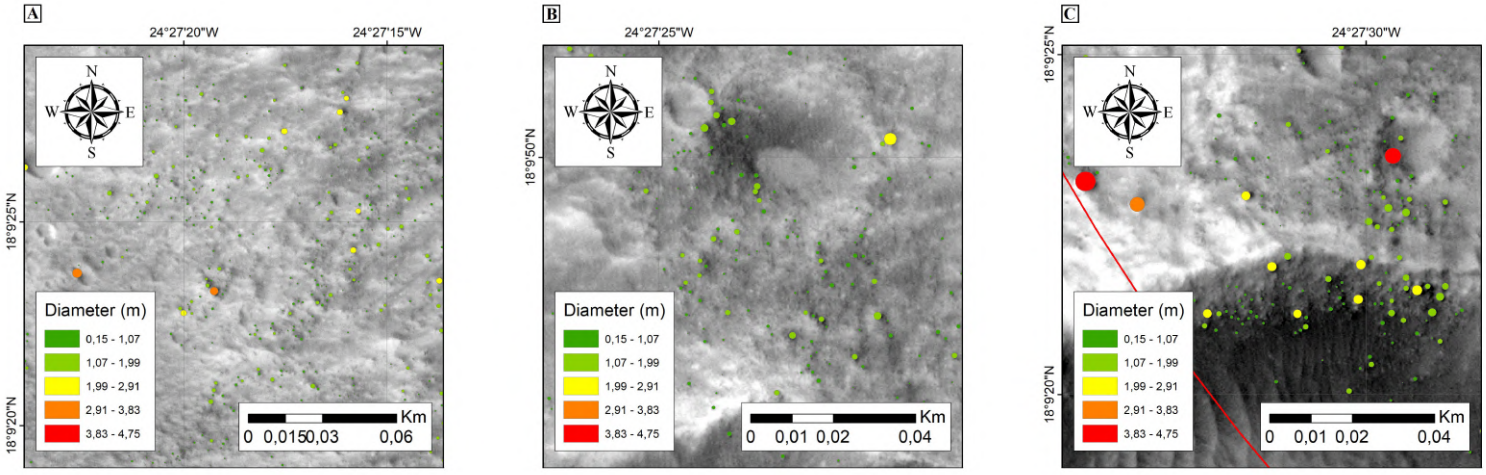

Figure 4.31: The three regions identified in Figure 4.30.

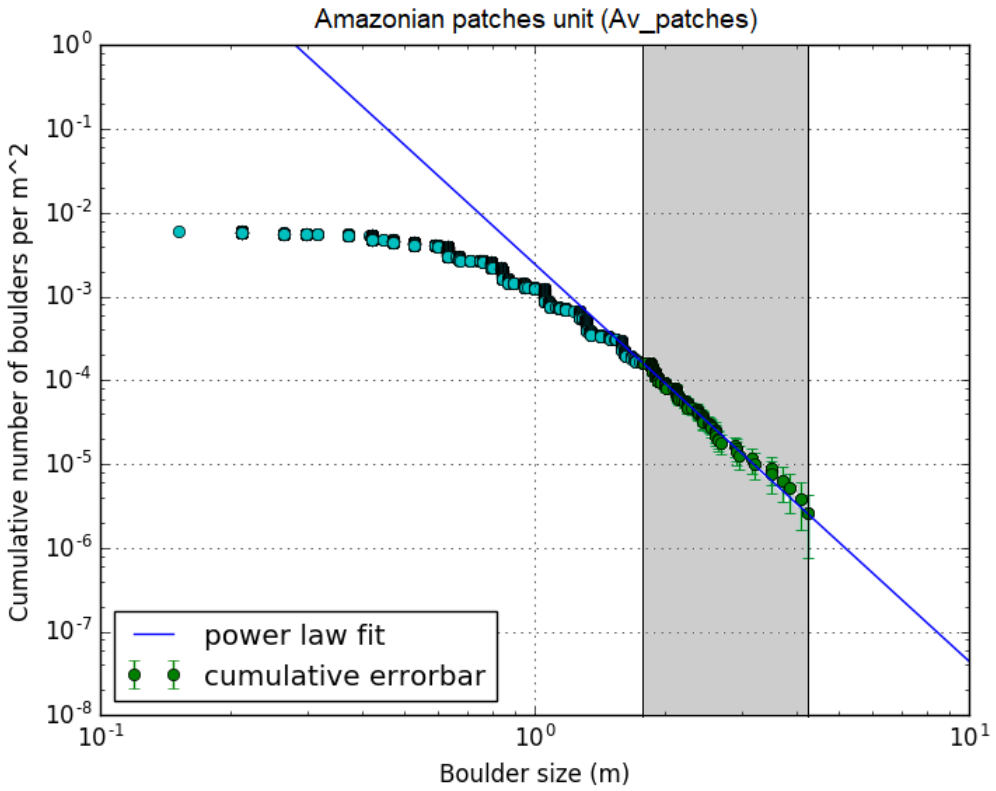

Figure 4.32: SFD of the identified boulders in the Av_patches unit. The data were fitted with a power-law fit performed in the grey interval starting at 1.75 m.

The third circular study area (1 km radius) is localized in the exhumed Noachian unit (Nc2_centre), exactly at the centre of the ExoMars landing ellipse. Here we decided to study an area that is larger than the others because there is a higher probability that the rover will land at the centre of the ellipse. This area is 3140000 m^2 and we counted a total number of 1077 boulders (Figure 4.33). The minimum diameter in this count is 0.317 m and the maximum one is 3.404 m.
Through an unbinned cumulative size frequency distribution we obtained the best power-law fit with an index of -5.57 +0.57/-1.11 (Figure 4.35). The density we derived for boulders $\geq$1.75 m is 2.20 x 10^{-5} per m^2.

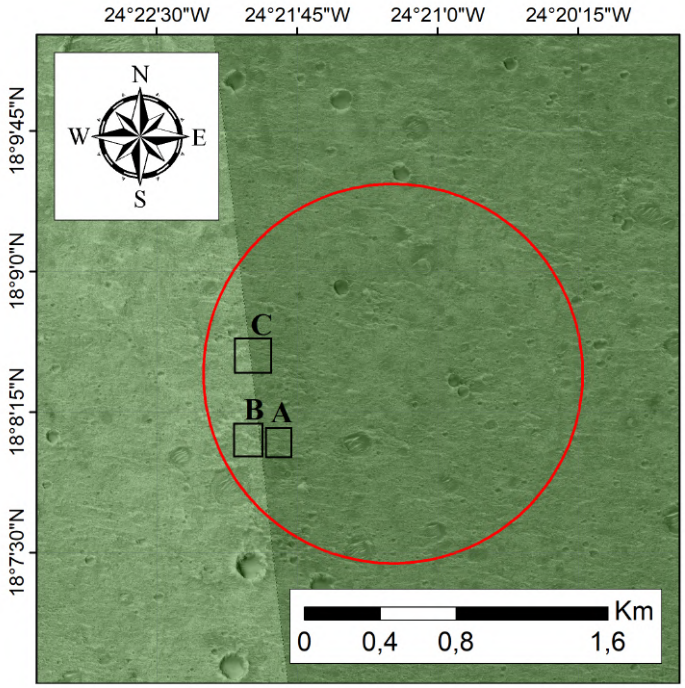

Figure 4.33: Circle (Nc2_centre) where we counted the boulders localised in the exhumed Noachian 2 unit at the centre of the landing ellipse. In Figure 4.34 the three regions in the black rectangles are showed.

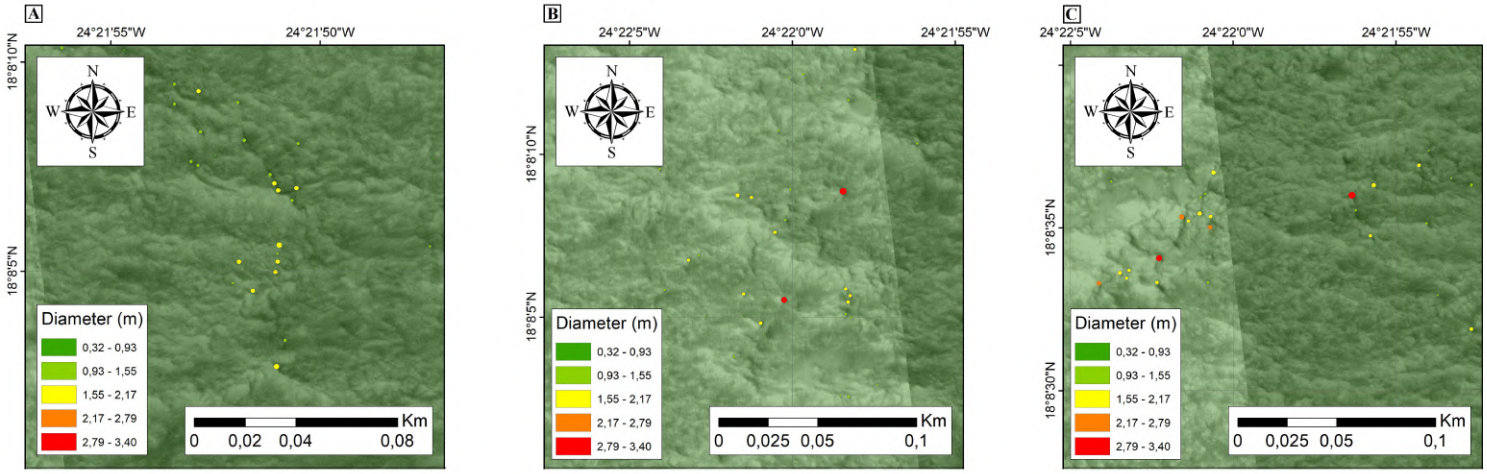

Figure 4.34: The three regions identified in Figure 4.33.

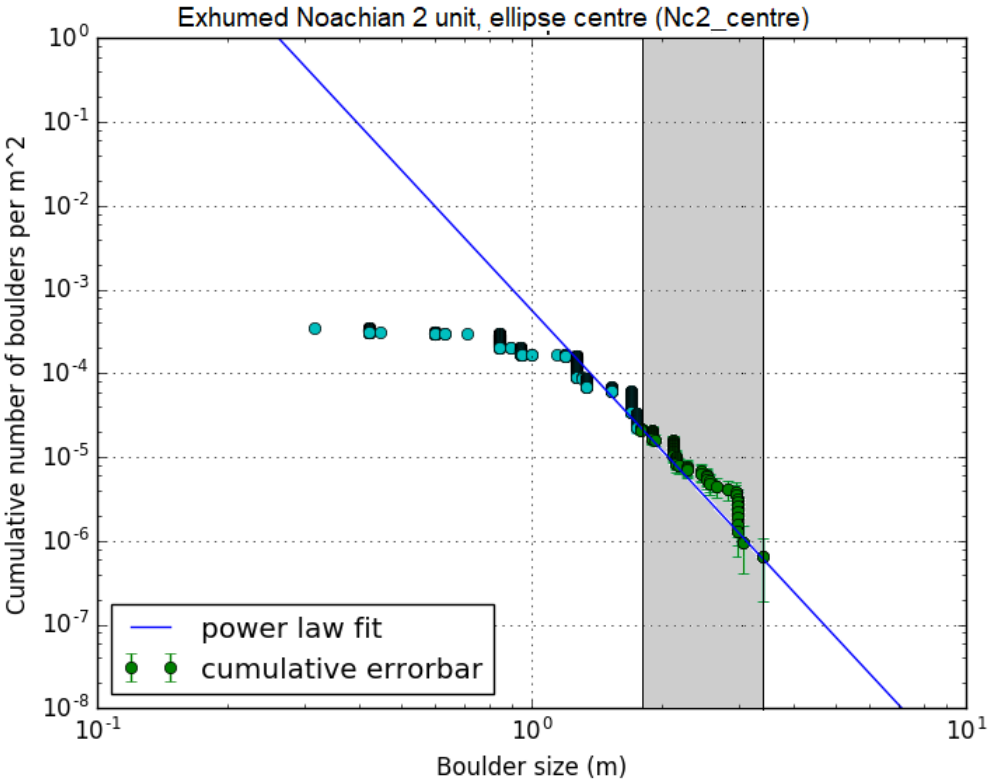

Figure 4.35: SFD of the identified boulders in the Nc2 unit. The data were fitted with a power-law fit performed in the grey interval starting at 1.75 m.

The fourth circular study area (500 m radius) is localized in the exhumed Noachian 3 unit (Nc3A). This area is 785000 m^2 and we counted a total number of 452 boulders (Figure 4.36). The minimum diameter in this count is 0.42 m and the maximum one is 4.26 m.
Through an unbinned cumulative size frequency distribution we obtained the best power-law fit with an index of -5.36 +0.64/-1.66 (Figure 4.38). The density we derived for boulders $\geq$1.75 m is 8.92 x 10^{-5} per m^2.

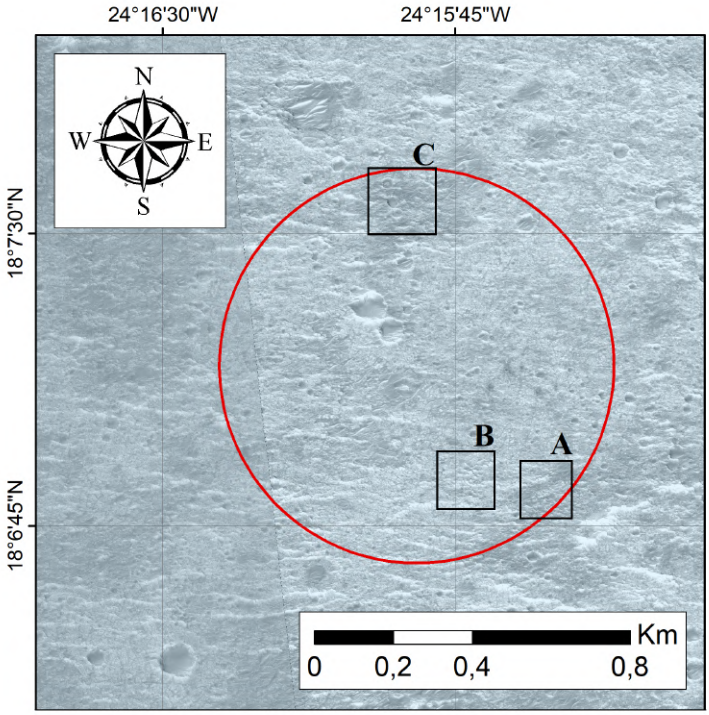

Figure 4.36: Circle (Nc3A) where we counted the boulders localised in the exhumed Noachian 3 unit. In Figure 4.37 the three regions in the black rectangles are showed.

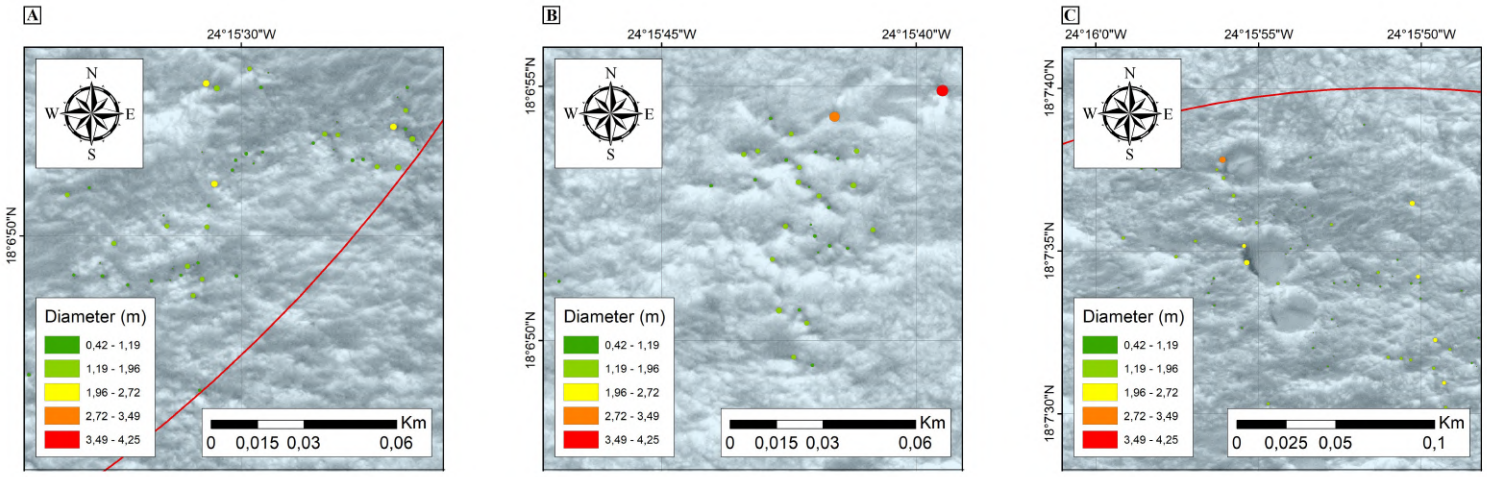

Figure 4.37: The three regions identified in Figure 4.36.

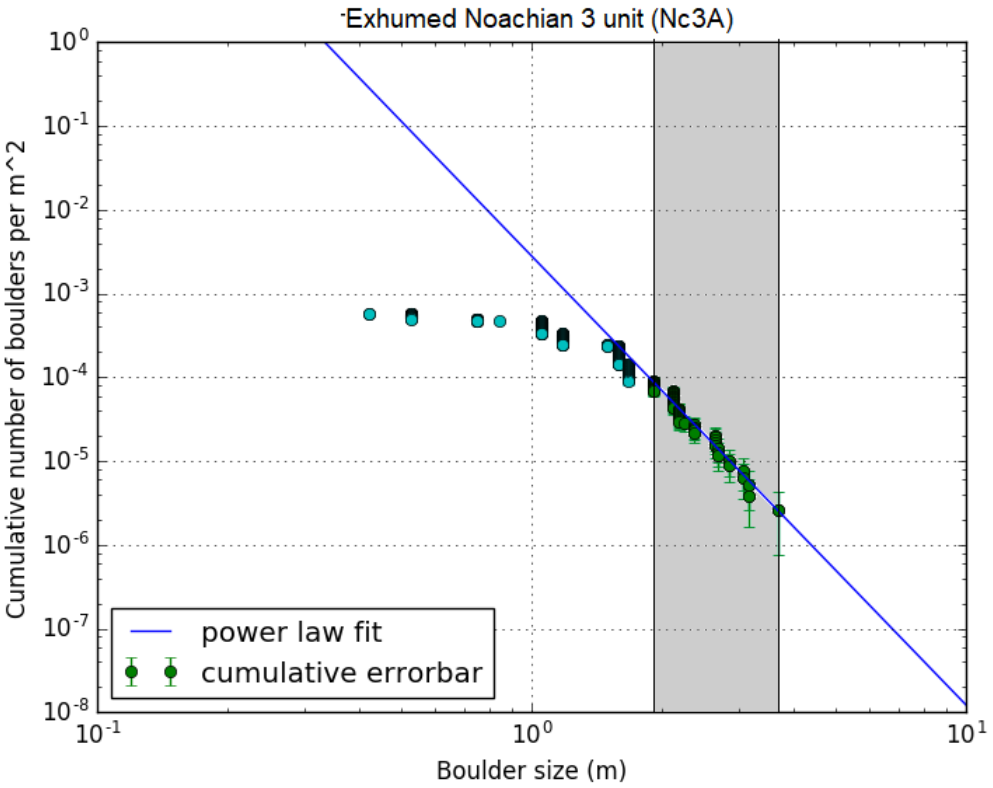

Figure 4.38: SFD of the identified boulders in the Nc3 unit (Nc3A circle). The data were fitted with a power-law fit performed in the grey interval starting at 1.75 m.

The fifth circular study area (500 m radius) is localized in the exhumed Noachian unit (Nc3B). This area is 785000 m^2 and we counted a total number of 735 boulders (Figure 4.39). The minimum diameter in this count is 0.55 m and the maximum one is 8.43 m.
Through an unbinned cumulative size frequency distribution we obtained the best power-law fit with an index of -5.20 +0.49/-1.19 (Figure 4.41). The density we derived for boulders $\geq$1.75 m is 4.32 10^{-4} per m^2.

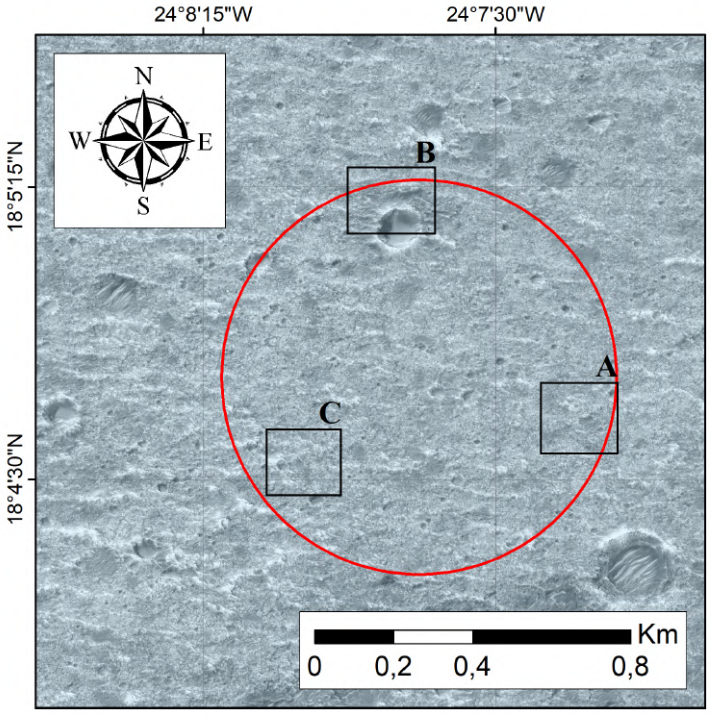

Figure 4.39: Circle (Nc3B) where we counted the boulders localised in the exhumed Noachian 3 unit. In Figure 4.40 the three regions in the black rectangles are showed.

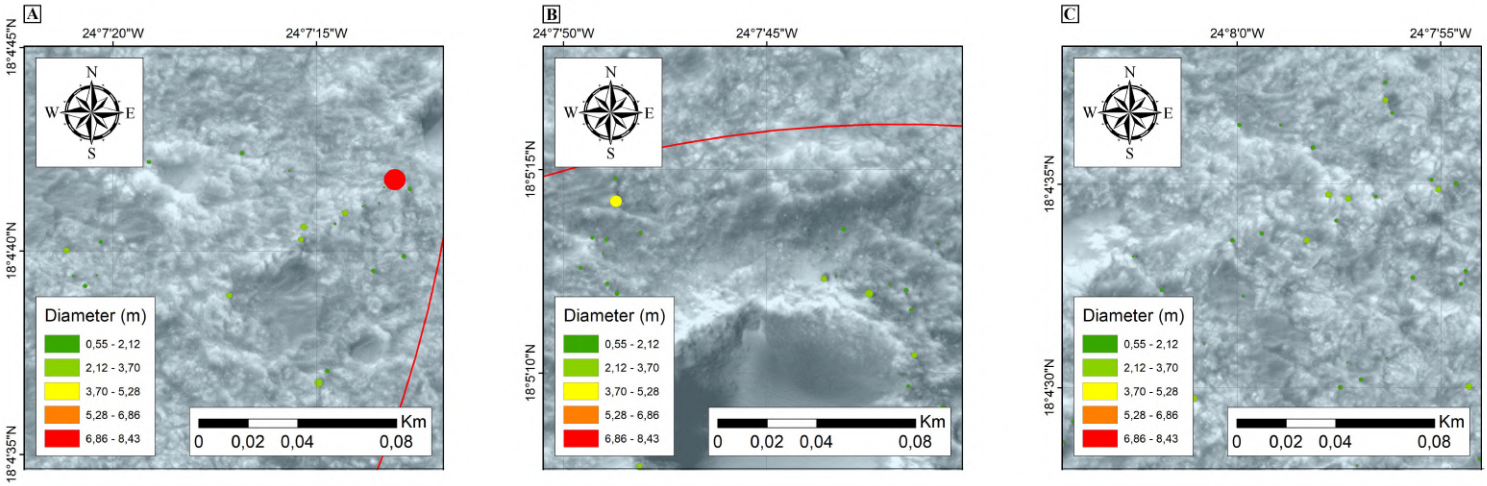

Figure 4.40: The three regions identified in Figure 4.39.

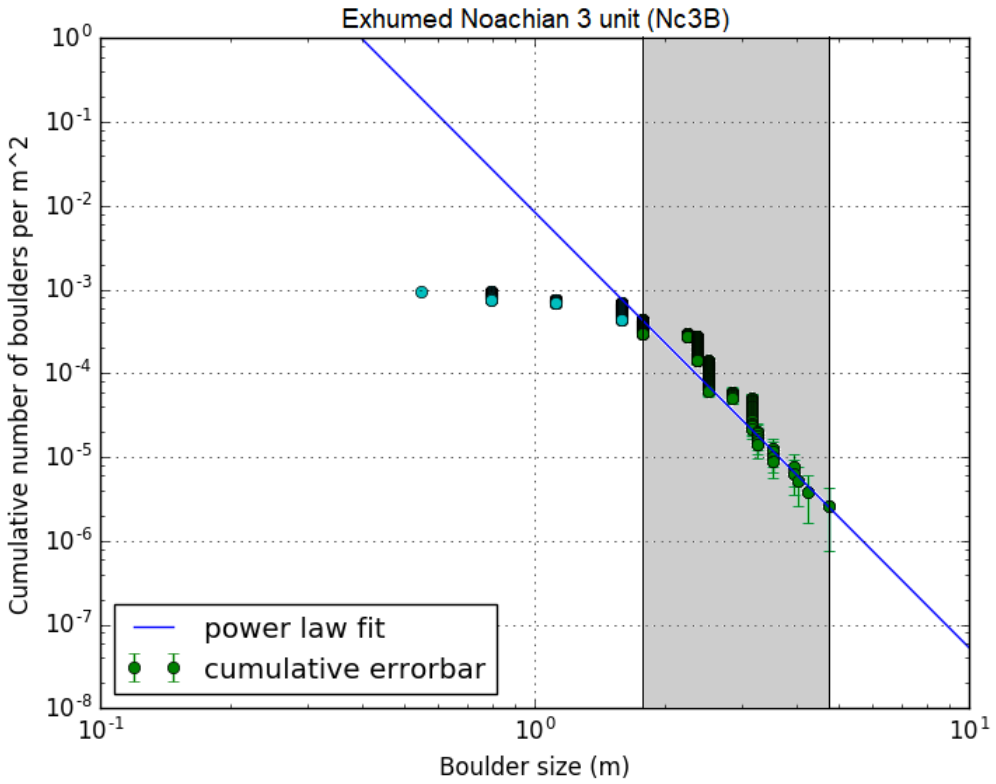

Figure 4.41: SFD of the identified boulders in the Nc3 unit (Nc3A circle). The data were fitted with a power-law fit performed in the grey interval starting at 1.75 m.

In this work we calculated the cumulative boulder SFD per m^2 in different regions in the landing 1σ ellipse. The power-law fitting curves used to interpolate the number of boulders take in account diameters that are larger than 1.75 m. The power-law indices derived from the total amount of boulders with size larger than 1.75 m are showed in Table 4.4, where the areas, the boulders counted and the densities at 1.75 m for the different regions are indicated too.
We identified five regions in the Oxia Planum region to investigate how the SFD and boulder densities are different among them and to compare such results with the Pajola et al. (2017) work, where boulders identified on the previous landing ellipse center have been studied. These five circles are located in the Amazonian and in the exhumed Noachian units. The SFDs obtained can be attributed to impact processes, since the indices reflect the distributions produced by impact of a rock surface on the ground (Surveyor Scientific

Evaluation and Analysis Team, 1966; Shoemaker, 1965; Melosh,1984). They are comparable with the indices produced for the Moon and for the asteroids. Nevertheless, Mars was subjected not only to impacts, like the Moon and asteroids, but also to processes such as aeolian and water activity, chemical and physical erosion and tectonic events (Bourke et al., 2005; Viles et al., 2005). These phenomena could have modified the original boulder size distribution, making it to increase or decrease as suggested in Pajola et al. (2017).
The power-law indices we derived in the exhumed Noachian units are always steeper than those from the Amazonian unit and from the Amazonian patches over NC2. This can be due to different processes occurred on the Martian surface. When an impact occurs, shock waves are generated if the energy produces is high enough to overcome the limit between elastic and inelastic behavior of the rocks (Jaeger et al., 2007). The Amazonian unit is composed by basaltic lava flows, while the Noachian unit is made by clay, of sedimentary origin. Shock waves propagate at higher velocity in basalts than in sedimentary rocks (Ahrens and Johnson, 1995). These two different materials have also different mechanical properties (Chevrier and Mathé, 2007; Hausrath et al., 2008; Yesavage et al., 2015) that can influence boulders production and preservation. One of this property is that igneous rocks have higher dynamic strength than the sedimentary ones (Ai and Ahrens, 2004) and this infuences melt generation at impact (Osinski et al., 2011). Smaller shoks waved velocities and dynamic strengths for the sedimentary rocks produce smaller and abundant boulders, while the igneous ones produce fewer and larger boulders. Our SFD results are in agreement with this observations. Indeed in Table 4.4 we show the densities per m^2 at diameter 1.75 m. These values are decreasing with respect to the distance from Av. That means that the Av unit is much richer of boulders with respect to the Nc units, as previous specified.

The values of the densities and the slopes of the power-law model we derived (Table 4.4) in this work are comparable with the ones obtained in Pajola et al. (2017). The density in our Av unit of 1.06 x 10^{-3} m^2 is comparable to their Av unit density of 1.79 x 10^{-3} m^2. On the contrary, our 1.63 x 10^{-4} m^2 is lower with respect to the Av values in Pajola et al. (2017). The power-law index we obtained in the Av unit of -4.03 +0.16/-0.21 is slightly different with their value of -4.8 +0.2/-0.2 in the Av unit, while it is comparable with our slope of -4.74 +0.51/-1.30 in the Av_patches. In the exhumed Noachian cases, our density values of about 10^{-5} m^2 are much less with respect to the Pajola et al. (2017) value of 2.55 x 10^{-4} m^2, suggesting that our Noachian studied areas have been degraded more than the Noachian unit of Pajola et al. (2017). Nevertheless, the identified power-law indices are similar to

the -5.5 +0.3/-0.4 value previously identified. This means that the boulder densities per m^2 are typically much less than the previous measurements, but the erosive processes, such as wind, have acted in the similar fashion, hence returning a similar SFD.

Circle	Area (m^2)	Num	Slope	Density ≥1.75 m
Av	785000	22611	-4.03 +0.16/-0.21	1.06 x 10^{-3} m^2
Av_patches	785000	4665	-4.74 +0.51/-1.30	1.63 x 10^{-4} m^2
Nc2_centre	3140000	1077	-5.57 +0.57/-1.11	2.20 x 10^{-5} m^2
Nc3A	785000	452	-5.36 +0.64/-1.66	8.92 x 10^{-5} m^2
Nc3B	785000	735	-5.20 +0.49/-1.19	4.32 x 10^{-4} m^2

Table 4.4: Circles, inside the landing site, where the boulders counting was done, their areas in m^2, the number of boulders counted and the slope we obtained from the power-law fit. The Nc2_centre unit is situated in the centre of the landing ellipse.

4.2.2 Engineering analysis

As for the craters, the bounders analysis is also important because of safety reasons, since boulders can be dangerous during the rover landing and traversing. The Amazonian unit has densities larger than the exhumed Noachian unit at the size of 1.75 m, as showed in the ratios between the Av unit and the other units (Av_patches, Nc3A, Nc3B) in Table 4.5. Indeed, the density value obtained in the Av unit is 1.06 x 10^{-3} m^2, while the ones derived in the other cases are 1.63 x 10^{-4} m^2 in the Av_patches, 2.20 x 10^{-5} m^2 in Nc2_centre, 8.92 x 10^{-5} m^2 in Nc3A and 4.32 x 10^{-4} m^2 in Nc3B (Table 4.4). This result is pivotal from engineering requirements because we quantitatively show that the Amazonian region needs to be avoided while landing. Indeed, the exhumed Noachian units are safer regions than the Amazonian one, since the density of boulders per m^2 is lower than the Av unit and the Av_patches unit.

Av/Av_patches	Av/Nc2_centre	Av/Nc3A	Av/Nc3B
6.50	48.18	11.88	2.45

Table 4.5: The ratios between the Amazonian density at 1.75 m and the other exhumed Noachian units.

Through our counts we can make a comparison of the boulder distribution in Oxia Planum with those present in other landing site on Mars.
The work of Golombek and Rapp (1997) shows that the Chryse and the Utopia Planitia, the landing sites of the Viking 1 and 2 missions, have a spatial densities of 3.9 x 10^{-9} m^2 and 3.4 x 10^{-6} m^2 for boulders $\geq$1.75 m. On the contrary, the work of Golombek et al. (2008) shows a much higher spatial density of 1.0 x 10^{-4} m^2 for boulders $\geq$1.75 m on the landing site of the Mars Pathfinder. The work of Golombek et al. (2012) shows a spatial density of 1.0 x 10^{-6} m^2 for boulders $\geq$1.75 m on the Vastitatis Borealis, the landing site of the Phoenix lander.
The Mars Pathfinder landing area is located on a much rockier surface than the landing sites of the Viking 1 and 2 and of the Phoenix lander. In Table 4.6 we can see that the Pathfinder landing site is 4.54 times dangerous than our Nc2_centre area and 1.12 times dangerous than our Nc3A area, but it is less dangerous than our other units. Indeed, our Av unit is 10.60 more times dangerous than the Pathfinder landing site, our Av_patches unit is 1.63 times more dangerous than the Pathfinder landing site and our Nc3B unit is 4.32 times more dangerous than the Pathfinder landing site.
The right landing area for the ExoMars rover would therefore be the exhumed Noachian 2 unit (Nc2), but since they have similar elevation and thermal inertia also the exhumed Noachian 1 unit (Nc1) can be considered an optimal landing site.

Av/P	Av_patches/P	P/Nc2_centre	P/Nc3A	Nc3B/P
10.60	1.63	4.54	1.12	4.32

Table 4.6: The ratios between the Pathfinder landing site density at 1.75 m and our ones.

Chapter 5

Conclusions

The Oxia Planum region, situated in the Oxia Palus quadrangle, has been chosen as the landing site for the future ESA ExoMars 2020 rover, because it is both an engineering-safe area, as well as it is interesting and important from an exobiological standpoint.
The main focus of this thesis has been the identification and measurement of craters and boulders located in the Oxia Planum area. We first performed a statistical analysis of the craters and a dating of the areas located on Oxia. We used THEMIS images, whose spatial scale is 100 m/pixel, on the two surface units present on Oxia Planum. They are a middle and a late Noachian highland units, that were individuated by the use of the global geologic map by Tanaka et al. (2014). The method of counting craters was used to derive the age of these units and we found a modelled age of 3.85 +0.02/-0.02 Ga for the middle Noachian unit and a modelled age of 3.82 +0.02/-0.03 Ga for the late Noachian unit. We then derived the age of the four different deposits that are present inside the landing ellipse, by means of high resolution CTX images (5.0 m). They are an Amazonian volcanic unit and three exhumed Noachian units. The modelled age we derived are 1.39 +0.56/-0.56 Ga for the Amazonian unit, 607 +72/-72 Ma for the exhumed Noachian 1 unit, 659 +120/-120 Ma for the exhumed Noachian 2 unit and 1.79 +0.30/-0.30 Ga for the exhumed Noachian 3 unit. The studied units are all Noachian areas that were exhumed during the Amazonian age. Two of the exhumed Noachian units have the same mean values in elevation and thermal inertia; they also have the same exposure age, on the contrary, the exhumed Noachian 3 unit is higher in elevation and older in age than the other ones, therefore it was exposed earlier in time with respect to the other two.
Thanks to the modelled ages derived from the different units located in the Oxia Planum region, we suggested an evolutionary model of the area. By analysing the middle and late Noachian units we derived an age of valleys

incision and water activity, together with the formation of the Cogoon deltaic deposits. Afterwards, during the Hesperian-Amazonian epoch volcanic lava flows entirely covered the region and partially covered the Cogoon deltaic deposits. Later, the erosion occurred and the underneath, clay-rich deposits started to be exhumed.
These results were pivotal from a scientific perspective, because they support the previous interpretation that Oxia Planum is located in Noachian terrains, achieving the surface exposure goal required by the ExoMars mission. Indeed, the Oxia Planum region is a clay-rich unit, indicating past aqueous activities, that are fundamental for astrobiological perspectives: they indicate a possible rich environment, where ancient biosignatures might still be present, and a good preservation of the environment. This demonstrates that the Oxia Planum region is a remarkable site for searching potential life on Mars and the right landing site for the ExoMars 2020 mission. In addition to the differents units located in the Oxia Planum region, we made the first crater count in the Cogoon deltaic deposits, performed through CTX 5.0 m resolution images. The modelled age we obtained is 3.78 +0.05/-0.08 Ga and it indicates the latest stage of water pulses occurring in the area. This age is comparable with the one suggested in Quantin et al., (2016) of >3.5 Ga.
Regarding the boulders manual identification and count, we used the MRO-HiRISE (with a spatial scale of 0.25 m/pixel and 0.5 m/pixel) images and we calculated their size-frequency distribution and their spatial density. This work has been accomplished in different zones of the landing ellipse to assess the processes that occurred and modified the Oxia Planum surface. The SFDs obtained can be attributed to impact processes. By analysing the slope, derived from the power-law fitting curves, we noticed that the slopes in the exhumed Noachian cases are always steeper than those obtained in the Amazonian case. This can be due to different processes that occurred on the Martian surface and to the composition of the terrains, because different materials have different mechanical properties and they can influence the production and preservation of boulders. We found that the Amazonian unit is richer of boulders than the exhumed Noachian units, it has indeed a density of boulders per m^2 that is 6.50 to 48.18 or 11.88 or 2.45 times greater than the remaining units.
The study of the areal density of the craters on Oxia was important not only from a scientific perspective, but also for rover landing and traversing reasons. Indeed, a landing in a crater with walls too steep would cause the rover to remain stuck inside with no possible exit, resulting in a failure for the mission. We obtained that the power-law indices of the exhumed Noachian units are steeper than the Amazonian unit in the most of the cases. This result is pivotal from engineering perspectives because it confirms the Ama-

zonian unit is more dangerous than the exhumed Noachian ones, hence it should be avoided as landing site. As for the craters, the boulder analysis is important from an engineering perspective, because it provides the safest areas where the ExoMars 2020 rover might land and traverse. The best areas both for landing and roving are the exhumed Noachian units and not the Amazonian one, as previously found with the crater analysis. We also made a comparison with the boulder densities derived in Pajola et al. (2017) on Oxia Planum and the results obtained show that the boulder densities are smaller than the previous measurements. Nevertheless, the erosive processes acted in similar way returning a similar SFD. We also compared our results with those derived from other landing sites on Mars. We found that the Pathfinder landing site is 4.2 times more dangerous than our exhumed Noachian 2 unit. Therefore, the right landing area for the ExoMars rover would be the exhumed Noachian 2 unit, but since they have similar elevation and thermal inertia also the exhumed Noachian 1 unit can be considered an optimal landing site.
From this work we can conclude that Oxia Planum is the right landing site for the ExoMars 2020 mission and for the search for life on Mars planet. We can assure that the Noachian unit is the safest region where to land.

The analysis we made was useful to date the region, to understand its evolution, to identify the processes occurred on the Martian surface and in particularly to locate the safest regions for the landing and roving phase of the future ExoMars 2020 rover.

Bibliography

Ahrens T. J. and Johnson M. L. (1995), *Shock Wave Data for Rocks*, Rock Physics and Phase Relations: A Handbook of Physical Constants, Vol. 3, doi:10.1029/RF003p0035, (January)

Ai H.-A. and Ahrens T. J. (2004), *Dynamic tensile strength of terrestrial rocks and application to impact cratering*, Meteoritics, Planetary Science, Vol. 39, Issue 2, doi:10.1111/j.1945-5100.2004.tb00338.x, (26), (January)

Aubrey A. (2006), *Sulfate minerals and organic compounds on Mars*, Geology, Vol. 34, doi:10.1130/G22316.1, (May), pp. 357-360

Balme M. et al. (2003), *Friction wind speeds in dust devils: A field study*, Geophysical Research Letters, Vol. 30, No. 16, doi:10.1029/2003GL017493, (August)

Barlow N. (2008), *Mars: an introduction to its interior, surface and atmosphere*, Cambridge planetary science, 8, Cambridge University Press, ISBN 978-0-521-85226-5

Bell III et al. (2013), *Calibration and performance of the Mars Reconnaissance Orbiter Context Camera (CTX)*, Mars the international journal of Mars science and exploration, doi:10.1555/mars.2013.0001, (April)

Bettanini C. et al. (2018), *The DREAMS experiment flown on the ExoMars 2016 mission for the study of Martian environment during the dust storm season*, Measurement, Vol. 122, doi:10.1016/j.measurement.2018.01.019, (July), pp. 484-493

Bibring J. P. et al. (2006), *Global Mineralogical and Aqueous Mars*

History Derived from OMEGA/Mars Express Data, Science, Vol. 312, Issue 5772, doi:10.1126/science.1122659, (April), pp. 400-404

Bourke M. C. et al., (2005), *The Surface Features of 'Pristine' Flood-transported Boulders*, Lunar and Planetary Science XXXVI

Briot D. (2013), *Present and Future Observations of the Earthshine from Antarctica*, International Astronomical Union, Vol. 8, doi:10.1017/S1743921312016900, pp. 214-217

Carr M.H., Head J.W. (2010), *Geologic history of Mars*, Earth and Planetary Science Letters, Vol. 294, Issues 3–4, doi:10.1016/j.epsl.2009.06.042, (1), (June), pp. 185-203

Carter et al. (2016), *Oxia Planum: A Clay-Laden Landing Site Proposed for the ExoMars Rover Mission: Aqueous Mineralogy and Alteration Scenarios*, 47th Lunar and Planetary Science Conference

Chevrier V. F. and Mathé P.-E. (2007), *Mineralogy and evolution of the surface of Mars: A review*, Planetary and Space Science, Vol. 55, doi:10.1016/j.pss.2006.05.039, (February), pp. 289-314

Christensen P.R. (1986a), *The Spatial Distribution of Rocks on Mars*, Icarus, Vol. 68, Issue 2, doi:10.1016/0019-1035(86)90020-5, (November), pp. 217-238

Christensen P.R. (1986b), *Regional dust deposits on Mars: Physical properties, age, and history*, Journal of Geophysical Research, Vol. 91, Issue B3, doi:10.1029/JB091iB03p03533, (10), (March)

Christensen P.R. et al. (2001), *Mars Global Surveyor Thermal Emission Spectrometer experiment: Investigation description and surface science results*, Journal of Geophysical Research, Vol. 106, Issue E10, doi:10.1029/2000JE001370, (1), (October)

Christensen P.R. et al. (2004), *The thermal emission imaging system (THEMIS) for the Mars 2001 Odyssey Mission*, Space Science Reviews, doi:10.1023/B:SPAC.0000021008.16305.94, (January), pp. 85-130

Crater analysis techniques working group (1979), *Standard tech-*

niques for presentation and analysis of crater size-frequency data, Icarus, Vol. 37, Issue 2, doi:10.1016/0019-1035(79)90009-5, (February), pp. 467-474

Delamere et al. (2003), *MRO High Resolution Imaging Science Experiment (HiRISE): Instrument Development*, Sixth International Conference on Mars

Ehlmann B.L. et al. (2008), *Clay minerals in delta deposits and organic preservation potential on Mars*, Nature Geoscience, Vol. 1, doi:10.1038/ngeo207, (June)

Ehlmann B.L. et al. (2009), *Identification of hydrated silicate minerals on Mars using MRO-CRISM: Geologic context near Nili Fossae and implications for aqueous alteration*, Journal of Geophysical Research, Vol. 114, Issue E2, doi:10.1029/2009JE003339, (23), (October)

Ellehoj M. D. et al. (2010), *Convective vortices and dust devils at the Phoenix Mars mission landing site*, Journal of Geophysical Research, Vol. 115, Issue E4, doi:10.1029/2009JE003413, (08), (April)

Galletta G., Bertoloni G., D'Alessandro M. (2010), *Bacterial survival in Martian conditions*, Earth and Planetary Astrophysics, arXiv:1002.4077, (February)

Galletta G., Sergi V. (2005), *Astrobiologia: le frontiere della vita*, Hoepli, ISBN 88-203-3424-0

Golombek M. P. et al. (2003a), *Rock size-frequency distributions on Mars and implications for Mars Exploration Rover landing safety and operations*, Journal of Geophysical Research, Volume 108, Issue E12, doi:10.1029/2002JE002035, (October)

Golombek M. P. et al. (2003b), *Selection of the Mars Exploration Rover landing sites*, Journal of Geophysical Research, Volume 108, Issue E12, doi:10.1029/2003JE002074, (December)

Golombek M. P. et al. (2008), *Size-frequency distributions of rocks on the northern plains of Mars with special reference to Phoenix landing surfaces*, Journal of Geophysical Research, Volume 113, Issue E3, doi:10.1029/2007JE003065, (July)

Golombek M. P. et al. (2012), *Detenction and Chatacterization of Rocks and Rock Size-Frequency Distributions at the Final Four Mars Science Laboratory Landing Sites*, Mars, Vol. 7, pp. 1-22

Golombek M. and Rapp D. (1997), *Size-frequency distributions of rocks on Mars and Earth analog sites: Implications for future landed missions*, Journal of Geophysical Research, Volume 102, Issue E2, doi:10.1029/96JE03319, (February)

Hartmann W. K. (1964), *On the Distribution of Lunar Crater Diameters*, Communications of the Lunar and Planetary Laboratory, Vol. 2, Part 1, pp.197-204

Hartmann W. K. (1965), *Terrestrial and Lunar Flux of Large Meteorites in the Last Two Billion Years*, Icarus, Vol. 4, Issue 2, doi:10.1016/0019-1035(65)90057-6, (May), pp. 157-165

Hartmann W. K. (1966), *Early lunar cratering*, Icarus, Vol. 5, Issue 1-6, doi:10.1016/0019-1035(66)90054-6, pp. 406-418

Hartmann W. K. (1969), *Terrestrial, lunar, and interplanetary rock fragmentation*, Icarus, Vol. 10, Issue 2, doi:10.1016/0019-1035(69)90022-0, (March), pp. 201-213

Hartmann W. K. (1977), *Relative crater production rates on planets*, Icarus, Vol. 31, Issue 2, doi:10.1016/0019-1035(77)90037-9, (June), pp. 260-276

Hartmann W. K. (1984), *Does crater "saturation equilibrium" occur in the solar system?*, Icarus, Vol. 60, Issue 1, doi:10.1016/0019-1035(84)90138-6, (October), pp. 56-74

Hartmann W. K. (1995), *Planetary cratering I: Lunar highlands and tests of hypotheses on crater populations*, Meteoritics, Vol. 30, doi:10.1111/j.1945-5100.1995.tb01152.x, p. 451

Hartmann W. K. (1999), *Martian cratering VI. Crater count isochrons and evidence for recent volcanism from Mars Global Surveyor*, Meteoritics and Planetary Science, Vol. 34, Issue 2, doi:10.1111/j.1945-5100.1999.tb01743.x, (February), pp. 167-177

Hartmann W. K. (2005), *Martian cratering 8: Isochron refinement and the chronology of Mars*, Icarus, Vol. 174, Issue 2, doi:10.1016/j.icarus.2004.11.023, (April), pp. 294-320

Hartmann W. K. (2007), *Martian cratering 9: Toward resolution of the controversy about small craters*, Icarus, Vol. 189, Issue 1, doi:10.1016/j.icarus.2007.02.011, (July), pp. 274-278

Hartmann W. K. and Neukum G. (2001), *Cratering Chronology and the Evolution of Mars*, Space Science Reviews, Volume 96, doi:10.1007/978-94-017-1035-0_6, pp. 165-194

Hartmann W. K. et al. (1981), *Chronology of planetary volcanism by comparative studies of planetary cratering*, in: Basaltic Volcanism Study Project (eds), Basaltic Volcanism on the terrestrial Planets, Pergamon, New York, pp. 1049–1127

Hartmann W. K. et al. (2008), *Confirmation and utilization of the "production function" size–frequency distribution of Martian impact craters*, Geophysical Research Letters, Vol. 35, doi:10.1029/2007GL031557, pp. 1–5

Hausrath E. M. et al. (2008), *Basalt weathering rates on Earth and the duration of liquid water on the plains of Gusev Crater, Mars*, Geology, Vol. 36, doi:10.1130/G24238A.1, (March)

Heather B. F. et al. (2017), *Initial SAM calibration gas experiments on Mars: Quadrupole mass spectrometer results and implications*, Planetary and Space Science, Vol. 138, doi:10.1016/j.pss.2017.01.014, (April), pp. 44-54

Hébrard E. et al., (2012), *An aerodynamic roughness length map derived from extended Martian rock abundance data*, Journal of Geophysical Research Atmospheres, Vol. 117, doi:10.1029/2011JE003942, (April)

Heet T. L. et al., (2009), *Geomorphic and geologic settings of the Phoenix Lander mission landing site*, Journal of Geophysical Research Atmospheres, Vol. 114, doi:10.1029/2009JE003416, (November)

Hiesinger H. et al. (2000), *Ages of mare basalts on the lunar*

nearside, Journal of Geophysical Research, Vol. 105, Issue E12, doi:10.1029/2000JE001244, (December)

Ivanov B. A. (2001), *Mars/Moon cratering rate ratio estimates*, Space Science Reviews, Vol. 96, Issue 1-4, doi:10.1023/A:1011941121102, pp. 87–104

Ivanov B. (2008), *Size-Frequency Distribution Of Asteroids And Impact Craters: Estimates Of Impact Rate*, from book Catastrophic Events Caused by Cosmic Objects, doi:10.1007/978-1-4020-6452-4_2, (January)

Ivanov B. A., Neukum, G. and Wagner, R. (2001), *Size-frequency distributions of planetary impact craters and asteroids*, in Collisional processes in the solar system, ed. by: Mikhail Ya. Marov and Hans Rickman, Astrophysics and space science library, Vol. 261, Dordrecht: Kluwer Academic Publishers, ISBN 0-7923-6946-7, doi:10.1007/978-94-010-0712-2_1, pp. 1-34

Ivanov B. et al., (2002), *The Comparison of Size-Frequency Distributions of Impact Craters and Asteroids and the Planetary Cratering Rate*, Asteroids III, W. F. Bottke Jr., A. Cellino, P. Paolicchi, and R. P. Binzel (eds), University of Arizona Press, Tucson, pp.89-101

Jaeger J. G. et al. (2007), *Fundamental of Rock Mechanics*, doi:10.1017/CBO9780511735349, publisher: Blackwell Publishers, (January)

Jakosky B. M. et al. (2015), *Initial results from the MAVEN mission to Mars*, Geophysical Research Letters, doi:10.1002/2015GL065271

Kading B. and Straub J. (2015), *Utilizing in-situ resources and 3D printing structures for a manned Mars mission*, Acta Astronautica, Vol. 107, doi:10.1016/j.actaastro.2014.11.036, (Feb-Mar), pp. 317-326

Kass D. M. et al. (2003), *Analysis of atmospheric mesoscale models for entry, descent, and landing*, Journal of Geophysical Research, Vol. 108, Issue E12, doi:10.1029/2003JE002065, (25), (November)

Kerr R. A. (2005), *Ice or Lava Sea on Mars? A Transatlantic Debate Erupts*, Science, Volume 307, doi:10.1126/science.307.5714.1390a,

(4), (March)

Küppers M. et al. (2012), *Boulders on Lutetia*, Planetary and Space Science, doi:10.1016/j.pss.2011.11.004, pp. 71-78

Lewis K.W., Aharonson O. (2006), *Stratigraphic analysis of the distributary fan in Eberswalde crater using stereo imagery*, Journal of Geophysical Research, Volume 111, doi:10.1029/2005JE002558

Malin M.C. et al. (2006), *Present-Day Impact Cratering Rate and Contemporary Gully Activity on Mars*, Science, Vol. 314, Issue 5805 doi:10.1126/science.1135156, (8), (December), pp. 1573-1577

Malin M. C. et al. (2007), *Context Camera Investigation on board the Mars Reconnaissance Orbiter*, Journal of Geophysical Research, Vol. 112, doi:10.1029/2006JE002808, (May)

McEwen A. S. et al. (2007), *Mars Reconnaissance Orbiter's High Resolution Imaging Science Experiment (HiRISE)*, Journal of Geophysical Research, Vol. 112, Issue E5, doi:10.1029/2005JE002605, (17), (May)

McEwen A. S. and Bierhaus E. B. (2006), *The importance of secondary cratering to age constraints on planetary surface*, Annual Review of Earth and Planetary Sciences, Vol. 34, doi:10.1146/annurev.earth.34.031405.125018, (April)

Melosh H. J. (1984), *Impact ejection, spallation, and the origin of meteorites*, Icarus, Vol. 59, Issue 2, doi:10.1016/0019-1035(84)90026-5, (August), pp. 234-260

Melosh H. J. (1989), *Impact cratering: A geologic process*, Earth Science Reviews, Vol. 41, Issue 3-4, doi:10.1016/S0012-8252(96)00035-9, (November), pp. 222-224

Michael G. G. et al. (2012), *Planetary surface dating from crater size–frequency distribution measurements: Spatial randomness and clustering*, Icarus, Vol. 218, Issue 1, doi:10.1016/j.icarus.2011.11.033, (March), pp. 169-177

Michael G.G. (2013), *Planetary surface dating from crater size–frequency distribution measurements: Multiple resurfacing episodes and differential*

isochron fitting, Icarus, Vol. 226, Issue 1, doi:10.1016/j.icarus.2013.07.004, (Sep-Oct), pp. 885-890

Michael G. G. and Neukum G. (2010), *Planetary surface dating from crater size frequency distribution measurements: Partial resurfacing events and statistical age uncertainty*, Earth and Planetary Science Letters, Vol. 294, Issue 3-4, doi:10.1016/j.epsl.2009.12.041, (June), pp.223-229

Michalski J. R. et al. (2017), *Ancient hydrothermal seafloor deposits in Eridania basin on Mars*, Nature Communications, doi:10.1038/ncomms15978, (July)

Michikami T. et al. (2008), *Size-frequency statistics of boulders on global surface of asteroid 25143 Itokawa*, Earth Planets and Space, Vol. 60, Issue 1, doi:10.1186/BF03352757, (January), pp. 13-20

Mottola S. et al. (2015), *The structure of the regolith on 67P/Churyumov-Gerasimenko from ROLIS descent imaging*, Science, Vol. 349, doi:10.1126/science.aab0232, (July)

Mouginot J. et al. (2010), *The 3–5 MHz global reflectivity map of Mars by MARSIS/Mars Express: Implications for the current inventory of subsurface H_2O*, Icarus, Vol. 210, Issue 2, doi:10.1016/j.icarus.2010.07.003, (December), pp. 612-625

Mpodozis C. et al. (1996), *Geología de la región de Ojos del Salado (Andes centrales, 27˚S): Implicancias de la migración hacia el este del frente volcánico Cenozoico Superior*, XIII Congreso Geológico Argentino y III Congreso de Exploración de Hidrocarburos, Actas III, (January), pp. 539-548

Murchie S. et al. (2007), *Compact Reconnaissance Imaging Spectrometer for Mars (CRISM) on Mars Reconnaissance Orbiter (MRO)*, Journal of Geophysical Research, Vol. 112, Issue E5, doi:10.1029/2006JE002682, (May)

Mustard J.F., Beaty D., Bass D. (2013), *Mars 2020 Science Rover: Science Goals and Mission Concept*, American Astronomical Society, (October)

Mustard J.F. et al. (2008), *Hydrated silicate minerals on Mars observed by the Mars Reconnaissance Orbiter CRISM instrument*, Nature, doi:10.1038/nature07097, (July)

Neukum (1977a), *Lunar cratering*, Philosophical Transactions of the Royal Society of London, Series A, Mathematical and Physical Sciences, doi:10.1098/rsta.1977.0064, (31), (March)

Neukum (1977b), *Different ages of lunar light plains*, The moon, Vol. 17, Issue 4, (December), pp 383–393

Neukum G. (1983), *Meteoritenbombardement und Datierung planetarer Oberflächen*, University of Munich. (February), p. 1-186

Neukum G. and Ivanov B. A. (1994), *Crater Size Distributions and Impact Probabilities on Earth from Lunar, Terrestrial-planet, and Asteroid Cratering Data*, Hazards due to comets and asteroids, Space Science Series, Tucson, AZ: Edited by Tom Gehrels, M. S. Matthews. and A. Schumann, published by University of Arizona Press, p.359

Neukum G. and König B. (1976), *Dating of individual lunar craters*, in: Lunar Science Conference, 7th, Houston, Tex., Vol. 3, (March), pp. 2867-2881

Neukum G. et al. (1975a), *A study of lunar impact crater size-distributions*, The Moon, Vol. 12, (February), pp. 201-229

Neukum G. et al. (1975b), *Cratering in the earth-moon system - Consequences for age determination by crater counting*, in Lunar Science Conference, 6th, Houston, Tex., Vol. 3, (March), pp. 2597-2620

Neukum G., Ivanov B. A. and Hartmann W. K. (2001a), *Cratering Records in the Inner Solar System in Relation to the Lunar Reference System* Space Science Reviews, Vol. 96, Issue 1-4, doi:10.1023/A:1011989004263, pp. 55-86

Neukum G. et al. (2001b), *Geologic evolution and cratering history of Mercury*, Planetary and Space Science, Vol. 49, doi:10.1016/S0032-0633(01)00089-7 , (December)pp. 1507-1521

Nowicki S.A., Christensen P.R. (2007), *Rock abundance on Mars*

from the thermal emission spectrometer, Journal of Geophysical Research, Vol. 112, Issue E5, doi:10.1029/2006JE002798, (17), (May)

Oberbeck V. R. and Morrison R. H. (1973), *On the formation of the lunar herringbone pattern*, Proceedings of the Lunar Science Conference, Vol. 4, p.107

Oberbeck V. R. and Morrison R. H. (1974), *Laboratory simulation of the herringbone pattern associated with lunar secondary crater chains*, The moon, Vol. 9, Issue 3-4, doi:10.1007/BF00562581 , (September), pp. 415-455

Orosei R. et al. (2018), *Radar evidence of subglacial liquid water on Mars*, Science, Vol. 361, Issue 6401, doi:10.1126/science.aar7268, (03), (August), pp. 490-493

Osinski G. R., Tornabene L. L. and Grieve R. A. F. (2001), *Impact ejecta emplacement on terrestrial planets*, Earth and Planetary Science Letters, Vol. 310, doi:10.1016/j.epsl.2011.08.012, (October), pp. 167–181

Pajola M. et al. (2015), *Size-frequency distribution of boulders $\geq$7 m on comet 67P/Churyumov-Gerasimenko*, Astronomy and Astrophysics, Vol. 583, A37, doi:10.1051/0004-6361/201525975

Pajola M. et al. (2016a), *Eridania Basin: An ancient paleolake floor as the next landing site for the Mars 2020 rover*, Icarus, Vol. 275, doi:10.1016/j.icarus.2016.03.029, (1), (September), pp. 163-182

Pajola M. et al. (2016b), *The Simud–Tiu Valles hydrologic system: A multidisciplinary study of a possible site for future Mars on-site exploration*, Icarus, Vol. 268, doi:10.1016/j.icarus.2015.12.049, (April), pp. 355-381

Pajola M. et al., (2016c), *The southern hemisphere of 67P/Churyumov-Gerasimenko: Analysis of the preperihelion size-frequency distribution of boulders $\geq$7 m*, Astronomy and Astrophysics, Vol. 592, L2, doi:10.1051/0004-6361/201628887, (July)

Pajola M. et al., (2016d), *The Agilkia boulders/pebbles size-frequency distributions: OSIRIS and ROLIS joint observations of 67P sur-*

face, Monthly Notices of the Royal Astronomical Society, Vol. 462, doi:10.1093/mnras/stw2720, (November)

Pajola M. et al. (2017), *Boulder abundances and size-frequency distributions on Oxia Planum-Mars: Scientific implications for the 2020 ESA ExoMars rover*, Icarus, Vol. 296, doi:10.1016/j.icarus.2017.05.011, (November), pp. 73-90

Pajola M. et al. (2019), *Planetary Mapping for Landing Sites Selection: The Mars Case Study*, Planetary Cartography and GIS, doi:https://doi.org/10.1007/978-3-319-62849-3_7, (February), pp. 175-190

Putzig N.E. et al. (2005), *Global thermal inertia and surface properties of mars from the MGS mapping mission*, Icarus, Vol. 173, Issue 2, doi:10.1016/j.icarus.2004.08.017, (February), pp. 325-341

Putzig N.E., Mellon M.T. (2007), *Apparent thermal inertia and the surface heterogeneity of Mars*, Icarus, Vol. 191, Issue 1, doi:10.1016/j.icarus.2007.05.013, (November), pp. 68-94

Quantin C. (2007), *Possible Long-term Decline in Impact Rates 1: Martian Geological Data*, Icarus, Vol. 186, doi:10.1016/j.icarus.2006.07.008, (January), pp. 1-10

Quantin et al. (2015), *Oxia Planum: a suitable landing site for ExoMars 2018 Rover*, European Planetary Science Congress, Vol. 10

Quantin et al. (2016), *Oxia Planum, The Landing Site for ExoMars 2018*, 47th Lunar and Planetary Science Conference

Rafkin S.C.R., Michaels T.I. (2003), *Meteorological predictions for 2003 Mars Exploration Rover high-priority landing sites*, Journal of Geophysical Research, Vol. 108, Issue E12, doi:10.1029/2002JE002027, (24), (October)

Ribes-Pleguezuelo P. et al. (2019), *Insights of the Qualified ExoMars Laser and Mechanical Considerations of Its Assembly Process*, Instruments, doi:10.3390/instruments3020025, (April)

Ringrose, T.J., Towner, M.C. and Zarnecki, J.C. et al. (2003), *Convective*

vortices on Mars: a reanalysis of Viking Lander 2 meteorological data, sols 1–60, Icarus, Vol. 163, doi:10.1016/S0019-1035(03)00073-3, pp. 78–87

Rivoldini A. et al. (2011), *Geodesy constraints on the interior structure and composition of Mars*, Icarus, Volume 213, Issue 2, doi:10.1016/j.icarus.2011.03.024, (June), pp. 451-472

Ruff S.W., Christensen P.R. (2002), *Bright and dark regions on Mars: Particle size and mineralogical characteristics based on Thermal Emission Spectrometer data*, Journal of Geophysical Research, Vol. 107, Issue E12, doi:10.1029/2001JE001580, (11), (December)

Ryan J. A. and Carroll J. J. (1970), *Dust devil wind velocities: Mature state*, Journal of Geophysical Research, Vol. 75, Issue 3, doi:doi.org/10.1029/JC075i003p00531, (20), (January)

Ryan J. A. and Lucich R. D. (1983), *Possible dust devils - Vortices on Mars* , Journal of Geophysical Research, Vol. 88, (20), (December), pp. 11005-11011

Sakai S. et al. (2018), *Effects of a Weak Intrinsic Magnetic Field on Atmospheric Escape From Mars*, Geophysical Research Letters, doi:10.1029/2018GL079972, (29), (August)

Segura T.L. et al. (2002), *Environmental Effects of Large Impacts on Mars*, Science, Vol. 298, doi:10.1126/science.1073586, (6), (December)

Shoemaker E. M. (1965), *Preliminary Analysis of the Fine Structure of the Lunar Surface in Mare Cognitum*, The Nature of the Lunar Surface, published by the Johns Hopkins Press, Baltimore, MD USA, p.23

Smith D.E. et al. (2001), *Mars Orbiter Laser Altimeter: Experiment summary after the first year of global mapping of Mars*, Journal of Geophysical Research, Vol. 106, Issue E10, doi:10.1029/2000JE001364, (25), (October)

Smith I. B. et al. (2016), *An ice age recorded in the polar deposits of Mars*, Science, Vol. 352, Issue 6289, doi:10.1126/science.aad6968, pp. 1075-1078

Strom R. G. and Sprague A. L. (2003), *Exploring Mercury: the*

iron planet, The Journal of the British Astronomical Association, Vol. 114, (March)

Surveyor Scientific Evaluation and Analysis Team (1966), *Size Distribution of Debris on Lunar Surface and Characteristics of Fine Matrix*, in Lunar Surface Topography, Surveyor 1 Mission Report

Tanaka K. L. et al. (2014), *Geologic map of Mars*, US Geological Survey, doi:10.3133/sim3292

Thomas N. et al. (2017), *The Colour and Stereo Surface Imaging System (CaSSIS) for the ExoMars Trace Gas Orbiter*, Space Sci Rev, Vol. 212, Issue 3-4, doi:10.1007/s11214-017-0421-1, pp. 1897-1944

Vago J.L. et al. (2017), *Habitability on Early Mars and the Search for Biosignatures with the ExoMars Rover*, Astrobiology, Vol. 17, doi:10.1089/ast.2016.1533, (July)

Vasavada A.R. et al. (2012), *Assessment of Environments for Mars Science Laboratory Entry, Descent, and Surface Operations*, Space, Vol. 170, Issue 1-4, doi:10.1007/s11214-012-9911-3, (September), pp. 793–835

Viles H. A. et al., (2005), *What Processes Have Shaped Basalt Boulders on Earth and Mars? Studies of Feature Persistence Using Facet Mapping and Fractal Analysis*, 36th Annual Lunar and Planetary Science Conference, (March), in League City, Texas, abstract no.2237

Wagner R. J. et al. (2002), *Stratigraphic sequence and ages of volcanic units in the Gruithuisen Region of the Moon*, Conference: 27th General Assembly of the European Geophysical Society, Nice, France, doi:10.1029/2002JE001844

Wagner R. et al. (2010), *Lunar red spots: Stratigraphic sequence and ages of domes and plains in the Hansteen and Helmet regions on the lunar nearside*, Journal of Geophysical Research, Vol. 115, Issue E6, doi:10.1029/2009JE003359, (26), (June)

Wilhelms D. E. (1987), *The geologic history of the Moon*, U.S. Geological Survey Professional Paper 1348, doi:10.3133/pp1348

Woronow A. (1977), *Crater saturation and equilibrium: A Monte*

Carlo simulation, Journal of Geophysical Research, Vol. 82, Issue 17, doi:10.1029/JB082i017p02447, (June)

Woronow A. (1978), *A general cratering-history model and its implications for the lunar highlands*, Icarus, Vol. 34, Issue 1, doi:10.1016/0019-1035(78)90127-6, (April), pp. 76-88

Wray J.J. et al. (2010), *Identification of the Ca-sulfate bassanite in Mawrth Vallis, Mars*, Icarus, Vol. 209, Issue 2, doi:10.1016/j.icarus.2010.06.001, (October), pp. 416-421

Yesavage T. et al. (2015), *Basalt weathering in an Arctic Mars-analog site*, Icarus, Vol. 254, doi:10.1016/j.icarus.2015.03.011, (July), pp. 219-232

Zuber M. T. et al. (1992), *The Mars Observer laser altimeter investigation*, Journal of Geophysical Research, Vol. 97, Issue E5, doi:10.1029/92JE00341, (25), (May)

Zurek R. W. and Smrekar S. E. (2007), *An overview of the Mars Reconnaissance Orbiter (MRO) science mission*, Journal of Geophysical Research, Vol. 112, Issue E5, doi:10.1029/2006JE002701, (May)